ORNL NUREG-1

Test of 6-In.-Thick Pressure Vessels. Series 3: Intermediate Test Vessel V-7

J. G. Merkle
G. C. Robinson
P. P. Holz
J. E. Smith
R. H. Bryan

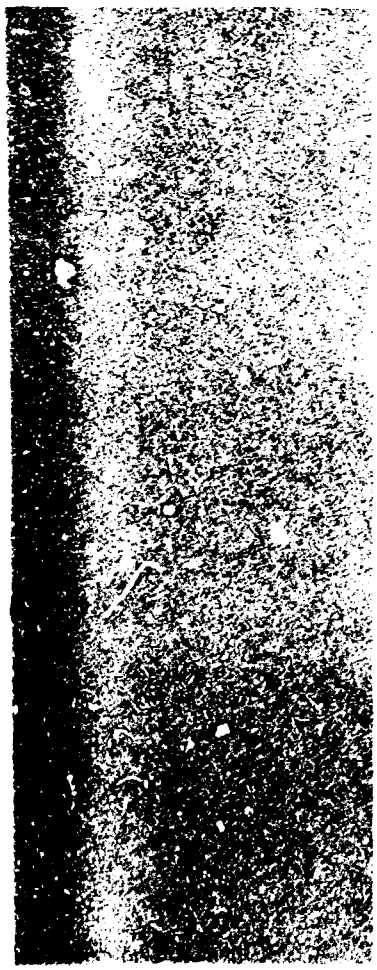

OAK RIDGE NATIONAL LABORATORY
OPERATED BY UNION CARBIDE CORPORATION FOR THE ENERGY RESEARCH AND DEVELOPMENT ADMINISTRATION

BLANK PAGE

Printed in the United States of America. Available from
National Technical Information Service
U.S. Department of Commerce
5285 Port Royal Road, Springfield, Virginia 22161
Price: Printed Copy $6.00; Microfiche $2.25

ORNL/NUREG-1
Dist. Category NRC-5

REACTOR DIVISION

TEST OF 6-IN.-THICK PRESSURE VESSELS. SERIES 3: INTERMEDIATE TEST VESSEL V-7

J. G. Merkle P. P. Holz
G. C. Robinson J. E. Smith
S. H. Bryan

Prepared for the U. S. Nuclear Regulatory Commission under Interagency Agreement 40-495-75

Manuscript Completed - 7-26-76

Date Completed - August 1976

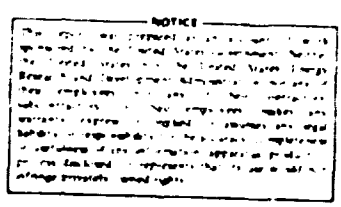

OAK RIDGE NATIONAL LABORATORY
Oak Ridge, Tennessee 37830
operated by
UNION CARBIDE CORPORATION
for the
ENERGY RESEARCH AND DEVELOPMENT ADMINISTRATION

Contents

BLANK PAGE

Foreword

The work reported here was performed mostly at Oak Ridge National Laboratory (ORNL) under sponsorship of the U.S. Nuclear Regulatory Commission's (NRC) Heavy-Section Steel Technology (HSST) Program, which is directed by ORNL. The program is conducted as part of the ORNL Pressure Vessel Technology Program, of which G. D. Whitman is manager. The manager for the NRC is E. K. Lynn.

This report is designated Heavy-Section Steel Technology Program Technical Report No. 40. Prior reports in this series are listed below.

1. S. Yukawa, *Evaluation of Periodic Proof Testing and Warm Prestressing Procedures for Nuclear Reactor Vessels*, HSSTP-TR-1, General Electric Company, Schenectady, N.Y. (July 1, 1969).
2. L. W. Loechel, *The Effect of Section Size on the Transition Temperature in Steel*, MCR-69-189, Martin Marietta Corporation, Denver, Colo. (Nov. 20, 1969).
3. P. N. Randall, *Gross Strain Measure of Fracture Toughness of Steels*, HSSTP-TR-3, TRW Systems Group, Redondo Beach, Calif. (Nov. 1, 1969).
4. C. Visser, S. E. Gabrielse, and W. VanBuren, *A Two-Dimensional Elastic-Plastic Analysis of Fracture Test Specimens*, WCAP-7368, Westinghouse Electric Corporation, PWR Systems Division, Pittsburgh, Pa. (October 1969).
5. T. R. Mager, F. O. Thomas, and W. S. Hazelton, *Evaluation by Linear Elastic Fracture Mechanics of Radiation Damage to Pressure Vessel Steels*, WCAP-7328 (Rev.), Westinghouse Electric Corporation, PWR Systems Division, Pittsburgh, Pa. (October 1969).
6. W. O. Shabbits, W. H. Pryle, and E. T. Wessel, *Heavy Section Fracture Toughness Properties of A 533 Grade B Class 1 Steel Plate and Submerged Arc Weldment*, WCAP-7414, Westinghouse Electric Corporation, PWR Systems Division, Pittsburgh, Pa. (December 1969).
7. F. J. Loss, *Dynamic Tear Test Investigations of the Fracture Toughness of Thick-Section Steel*, NRL-7056, U.S. Naval Research Laboratory, Washington, D.C. (May 14, 1970).
8. P. B. Crosley and E. J. Ripling, *Crack Arrest Fracture Toughness of A 533 Grade B Class 1 Pressure Vessel Steel*, HSSTP-TR-8, Materials Research Laboratory, Inc., Glenwood, Ill. (March 1970).
9. T. R. Mager, *Post-Irradiation Testing of 2 T Compact Tension Specimens*, WCAP-7561, Westinghouse Electric Corporation, PWR Systems Division, Pittsburgh, Pa. (August 1970).
10. T. R. Mager, *Fracture Toughness Characterization Study of A 533, Grade B, Class 1 Steel*, WCAP-7578, Westinghouse Electric Corporation, PWR Systems Division, Pittsburgh, Pa. (October 1970).
11. T. R. Mager, *Notch Preparation in Compact Tension Specimens*, WCAP-7579, Westinghouse Electric Corporation, PWR Systems Division, Pittsburgh, Pa. (November 1970).
12. N. Levy and P. V. Marcal, *Three-Dimensional Elastic-Plastic Stress and Strain Analysis for Fracture Mechanics, Phase I: Simple Flawed Specimens*, HSSTP-TR-12, Brown University, Providence, R.I. (December 1970).
13. W. O. Shabbits, *Dynamic Fracture Toughness Properties of Heavy Section A 533 Grade B, Class 1 Steel Plate*, WCAP-7623, Westinghouse Electric Corporation, PWR Systems Division, Pittsburgh, Pa. (December 1970).
14. P. N. Randall, *Gross Strain Crack Tolerance of A 533-B Steel*, HSSTP-TR-14, TRW Systems Group, Redondo Beach, Calif. (May 1, 1971).
15. H. T. Corten and R. H. Sailors, *Relationship Between Material Fracture Toughness Using Fracture Mechanics and Transition Temperature Tests*, T&AM Report 346, University of Illinois, Urbana, Ill. (Aug. 1, 1971).

16. T. R. Mager and V. J. McLoughlin. *The Effect of an Environment of High Temperature Primary Grade Nuclear Reactor Water on the Fatigue Crack Growth Characteristics of A 533 Grade B Class 1 Plate and Weldment Material.* WCAP-7776. Westinghouse Electric Corporation. PWR Systems Division. Pittsburgh, Pa. (October 1971).

17. N. Levy and P. V. Marcal. *Three-Dimensional Elastic-Plastic Stress and Strain Analysis for Fracture Mechanics. Phase II: Improved Modeling.* HSSTP-TR-17. Brown University. Providence, R.I. (November 1971).

18. S. C. Grigory. *Six-Inch-Thick Flawed Tensile Tests. First Technical Summary Report. Longitudinal Specimens 1 through 7.* HSSTP-TR-18. Southwest Research Institute. San Antonio, Tex. (June 1972).

19. P. N. Randall. *Effects of Strain Gradients on the Gross Strain Crack Tolerance of A 533-B Steel.* HSSTP-TR-19. TRW Systems Group. Redondo Beach, Calif. (May 1, 1972).

20. S. C. Grigory. *Tests of Six-Inch-Thick Flawed Tensile Specimens. Second Technical Summary Report. Transverse Specimens Numbers 8 through 10. Welded Specimens Numbers 11 through 13.* HSSTP-TR-20. Southwest Research Institute. San Antonio, Tex. (June 1972).

21. L. A. James and J. A. Williams. *Heavy Section Steel Technology Program Technical Report No. 21. The Effect of Temperature and Neutron Irradiation Upon the Fatigue-Crack Propagation Behavior of ASTM A533, Grade B, Class 1 Steel.* HEDL-TME-72-132. Hanford Engineering Development Laboratory. Richland, Wash. (September 1972).

22. S. C. Grigory. *Tests of Six-Inch-Thick Flawed Tensile Specimens. Third Technical Summary Report. Longitudinal Specimens Numbers 14 through 16. Unflawed Specimen Number 17.* HSSTP-TR-22. Southwest Research Institute. San Antonio, Tex. (October 1972).

23. S. C. Grigory. *Tests of Six-Inch-Thick Flawed Tensile Specimens. Fourth Technical Summary Report. Tests of One-Inch-Thick Flawed Tensile Specimens for Size Effect Evaluation.* HSSTP-TR-23. Southwest Research Institute. San Antonio, Tex. (June 1973).

24. S. P. Ying and S. C. Grigory. *Tests of Six-Inch-Thick Tensile Specimens. Fifth Technical Summary Report. Acoustic Emission Monitoring of One-Inch and Six-Inch-Thick Tensile Specimens.* HSSTP-TR-24. Southwest Research Institute. San Antonio, Tex. (November 1972).

25. R. W. Derby et al.. *Test of 6-Inch-Thick Pressure Vessels. Series 1: Intermediate Test Vessels V-1 and V-2.* ORNL-4895 (February 1974).

26. W. J. Stelzman and R. G. Berggren. *Radiation Strengthening and Embrittlement in Heavy Section Plates and Welds.* ORNL-4871 (June 1973).

27. P. B. Crosley and E. J. Ripling. *Crack Arrest in an Increasing K-Field.* HSSTP-TR-27. Materials Research Laboratory. Glenwood, Ill. (January 1973).

28. P. V. Marcal, P. M. Stuart, and R. S. Bettes. *Elastic-Plastic Behavior of a Longitudinal Semi-Elliptical Crack in a Thick Pressure Vessel.* Brown University, Providence, R.I. (June 1973).

29. W. J. Stelzman. Characterization of HSST Plates 01, 02, and 03 (in preparation).

30. D. A. Canonico. Characterization of Heavy Section Weldments in Pressure Vessel Steels (in preparation).

31. J. A. Williams. *The Irradiation and Temperature Dependence of Tensile and Fracture Properties of ASTM A533, Grade B, Class 1 Steel Plate and Weldment.* HEDL-TME 73-75. Hanford Engineering Development Laboratory. Richland, Wash. (August 1973).

32. J. M. Steichen and J. A. Williams. *High Strain Rate Tensile Properties of Irradiated ASTM A533 Grade B Class 1 Pressure Vessel Steel.* HEDL-TME 73-74. Hanford Engineering Development Laboratory. Richland, Wash. (July 1973).

33. P. C. Riccardella and J. L. Swedlow, *A Combined Analytical-Experimental Fracture Study*, WCAP-8224, Westinghouse Electric Corporation, PWR Systems Division, Pittsburgh, Pa. (October 1973).

34. R. J. Podlasek and R. J. Eiber, *Final Report on Investigation of Mode III Crack Extension in Reactor Piping*, Battelle Columbus Laboratories, Columbus, Ohio (May 1974).

35. T. R. Mager et al., *Interim Report on the Effect of Low Frequencies on the Fatigue Crack Growth Characteristics of A533 Grade B Class 1 Plate in an Environment of High-Temperature Primary Grade Nuclear Reactor Water*, WCAP-8256, Westinghouse Electric Corporation, Pittsburgh, Pa. (December 1973).

36. J. A. Williams, *The Irradiated Fracture Toughness of ASTM A533, Grade B, Class 1 Steel Measured with a Four Inch Thick Compact Tension Specimen*, HEDL-TME 75-10, Hanford Engineering Development Laboratory, Richland, Wash. (January 1975).

37. R. H. Bryan et al., *Test of 6-in.-thick Pressure Vessels, Series 2. Intermediate Test Vessels V-3, V-4, and V-6*, ORNL-5059 (November 1975).

38. T. R. Mager, S. E. Yanichko, and L. R. Singer, *Fracture Toughness Characterization of HSST Intermediate Pressure Vessel Material*, WCAP-8456, Westinghouse Electric Corporation, Pittsburgh, Pa. (December 1974).

39. J. G. Merkle, G. D. Whitman, and R. H. Bryan, *An Evaluation of the HSST Program Intermediate Pressure Vessel Tests in Terms of Light-Water Reactor Pressure Vessel Safety*, ORNL/TM-5620 (November 1975).

Copies of these reports may be obtained from Laboratory Records Department, Oak Ridge National Laboratory, P.O. Box X, Oak Ridge, Tenn. 37830.

Test of 6-in.-thick Pressure Vessels. Series 3: Intermediate Test Vessel V-7

J. G. Merkle P. P. Holz
G. C. Robinson J. E. Smith
R. H. Bryan

Abstract

The test of intermediate test vessel V-7 was a crack-initiation fracture test of a 152-mm-thick (6-in.), 990-mm-OD (39-in.) vessel of ASTM A533, grade B, class 1 steel plate with a sharp outside surface flaw 457 mm (18 in.) long and about 135 mm (5.3 in.) deep. The vessel was heated to 91 C (196°F) and pressurized hydraulically until leakage through the flaw terminated the test at a peak pressure of 147 MPa (21,350 psi). Fracture toughness data obtained by testing precracked Charpy-V and compact-tension specimens machined from a prolongation of the cylindrical test shell were used in pretest analyses of the flawed vessel. The vessel, as expected, did not burst. Upon depressurization, the ruptured ligament closed so as to maintain static pressure without leakage at about 129 MPa (18,700 psi).

1. Introduction

The United States electric power industry adopted nuclear power as an economically competitive source of energy during the 1960–1970 decade. Plans were made and construction was started for boiling-water reactor (BWR) and pressurized-water reactor (PWR) nuclear generating stations in increasing numbers. The international energy crisis has intensified the pressure to utilize these types of nuclear power plants.

With the competitive commercialization of BWRs and PWRs, the predominant capacity ratings of these plants increased to about 1100 MW(e) with an attendant demand for larger, thicker reactor pressure vessels. The Heavy-Section Steel Technology (HSST) Program was instituted during this period of industrial change to accelerate investigations initiated by the industry of thick-section vessels for water-cooled nuclear reactor service. The program is especially concerned with developing the information necessary for assessing the influence of flaws on the safety and serviceability of the thick-section components of reactor pressure vessels. The program has developed data on the characteristics of plates, welds, and forgings in terms of mechanical properties, toughness, inherent flaws, and homogeneity. A major objective is to develop methods by which better estimates can be made of the effects of flaws on the service life and strength of vessels.

Methods of analysis as well as experimental methods are being developed for fracture evaluation of structures. A wide variety of specimen types and sizes have been tested under a wide range of loading conditions. Considerable progress has been made in understanding the behavior of flawed structures and in the application of results of tests of small specimens to the analysis and evaluation of large structures.

The importance of the size of test specimens and structures in the proper characterization of behavior has been demonstrated in many parts of the program. The confidence in methods of analysis so important in safety evaluation of nuclear vessels can be attained only in proportion to the degree to which theoretical methods have been tried by experience or experiment with appropriately sized structures under loading conditions of interest. Consequently, the HSST program includes simulated service tests, of which the intermediate vessel tests are a part.

BLANK PAGE

The aim of simulated service testing is to provide, through a series of experiments a connection between the behavior of structures observed in a laboratory environment and the behavior of full-size components under the wide variety of conditions that constitute the real operating environment. The main effort of this task is to determine, if not already known, which factors or conditions are important and then to carry out tests with the particular combinations of conditions that will contribute significant information on behavior of structures in service. Factors of concern include material properties; flaw location, orientation, shape, size, and sharpness; and loading and environmental conditions. If expense, resources, safety, and time were of no importance, the significance of these factors could be studied under actual service conditions imposed on vessels in a large number of experiments with vessels as large as, or larger than, reactor pressure vessels. Since such an approach is completely impractical, each factor is studied separately or in combination with others on as simple a scale as practicable.

The objective of each simulated service test is to determine the ability of analytical methods to predict actual fracture behavior of a flawed structure under known conditions of material properties and loading. In the planned progression of such tests, analytical methods are confirmed, improved, or their limitations revealed. The testing of intermediate vessels in conjunction with tests of flawed tensile specimens of similar material and flawed models of the intermediate vessels permits consideration of many variables. Thus the intermediate vessel tests are a part of a structural test program that covers ranges of flaw size, section thickness, temperature, and stress state. The effects of differences in transverse restraint, toughness, plastic strain, biaxiality, and stress concentration can be observed and analyzed.

The original objectives emphasized in the simulated service task were (1) to demonstrate capability to predict the "vessel transition temperature" for a selected crack configuration using the material of interest (ASTM A533, grade B, class 1 plate; ASTM A508, class 2 forging); (2) to demonstrate, for the materials of interest, capability to predict various combinations of load (pressure), temperature, and crack configuration in full-thickness walls 152 mm or more (6 in.) that will not cause fracture, and, finally, a combination that will cause fracture for both frangible and tough fracture conditions.

The intermediate vessel tests have been subdivided into four series:

1. flaws in cylindrical vessels, A508, class 2 forging steel -- two vessels;
2. flaws in cylindrical vessels with longitudinal submerged-arc weld seams, A508, class 2 forging steel -- three vessels;
3. flaws in cylindrical vessels with longitudinal submerged-arc weld seams, A533, grade B, class 1 plate steel -- two vessels;
4. cylindrical vessels with radially attached nozzles, vessels of A508, class 2 forging steel and A533, grade B, class 1 plate steel; nozzles of A508, class 2 forging steel -- three vessels.

The report[1] on the first series contains a comprehensive description of the pertinent factors considered in the design of the vessels and construction of the test facility and those leading to the tests of series 1, as well as a documentation of test results and fracture predictions. Emphasis is placed on providing the test results in such a manner that they form a resource for any investigators interested in the problem of fracture. The report[2] on series 2 documents comprehensive information on the characteristics of three test vessels, material properties, conditions of testing, and results so as to facilitate further analysis. The reports also describe the use of fracture toughness measurements based on equivalent-energy concepts. These measurements and the investigations of crack growth by tests of both large tensile specimens and model vessels provided the bases for analytical predictions of rupture conditions.

Intermediate test vessel V-7 has been tested in series 3. This vessel has the same cylindrical geometry as the five vessels of the first two series. However, vessel V-7 contained a flaw that was much larger and deeper than those of any other vessel tested. The test was preceded by tests of steel scale models of V-7 and by analyses, which all together indicated that the mode of failure would be the rupture of the thin ligament along the base of the flaw. Vessel V-7 failed as predicted, the test being necessarily terminated by the leakage of the pressurizing fluid. The vessel as a structure and the flaw itself remained stable throughout the test. Further testing of this vessel is planned.

REFERENCES

1. R. W. Derby et al., *Test of 6-in.-thick Pressure Vessels. Series 1: Intermediate Test Vessels V-1 and V-2*, ORNL-4895 (February 1974).
2. R. H. Bryan et al., *Test of 6-in.-thick Pressure Vessels. Series 2: Intermediate Test Vessels V-3, V-4, and V-6*, ORNL-5059 (November 1975).

2. Description of Vessels

DESIGN AND PROCUREMENT

Although intermediate vessels V-7 through V-10 were purchased under a separate purchase order from vessels V-1 through V-6, all features were identical with their earlier counterparts except for material requirements. The design of the intermediate test vessels provided for (1) material variation in base material and welding seams, (2) cylindrical shell thickness approximately that of light-water reactor (LWR) vessels, (3) special head and closure design to give reasonable assurance that these components would not fail prior to rupture of the cylindrical shell test part, and (4) achievement of economy by competitive lump sum bidding. The general physical features for vessel V-7 are shown in Fig. 2.1. The design and procurement activities for achieving the foregoing objectives are covered more fully in Refs. 1 and 2; the principal features are summarized here.

In the procurement of the first six vessels, the vendor, Taylor Forge Division of Gulf and Western Products Co., was permitted for economy, the option of utilizing either ASTM A508 class 2 forgings or ASTM A533, grade B, class 1 steel plate in the fabrication of the cylindrical shells. Also under this purchase order an option was requested to permit procurement of four extra head and access nozzle subassemblies. By this option four head subassemblies were obtained that subsequently, under a separate purchase order, became component parts of vessels V-7 through V-10. In the purchase order for vessels V-7 through V-10, only plate material conforming to ASTM A533, grade B, class 1 was permitted in the fabrication of the cylindrical shells in order to obtain data for both forging and plate forms that comprise the reference materials for the current generation of LWR vessels. This purchase order further provided that the shell courses could be made by using either one or two longitudinal submerged-arc welds and one or two shell segments per vessel. The vendor elected to make the shell courses for each vessel from a single shell segment with a single longitudinal weld seam. Fabrication of other vessel components for V-7 was sublet to National Forge Company of Irvine, Pa.

The cylindrical shell courses for vessels V-7 through V-10 were fabricated from plate produced by Lukens Steel Company from a single heat identified as B5233-2. Chemical analysis reported by the Lukens Mill Certification for this heat is as follows:

Ladle analysis (wt %)						
C	Mn	P	S	Si	Ni	Mo
0.20	1.23	0.015	0.017	0.26	0.49	0.52

The ingot was rolled to a 167-mm-thick ($6^{9}/_{16}$-in.) plate and given a stress-relieving heat treatment at 649°C (1200°F) for 3½ hr (see Fig. 2.2). The material for the test specimens was program (Data Trac) heat treated as follows:

1. austenitized at 899 ± 14°C (1650 ± 25°F) for 1.8 min/mm (¾ hr/in.) of thickness (see Fig. 2.3);
2. water quenched per cooling curve for 167-mm-thick plate (Fig. 2.3);
3. tempered at 682 ± 6°C (1260 ± 10°F) and held 2.4 min/mm (1 hr/in.) and water quenched (Fig. 2.4);
4. stress relieved by heating at 37 K/hr (67°F/hr) maximum to 593 + 28 −0°C (1100 + 50 −0°F), held for 30 hr, and furnace cooled at 46 K/hr (83°F/hr) maximum to 316°C (600°F) (see Fig. 2.5).

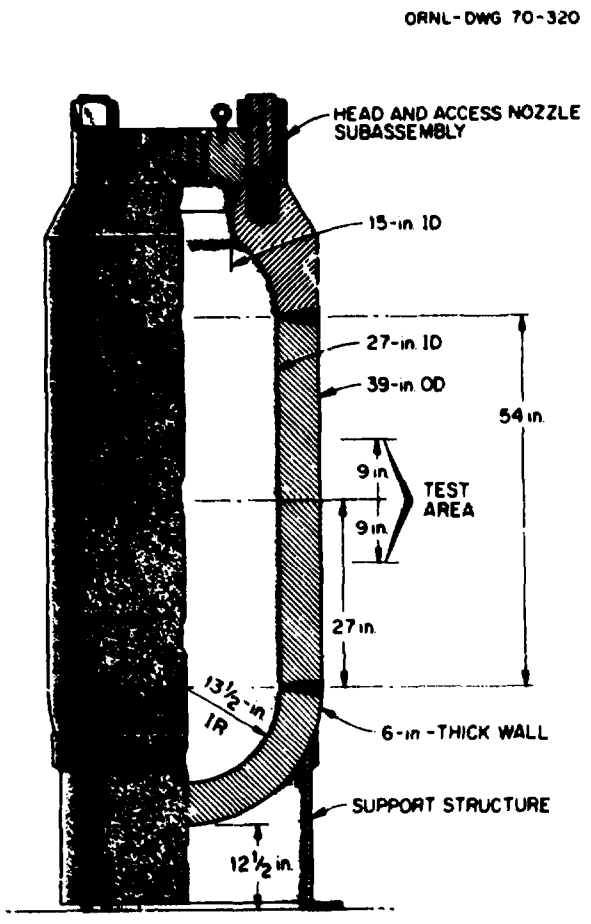

Fig. 2.1. HSST intermediate vessel.

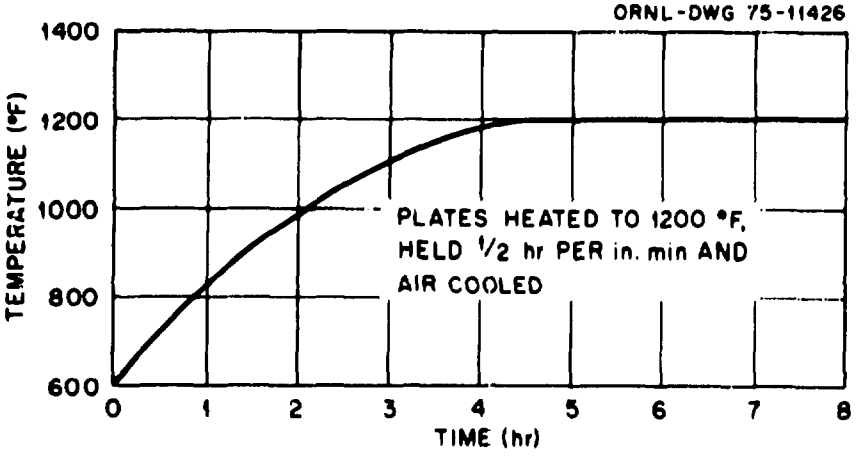

Fig. 2.2. Post-roll stress-relieving cycle for plate.

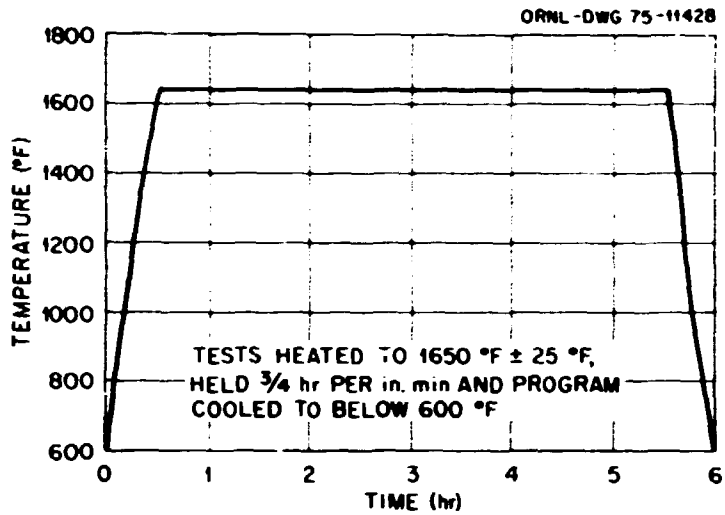

Fig. 2.3. Austenitizing and cooling cycle for plate for cylindrical shell course for vessels V-7 through V-10.

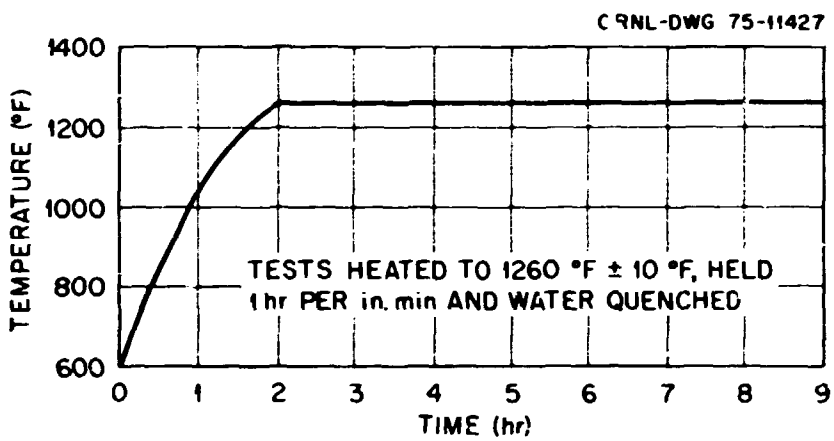

Fig. 2.4. Tempering cycle for plate for cylindrical shell courses for vessels V-7 through V-10.

The mechanical test results from specimens representing the shell material are:

Yield strength [MPa (ksi)]	Tensile strength [MPa (ksi)]	Elongation in 51 mm (2 in.) (%)	Longitudinal Charpy V-notch at −12°C (+10°F) [J (ft-lb)]	Lateral expansion [mm (mils)]	Fracture appearance (% shear)
450. (65.2)	586. (85.0)	26			
432. (62.6)	563. (81.6)	29	125-96-106 (92-71-78)	1.55-1.93-1.52 (61-76-60)	70-70-70

NDT temperature as determined by drop weight tests: −51°C (−60°F)

Before rolling, the plate segments for the shells and prolongations were cut to the proper dimensions and provided with the weld joint preparation shown in Fig. 2.6 and were then heated along the edges and

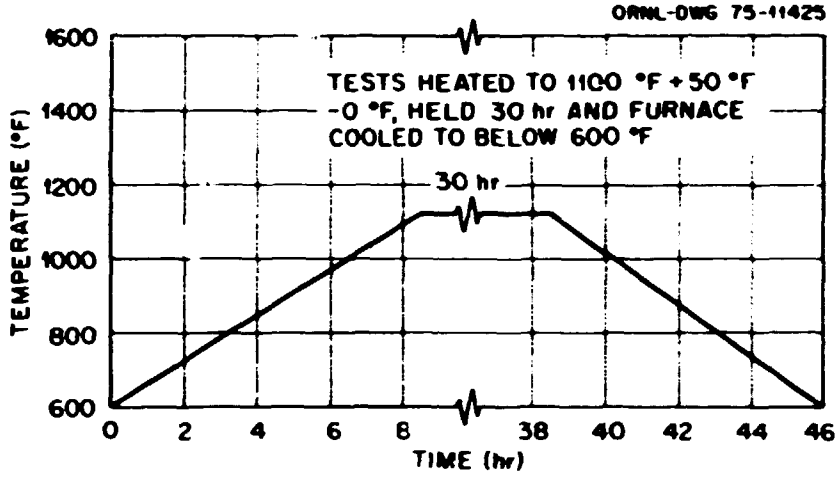

Fig. 2.5. Stress-relieving cycle for plate for cylindrical shell courses for vessels V-7 through V-10.

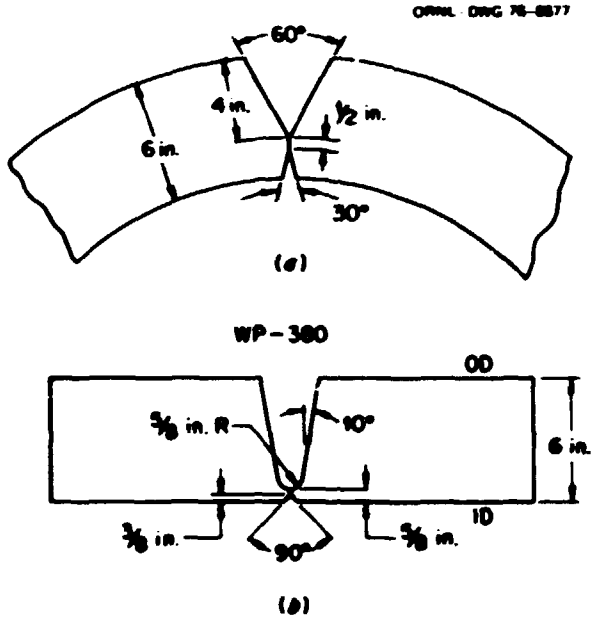

Fig. 2.6. Joint preparations for Taylor Forge welding procedures.

crimped to facilitate rolling. Later, the plates were charged into a furnace and heated to about 1093°C (2000°F) for rolling into a shell. Immediately after rolling and prior to removal from the rolls, the longitudinal weld joint preparation was tack welded.

On completion of the rolling operation and before any welding was completed, the shell courses and the respective prolongations of vessels V-7 through V-10 were typically concurrently subjected to heat treatments consisting of austenitizing at 899°C (1650°F) for 6½ hr, quenching in agitated water, tempering

at 682°C (1260°F) for 6½ hr and air cooling, and stress relieving at 621°C (1150°F) for 30 hr. They were then furnace cooled at 56 K hr (100°F hr) to 316°C (600°F) and air cooled to ambient temperature. In order to expedite fracture mechanics testing of the V-7 prolongation material, it was heat treated separately from the shell course and did not receive the same amount of postweld heat treatment. The V-7 prolongation received a total of 30 hr postweld heat treatment, the weld test plates for V-7 through V-10 received 20½ hr, and V-7 shell course received 10 hr.

Following rolling, the V-7 shell course and prolongation were aligned and tack welded together, and the longitudinal weld seam was joined by submerged-arc welding. The prolongation was removed from the shell course by flame cutting, given intermediate and final stress-relieving postweld heat treatments, and shipped to ORNL. After separation from the prolongation, the shell course was stress-relief heat treated, machined to final diametral dimensions, and machined to form the circumferential weld joint preparation.

Basically, Taylor Forge's procedure for making the longitudinal and circumferential weld seams for vessels V-7 through V-10 requires the following procedures and conditions:

1. machining the joint preparations as shown in Fig. 2.6*a* (longitudinal seam) and 2.6*b* (circumferential seam);
2. inspecting the groove surfaces with magnetic particles;
3. preheating to 149–260°C (300–500°F) and maintaining until postweld heat treatment (PWHT);
4. filling the shallow groove by the shielded metal-arc process (E8018 NM);
5. grinding the back side (OD side) to solid metal and inspecting with magnetic particles;
6. filling the deep groove with submerged-arc, RACO 127, 4.76-mm-diam ($^{3}/_{16}$-in.), single wire feed;
7. interpass temperature: 260°C (500°F) maximum;
8. flux: Linde type 0091, size 65 X 200;
9. travel speed: approximately 300 mm/mn (12 in./min);
10. current: ac, 750 A, 30–32 V;
11. usually on completion of a weld, the weldment was subjected to an intermediate PWHT at 593°C (1100°F) for 1½ hr, unless preheat was maintained until the next weld was made.

National Forge Company, subcontractor for other shell components, made the hemispherical heads, the closure cover, and the closure flange from their heats 3V-1283, 1-2401, and 4-1261 respectively. Chemical analyses for these heats are given in Table 2.1. Results of the mechanical property tests performed by National Forge on specimens taken from these heats are given in Table 2.2. Heat-treatment conditions employed by National Forge in the fabrication of these components are given in Table 2.3.

The Charpy V-notch data for the closure head and the closure flange given in Table 2.2 do not meet the requirements of Table N-421 of the ASME Code, Section III, for low-temperature −12°C (+10°F) toughness. However, since vessel V-7 was scheduled to be tested to failure at a temperature of 93°C (200°F) and since remelting would delay the delivery and testing schedules, the forging manufacturer was requested to test additional Charpy V-notch specimens at 10, 66, and 93°C (50, 150, and 200°F) for the closure cover and at −12, 4, 10, 66, and 93°C (10, 40, 50, 150, and 200°F) for the closure flange. The data given in Table 2.4 verified the acceptability of these components for 93°C service.

The components furnished by National Forge were subjected to longitudinal and shear-wave ultrasonic, magnetic particle, and dimensional inspections prior to shipment to Taylor Forge Company at Paola, Kan. The requisite procedures were identical to those employed on vessels V-1 through V-6.

Table 2.1. Chemical analyses for the hemispherical head, closure cover, and closure flange (%)

C	Mn	P	S	Si	Ni	Cr	Mo	V	Cu	Co
Hemispherical head, heat 3V-1283, ladle and check										
0.20	0.74	0.008	0.016	0.22	0.81	0.37	0.60	0.03		
0.18	0.73	0.007	0.017	0.23	0.83	0.38	0.60	0.03	0.10	0.007
Closure cover, heat 1-2401, ladle and check										
0.21	0.80	0.007	0.007	0.30	0.82	0.40	0.60	0.02		
0.19	0.79	0.008	0.010	0.29	0.82	0.39	0.61	0.02	0.09	0.010
Closure flange, heat 4-1261, ladle										
0.21	0.71	0.008	0.001	0.22	0.87	0.36	0.67	0.02		

Table 2.2. Mechanical properties obtained on specimens from the hemispherical head, closure cover, and closure flange[a]

Ultimate tensile strength (ksi)	Yield strength (ksi)	Reduction in area (%)	Elongation in 2-in. gage length (%)	C_v values at −12°C (ft-lb)	Percent shear	Lateral expansion (in.)
Hemispherical head						
87.5	68.5	69.3	25.0	30.5-38-47.5	30-32-38	0.029-0.030-0.039
87.5	67.5	70.4	26.0	46-55-58	40-46-45	0.037-0.047-0.046
Closure cover						
85.0	63.0	70.1	27.5	43-12.5-14		
85.5	63.5	70.6	27.0	36-15.5-28.5		
				27.5-12		
Closure flange						
86.0	66.0	69.9	25.0	34-14-10		
89.8	69.0	67.9	24.5	9-39-6		
				22.5-22		

[a]Conversion factors: 1 ksi = 6.895 MPa; 1 ft-lb = 1.356 J; 1 in. = 25.4 mm.

Table 2.3. Heat treatment conditions for hemispherical head, closure cover, and closure flange

Normalizing		Austenitizing		Tempering		Stress relieving		Grain size
Temperature [°C (°F)]	Time (hr)	Temperature [°C (°F)]	Time (hr)	Temperature [°C (°F)]	Time (hr)	Temperature [°C (°F)]	Time (hr)	
Hemispherical head								
927 (1700)	7	860 (1580)	7	704 (1300)	7	607 (1125)	30	7–8
Closure cover								
916 (1680)	11	854 (1570)	11	704 (1300)	8	607 (1125)	30	7–8
Closure flange								
854 (1570)	14			704 (1300)		621 (1150)	30	

Table 2.4. Charpy V-notch retest data for vessel V-7 components

Test temperature [°C (°F)]	C_v values[a] (ft-lb)		Lateral expansion of closure cover[c] (mils)	Percent fibrous fracture of closure cover
	Closure cover	Closure flange[b]		
12.2 (10)		34-14-10 9-39		
4.4 (40)		96-41-111 34-42-54.5		
10.0 (50)	28-102-89 29-53-35	28-102-89 29-53-355	22-97-75 27-48-30	32-51-48 28-28-32
65.6 (150)	141-123-143 120-115-117	141.5-123.5-143 115.5-117.5	90-79-100 100-97-75	100-90-100 85-84-79
93.3 (200)	145-141-141 125-135-135	146-141-125 135-135	96-110-108 104-105-105	100-100-100 100-100-100

[a] 1 ft-lb = 1.3558 J.

[b] Specimens were taken $\frac{1}{4}T$ from the inside surface since this probably represented the least tough material because of the slower quench on the inside surface.

[c] 1 mil = 0.0254 mm.

Taylor Forge joined the components by the submerged-arc welding procedure previously described. The fabrication sequence was comprised of welding, preliminary weld seam ultrasonic inspection, weld repair, postweld heat treatment, intermediate weld seam ultrasonic inspection, radiography, hydrostatic testing, final weld seam ultrasonic inspection, magnetic particle inspection, and leak testing.

MATERIALS CHARACTERIZATION

The prolongation of intermediate vessel V-7 was studied by Stelzman[3,4] to obtain tensile, Charpy V-notch impact, and static lower-bound fracture toughness data and by Mager et al. of Westinghouse Electric Corporation[5-7] to obtain static fracture toughness data. These data were used to set the fracture criteria and to predict failure prior to rupturing the vessel as was done for vessels V-1 through V-6.

Tensile and Charpy V-notch specimens were located in the material of interest (material in which the flaws resided, base material for vessel V-7) typically as shown in Fig. 2.7, and compact-tension specimens were located in the prolongations as shown in Fig. 2.8. Complete tabulations of tensile, Charpy V-notch impact, and fracture toughness data obtained by Stelzman are given in Appendix A.

Tensile and Charpy V-Notch Impact Data

Tensile test results at 93 and 25°C (200 and 77°F) from both tangentially (C) and axially (A) oriented specimens are shown in Figs. 2.9 and 2.10. The 4.52-mm-gage-diam (0.178-in.) subsize (MT) tensile specimen (L/D = 7) was used and tested at a strain rate of 0.016 min^{-1}. The through-the-wall strength distribution for the C and A orientations appears to be constant through the central 100 mm (4 in.). The increase in strength previously observed near the surfaces of the HSST plates due to the more rapid cooling rates during quenching was also present in this material.

Yield and ultimate stresses at 93°C (200°F) appear to be 503 and 621 MPa (73 and 90 ksi) at 7.6 mm (0.3 in.) and 434 and 572 MPa (63 and 83 ksi) through the 23- to 127-mm (0.9- to 5-in.) depths. The reduction in area results indicate that the ductility of the A-oriented specimens is 5% lower near the

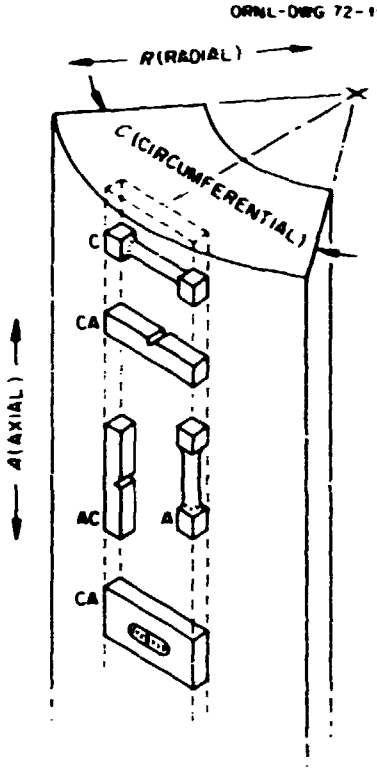

Fig. 2.7. Specimen orientation notation for HSST intermediate vessel materials showing tensile, Charpy V-notch, and drop-weight specimens.

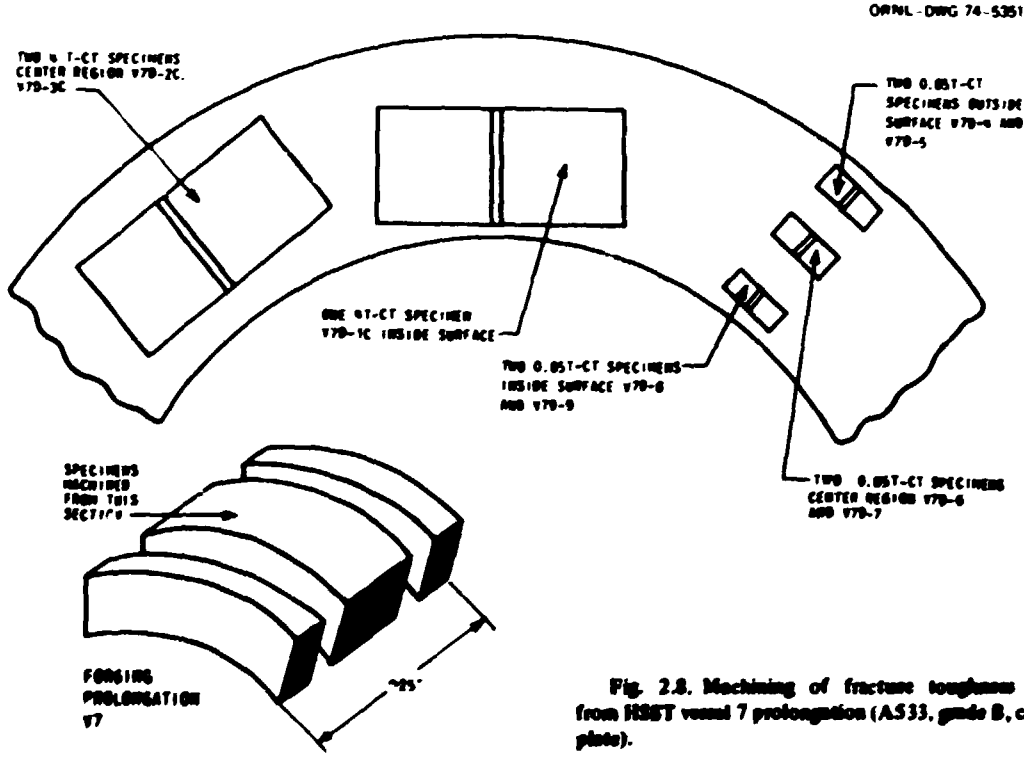

Fig. 2.8. Machining of fracture toughness specimens from HSST vessel 7 prolongation (A533, grade B, class 1 steel plate).

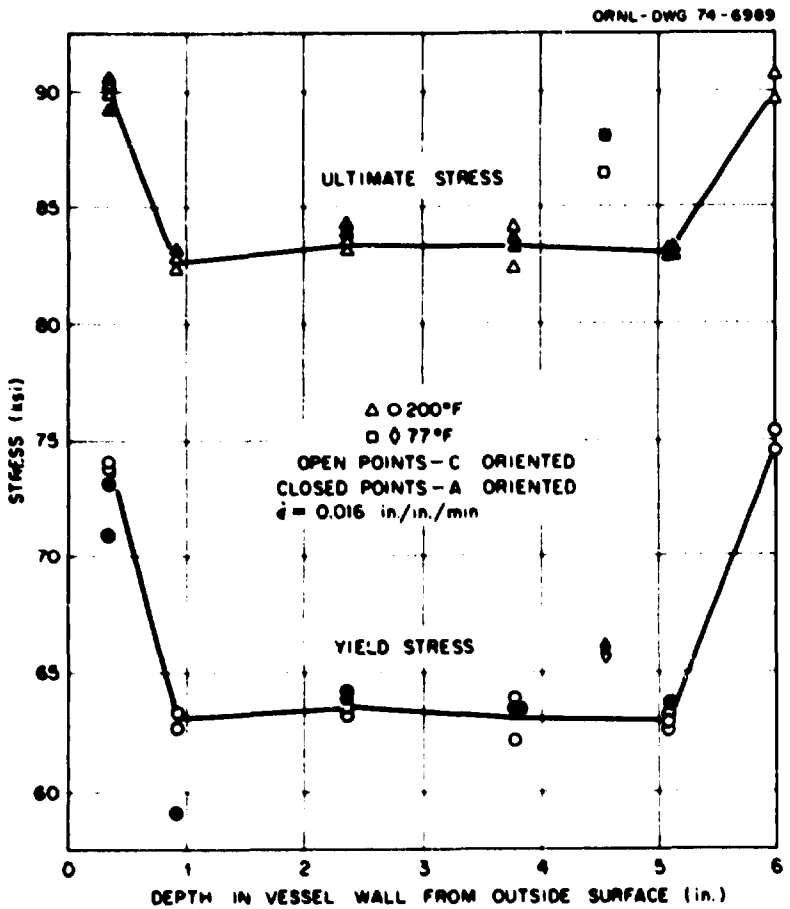

Fig. 2.9. Tensile properties of intermediate vessel V-7 using C- and A-oriented subsize tensile specimens from 152-mm-thick (6-in.) ASTM A533, grade B, class 1 carbon steel (1 ksi = 6.895 MPa; 1 in. = 25.4 mm).

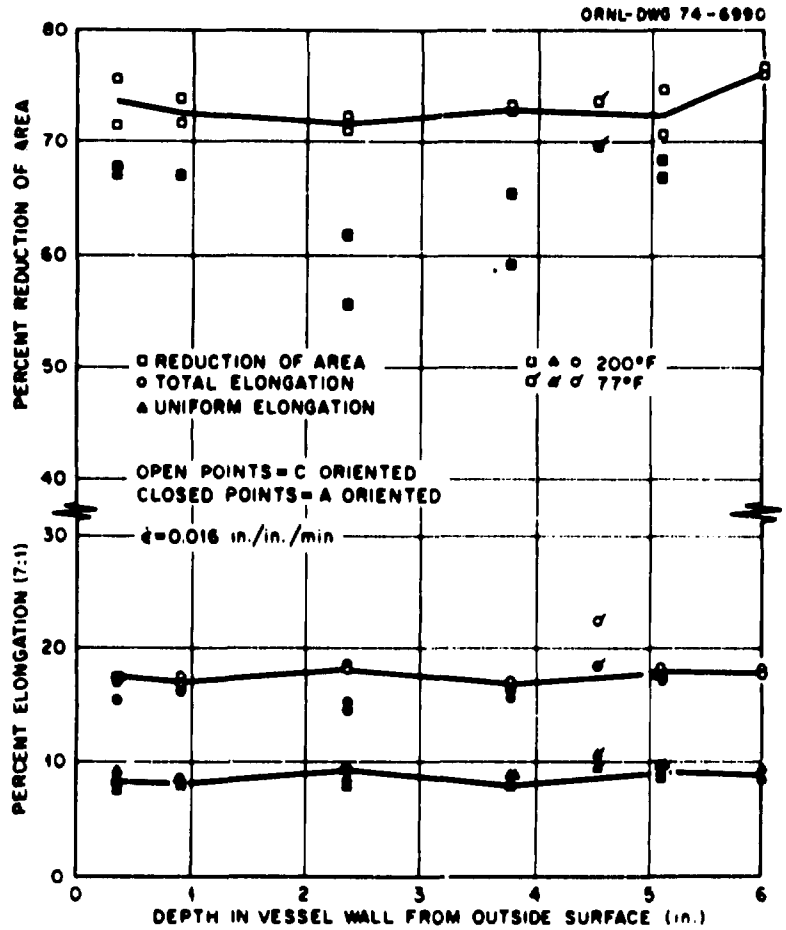

Fig. 2.10. Tensile properties of intermediate vessel V-7 using C- and A-oriented subsize tensile specimens from 152-mm-thick (6-in.) ASTM A533, grade B, class 1 carbon steel.

surfaces and 14% lower near ¼T than the C-oriented specimens. The C-oriented specimens show essentially constant ductility at about 73%. The elongation remained constant from surface to surface and did not vary significantly for the C and A orientations.

Charpy impact results from CA- and AC-oriented specimens indicate that the AC specimens have lower upper-shelf energies and transition regions occurring at higher temperatures. Both orientations indicate that the lowest energy values were obtained at the 54-mm (2⅛-in.) depth (from outer surface), that the inner half (0.59 and 0.79T) shows higher shelf energies than the outer half (0.05 and 0.36T), that the energy and lateral expansion transitions of all inner materials (0.36 to 0.79T) occur below 38°C (100°F), and that the upper shelf was attained at about 93°C (200°F). Figures 2.11 and 2.12 illustrate the distribution of both the energy and lateral expansion with temperature at selected depths.

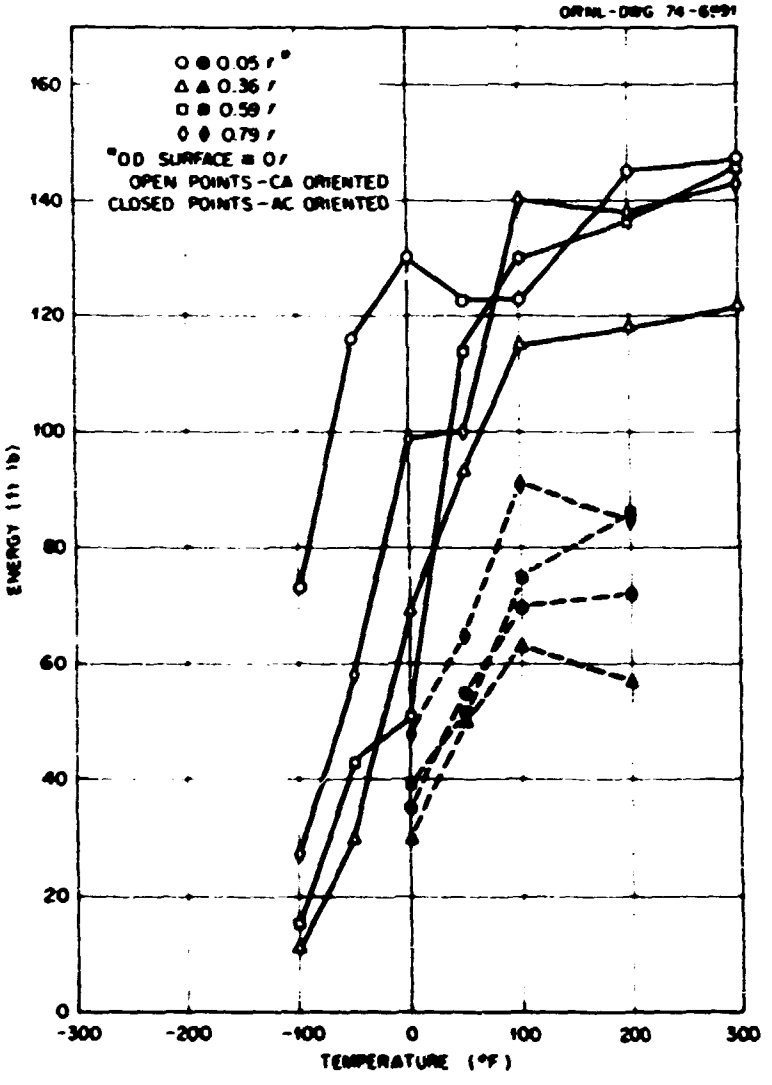

Fig. 2.11. Charpy-V impact properties of intermediate vessel V-7 using CA- and AC-oriented specimens from 152-mm-thick (6-in) ASTM A533, grade B, class 1 carbon steel (1 ft-lb = 1.356 J).

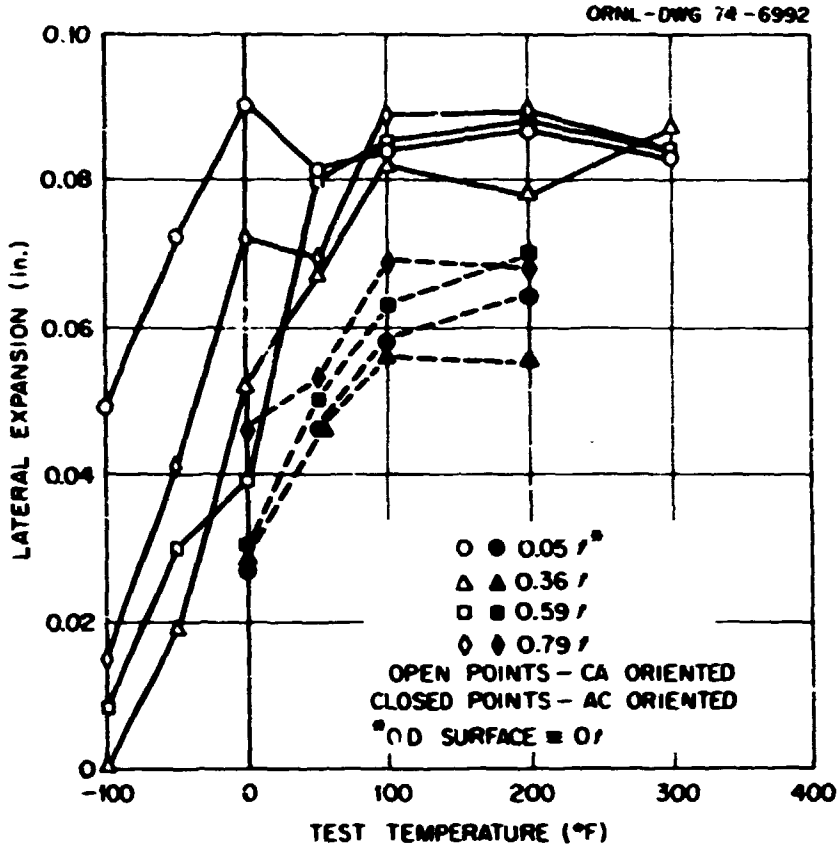

Fig. 2.12. Charpy-V impact properties of intermediate vessel V-7 using CA- and AC-oriented specimens from 152-mm-thick (6-in.) ASTM A533, grade B, class 1 carbon steel.

Fracture Toughness

Lower-bound static fracture toughness (K_{Icd}) results obtained by Stelzman from CA- and AC-oriented precracked Charpy specimens are shown in Figs. 2.13 and 2.14, and the lower-bound dynamic fracture toughness (K_{Idd}) data for the CA orientation are shown in Fig. 2.15. The effect of temperature on K_{Icd} indicates that the AC-oriented specimens exhibit lower upper-shelf values [165 to 192 MN·m$^{-3/2}$ (150 to 175 ksi $\sqrt{\text{in.}}$)] than the CA specimens [192 to 220 MN·m$^{-3/2}$ (175 to 200 ksi $\sqrt{\text{in.}}$)] except for the CA orientation near the outer surface (0.05T), where K_{Icd} values dip as low as 143 MN·m$^{-3/2}$ (130 ksi $\sqrt{\text{in.}}$) near room temperature. The toughest material in both orientations (highest K_{Icd}) occurs at mid-wall thickness. Generally, the static fracture toughness attained the upper shelf at −46°C (−50°F) or lower. The dynamic fracture toughness data for the CA orientation only indicated that the K_{Idd} upper-shelf values are about 27 to 55 MN·m$^{-3/2}$ (25 to 50 ksi $\sqrt{\text{in.}}$) higher and that the K_{Idd} transition to upper shelf occurs at higher temperatures than the CA oriented K_{Icd} values. Again, the mid-wall material exhibited the highest K_{Idd} values and the outer surface the lowest.

Mager et al.* tested nine compact-tension (CT) specimens: six 22-mm-thick (0.85T) CT and three 102-mm-thick (4T) CT specimens obtained from the prolongation of vessel V-7 as shown in Fig. 2.8.

*Work sponsored by HSST program under UCCND Subcontract 3196 between Union Carbide Corporation and Westinghouse Electric Corporation

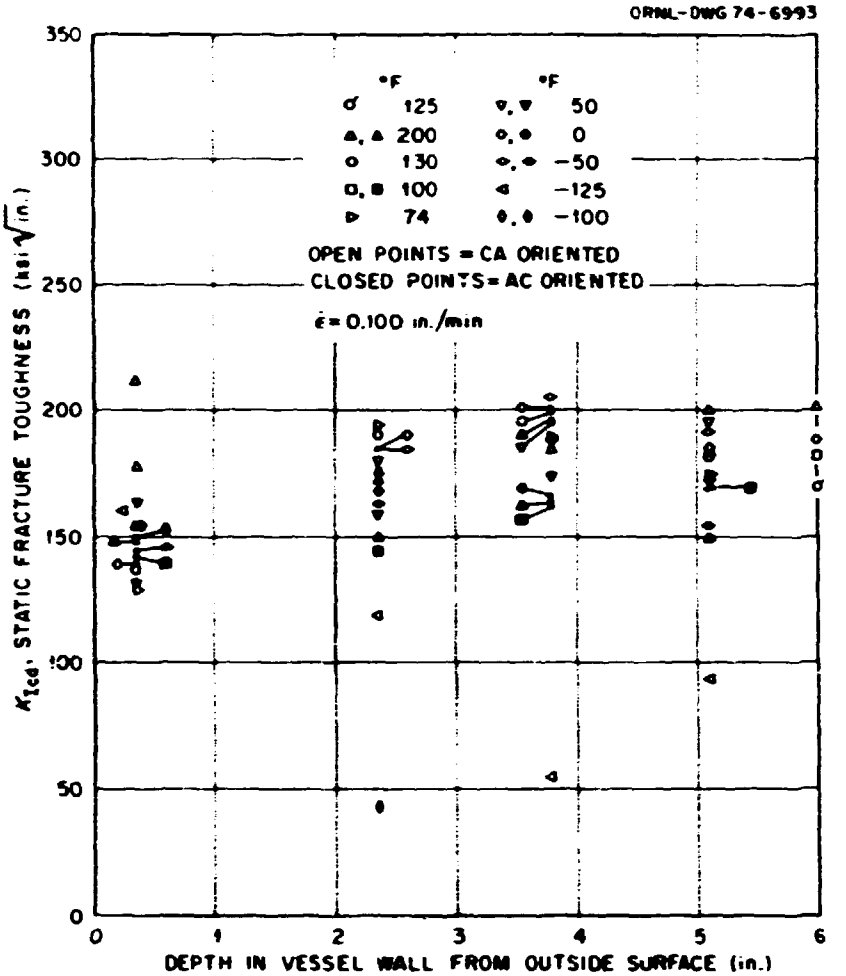

Fig. 2.13. Lower-bound fracture toughness values obtained from intermediate vessel V-7 using CA- and AC-oriented precracked Charpy-V specimens from 152-mm-thick (6-in.) ASTM A533, grade B, class 1 carbon steel.

All specimens were fatigue precracked according to the methods specified by ASTM.[8] A test temperature of 93°C (200°F) was specified in order to maximize the accuracy of the fracture toughness in the upper-shelf range with a minimum number of specimens. The test temperature of 93°C is near the onset of the upper-shelf range, where very large specimens (greater than 10T CT) would be necessary to perform valid fracture toughness testing according to the ASTM recommended procedure.[8] For this reason, the equivalent-energy concept[9,10] was used by Stelzman and Mager to interpret the data in terms of lower-bound values of the actual fracture toughness.

The fracture toughness data obtained by Mager for the prolongation material from intermediate test vessel V-7 are given in Table 2.5. The toughness of the base plate material from vessel V-7 is comparable to that of the forging prolongations of the first six intermediate vessels. Also, the fracture toughness through the thickness (inside surface, midthickness, and outside surface) of intermediate vessel V-7 appears to be homogeneous at 93°C.

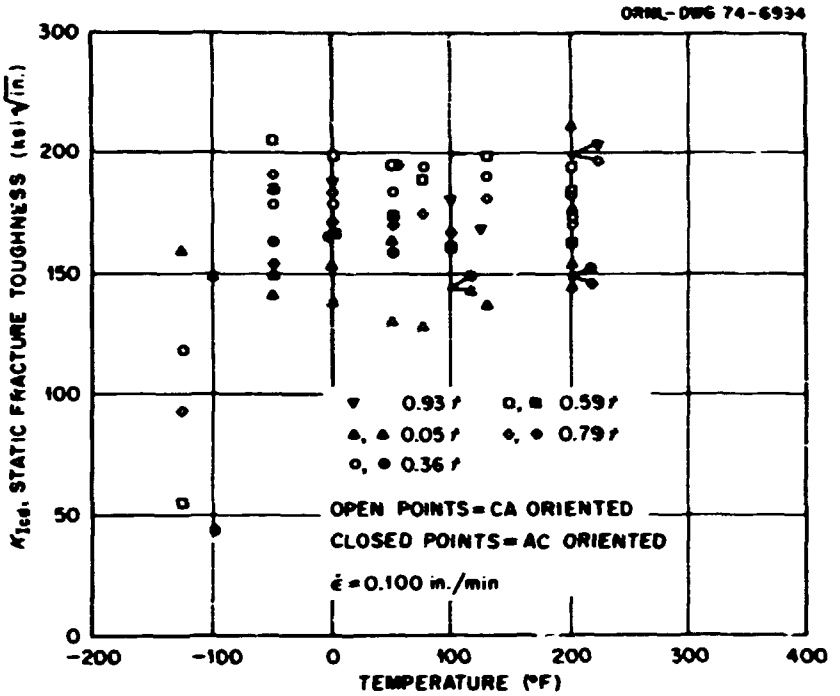

Fig. 2.14. Lower-bound fracture toughness values obtained from intermediate vessel V-7 using CA- and AC-oriented precracked Charpy-V specimens from 152-mm-thick (6-in.) ASTM A533, grade B, class 1 carbon steel.

Table 2.5. Fracture toughness results[a] determined from testing 0.85T and 4T CT specimens from HSST vessel V-7 at 93°C (200°F)

Specimen No.	Crack length (in.)	Maximum load (lb)	Energy to maximum load (in.-lb)	P_Q (lb)	Energy to P_Q (in.-lb)	K_{Icd} (ksi √in.)
0.850T CT specimens (outside surface)						
V7D-5	0.877	11,400	1,699.0	4,000	30.6	270.0
V7D-4	0.890	11,370	1,920.0	4,000	30.0	297.0
0.850T CT specimens (center thickness region)						
V7D-6	1.042	6,900	785.0	3,000	23.4	223.0
V7D-7	0.880	11,100	1,741.0	4,000	28.4	285.4
0.850T CT specimens (inside surface)						
V7D-8	0.885	11,500	1,877.0	4,000	30.0	291.0
V7D-9	0.963	9,400	1,785.0	4,000	35.0	306.6
4T CT specimen (inside surface)						
V7D-31	4.017	237,000	53,813.2	60,000	855.0	406.5
4T CT specimens (center thickness region)						
V7D-2C	4.130	214,000	42,310.2	60,000	810.0	386.7
V7D-1C	4.220	207,500	48,951.0	60,000	945.0	399.0

[a]Conversion factors: 0.85T = 21.6 mm thick; 4T = 101.6 mm thick; 1 in. = 25.4 mm; 1 lb force = 4.448N; 1 in.-lb = 0.11298 J; 1 ksi √in. = 1.0988 MN·m$^{-3/2}$.

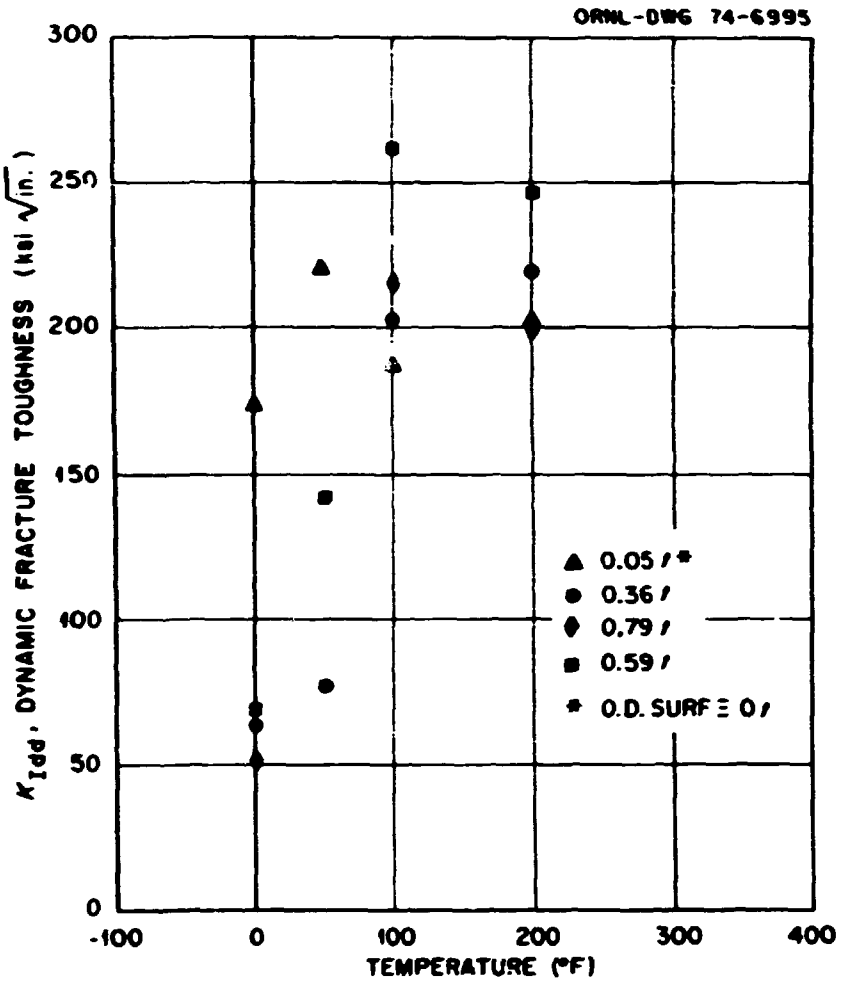

Fig. 2.15. Lower-bound fracture toughness values obtained from intermediate vessel V-7 using CA-oriented, precracked Charpy-V specimens from 152-mm-thick (6-in.) ASTM A533, grade B, class 1 carbon steel.

REFERENCES

1. R. W. Derby et al., *Test of 6-in.-thick Pressure Vessels. Series 1: Intermediate Test Vessels V-1 and V-2*, ORNL-4895 (February 1974).
2. C. E. Childress, *Fabrication and Mechanical Test Data for the Four 6-in.-thick Intermediate Test Vessels Made from Steel Plate for the Heavy-Section Steel Technology Program*, ORNL/TM-5074 (January 1976).
3. W. J. Stelzman, "Characterization of Intermediate Test Vessel Materials," *HSST Program Semiannu. Progr. Rep. Aug. 31, 1973*, ORNL-4971, pp. 66-74.
4. W. J. Stelzman, "Characterization of Intermediate Test Vessels," *Quart. Progr. Rep. Reactor Safety Programs Sponsored by the Division of Reactor Safety Research for April-June 1974*, ORNL/TM-4655, Vol. II, pp. 56-66.

5. T. R. Mager et al., "Fracture Toughness Characterization of HSST Intermediate Pressure Vessel Material." *HSST Program Semiannu. Progr. Rep. Aug. 31, 1973*, ORNL-4971, pp. 74–79.
6. T. R. Mager et al., "Fracture Toughness Characterization of HSST Intermediate Pressure Vessel Material." *Quart. Progr. Rep. Reactor Safety Programs Sponsored by the Division of Reactor Safety Research for April–June 1974*, ORNL/TM-4655, Vol. II, pp. 66–67.
7. T. R. Mager et al., *Fracture Toughness Characterization of HSST Intermediate Pressure Vessel Material*, HSSTP-TR-38 (WCAP-8456), Westinghouse Electric Corporation, Pittsburgh, Pa. (December 1974).
8. *Tentative Method of Test for Plane-Strain Fracture Toughness of Metallic Materials*, ASTM E399-70T.
9. F. J. Witt, "A Procedure for Determining Bounding Values on Fracture Toughness K_{Ic} at Any Temperature," HSST 5th Annual Information Meeting, Paper 13, March 1971.
10. F. J. Witt and T. R. Mager, *A Procedure for Determining Bounding Values on Fracture Toughness K_{Ic} at Any Temperature*, ORNL/TM-3894 (October 1972).

3. Flaw Preparation

INTRODUCTION

One phase of investigation in the HSST program requires that cracks of known size, location, and orientation be grown in the walls of massive steel containers or vessels to simulate the effects of flaws. The flaw characteristics are needed for the application of fracture mechanics and can be studied by means of analytical stress and strain procedures and by ultrasonic and acoustic sound-emission techniques.

Cracks can be grown by two techniques. One is based on mechanical techniques and involves the use of high-pressure pulsating fluids to fatigue the metal of the vessel. By this technique flaws are sharpened by cyclic notch pressurization applied by high-pressure hydraulic pumping equipment. The other method is based on metallurgical principles and involves the combination of electron-beam (EB) or laser-beam welding with an electrochemical process to crack the weld by hydrogen charging. Flaws of uniform depth can be produced by the welding method, whereas mechanically produced flaws tend to exhibit elliptical bottom contours with some minor depth variation.

The flaws in many tensile specimens and in the first six prototype pressure vessels of the HSST program were successfully sharpened by cyclic notch pressurization, because the flaw shape was specifically chosen so that the majority of the crack front would grow in a nearly uniform manner under cyclic pressure. However, the extension of this procedure to other crack shapes, such as long surface cracks, is extremely difficult because the crack front tends to grow nonuniformly. A long notch also presents seal-off problems for effective pumping. Furthermore, the pumping equipment presently available for cyclically pressurizing large flaws is inadequate, and the acquisition of additional equipment would have entailed long-term delays and expensive pump development. The combination of electron-beam welding and electrochemical hydrogen charging is not limited by the length of the flaw and offers uniform, sharp crack flawing capabilities for all machinable shapes. This method was selected for vessel V-7 and, following a concentrated development effort, provided the means to successfully produce the sharp crack in the vessel.

MECHANICAL FLAWING METHOD

In the mechanical method of flaw sharpening a test specimen, a suitable slot is machined into the vessel wall, a mold replication of the machined notch volume is made for templating shim stock to dimensionally conform to the notch, and the shim stock is inserted to fill the entire notch volume except for the contact surface contour line at the root of the notch. The notch is then sealed by a block welded or clamped to the test specimen, and the volume to be cyclically pressurized is connected to a pressurizing system. Figure 3.1 illustrates the schematics of a high-pressure hydraulic pumping system.

METALLURGICAL FLAWING METHOD

Any metallurgical method approach for growing flaws in low-alloy high-strength steel materials is premised on the role of hydrogen in the formation of cracks in ferritic materials. It is a well known fact that hydrogen is responsible for underbead cracking in the heat-affected zones of ferritic weldments; the cracking is associated with stresses and microstructure. It is also known that martensite offers a suitable microstructure for such cracking. Martensite can be produced in these steels by rapidly cooling them from the austenitic temperature range. This can be accomplished by placing an autogenous electron- or laser-beam weld at the surface of the steel to be flawed. Such welds assure the concentration of weld heat to a small region so as to establish the

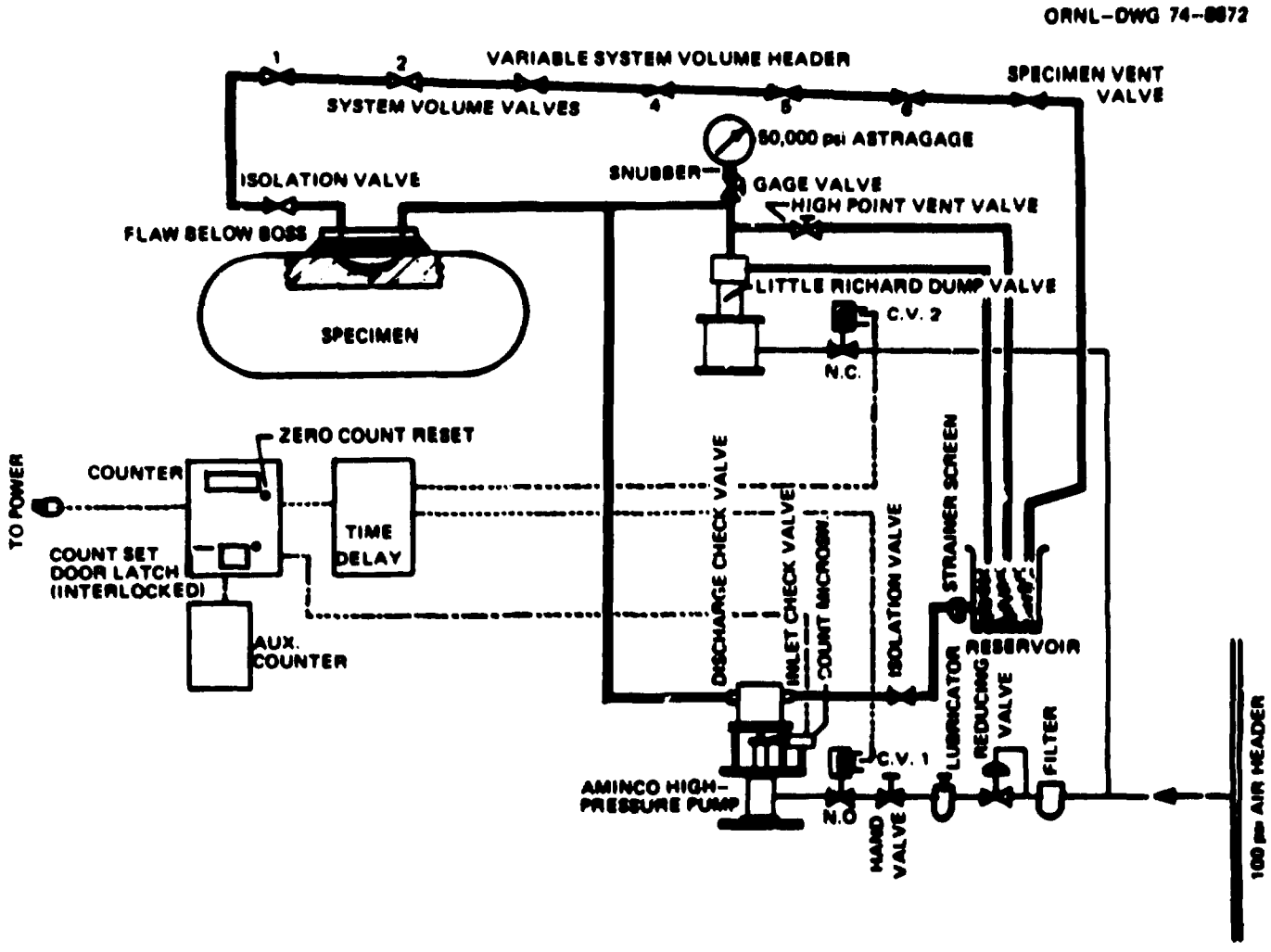

Fig. 3.1. High-pressure hydraulic pumping system for pump-dump cycling.

conditions for the required rapid cooling. Concentrating the heat also results in residual stresses of yield point magnitude existing contained within a very narrow band. The final requirement for cracking is the presence of hydrogen, which can be "pumped" electrochemically into the weld metal by submerging the weld in a 10% H_2SO_4 solution that serves as the electrolyte. The specimen is masked so that only the weld contacts the electrolyte. An electrode is immersed in the electrolyte, and the system is wired so that the specimen weld acts as the cathode. The arrangement is shown in Fig. 3.2. A current density of about 7.8×10^{-4} A mm^{-2} (5 A in.$^{-2}$) of unmasked area is generally sufficient to cause cracking within a few hours. A room-temperature vulcanizing material is used for the masking medium and to form a pool for the electrolyte.

Cracks formed by hydrogen-charging electron- or laser-beam welds are quite similar to those produced by mechanical flawing techniques. The cracks propagate through the weld metal and heat-affected zone and terminate very near the end of the weld zone. The width of the cracks at any cross section for both the mechanical or metallurgical flawing methods approaches the thickness of a hair, or about 0.05 mm (0.002 in.). Crack depths can be made to vary up to a maximum distance of about 13 mm (½ in.) as a function of weld power output.

The EB welding parameters that affect the cooling rate of an autogenous weld bead are the heat sink offered by the specimen, total weld power, the welding speed, and the gas purge surface cooling. Electron-beam welding within a vacuum cell eliminates the need for a gas purge and adds weld focus to the list of parameters. Focus, power, and speed are the parameters that control weld penetration depth and bead contour. Bead contour governs the rate of cooldown for any given weld speed.

Bead shape must be resolved experimentally by trying various distance and sharp focus combinations for a variety of settings suitable for a longitudinal weld path. Since a narrow pear-shaped bead has more side surface contact than a thick ball-shaped bead, the pear-shaped bead (see Fig. 3.2) is best for dissipating weld heat and restricting the size of the heat-affected zone. The pear-shaped cross section can be achieved with the sharpest possible focus for a given EB torch-to-work setting and preselected beam accelerating potential. Focusing circuit current settings are determined for sharp focus by visually observing the size and brilliance of the spot where all weld beam rays intersect the top surface of the work while operating the EB gun at full preselected weld voltage and minimum EB current, usually from 10 to 25 mA.

Figure 3.3 illustrates the variation of weld penetration as a function of changes in focusing current settings (at constant torch-to-work distance) for EB welds on A533, grade B, class 1 steel plate. However, test results indicated that an optimum final focusing current setting, for best repetitive welding results, should be 0.003 to 0.005 A to either side of the sharp focus, with the beam focused above the surface preferred. Programming the actual sharp focus setting appeared to magnify weld penetration spiking so as to cause voids at the bottom of the weld, possibly as a result of surface conditions of the specimen. Final bead refinements are then possible by experimenting with different current-speed combinations for determining optimum bead shape for a preselected average weld penetrating depth. The optimum cross-sectional contour will exhibit a high depth-to-width ratio with a moderately spiked tail of the bottom. Such a spiked bottom is ideal for eventual flaw growth.

The line separating the fused and unfused zones in a longitudinal sectional view of an autogenous EB weld in steel plate exhibits a spiked profile. The peaks and valleys vary up to about 12% of the average weld penetration depth. The spikes are closely spaced, random, and nonsymmetrical and are about 0.2 to 0.5 mm (0.001 to 0.002 in.) wide.

FLAW PREPARATION OF VESSEL V-7

The flaw selected for V-7 was an external trapezoidal surface flaw having machined dimensions of 457-mm (18-in.) surface length, a depth of 127 mm (5 in.), and a bottom length of 203 mm (8 in.) as shown in Fig. 3.4.

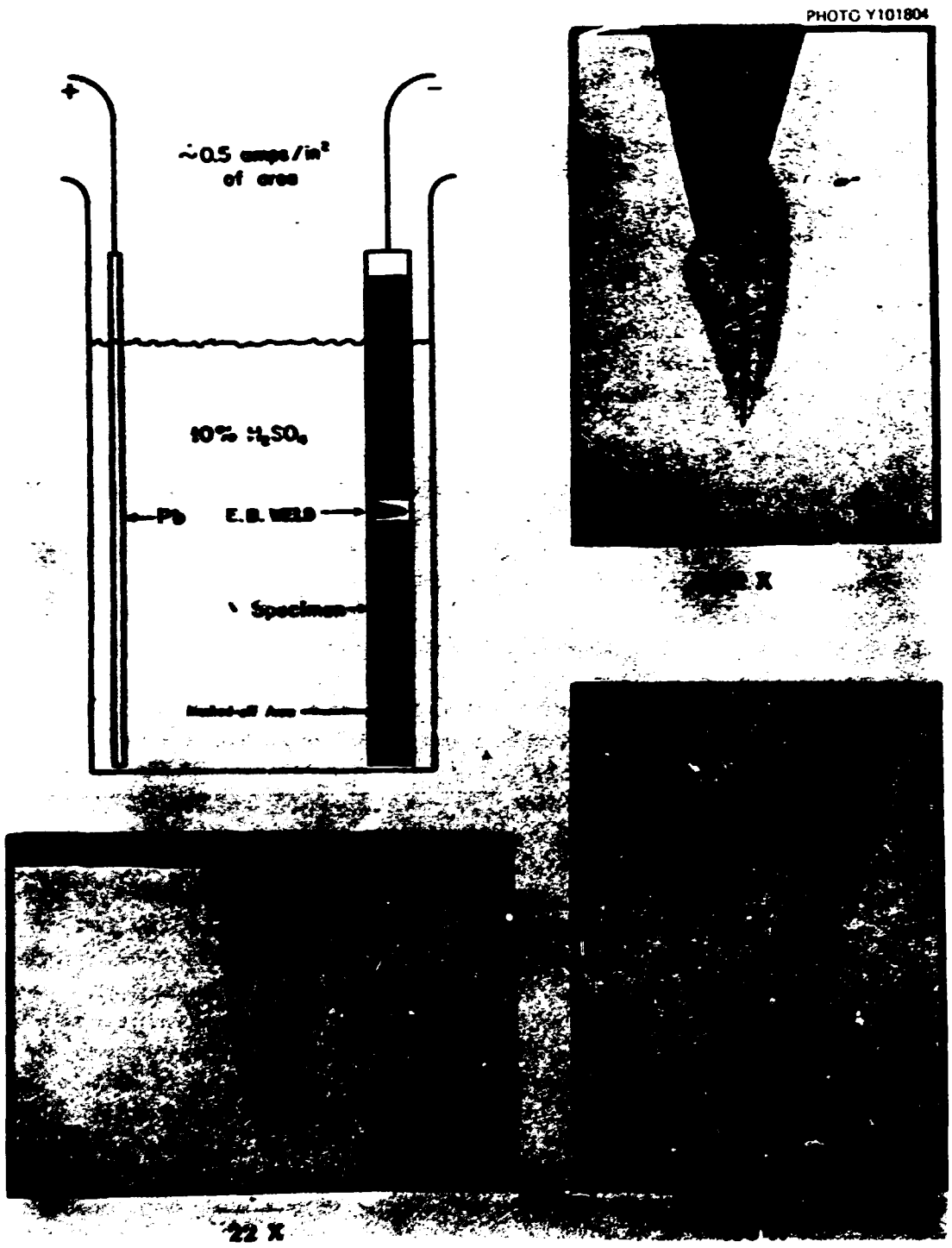

Fig. 3.2. Illustration of the process employed in the production of hydrogen-induced cracks in low-alloy high-strength steels. The photomicrographs were taken from specimens cracked by this technique (18% reduction).

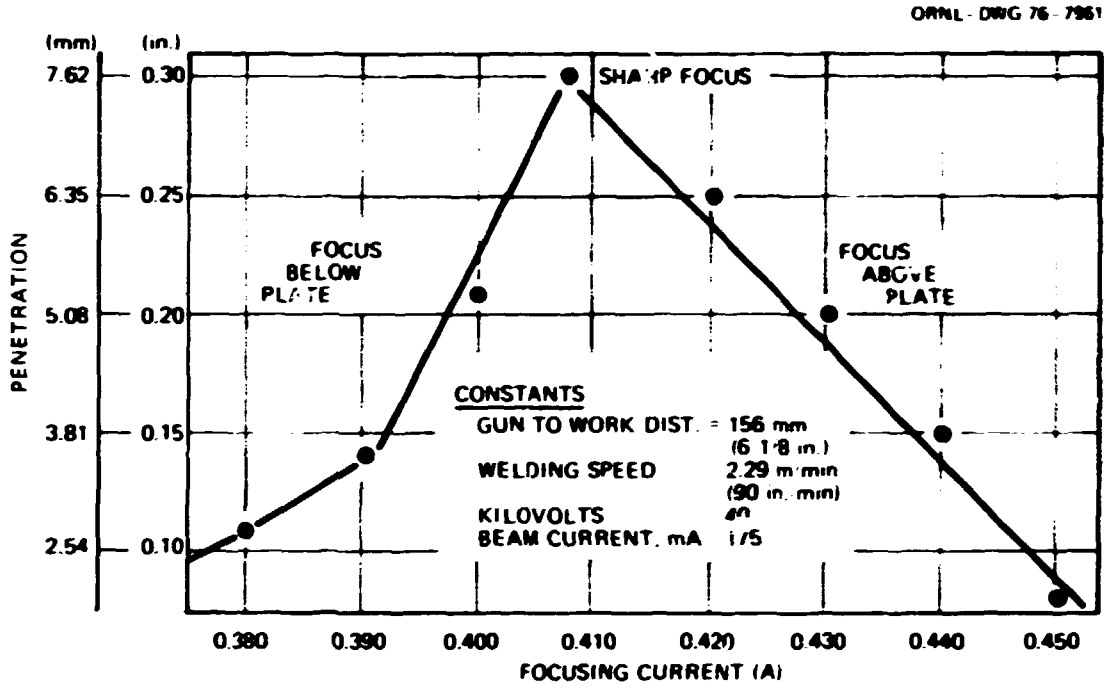

Fig. 3.3. Partial penetration autogenous electron-beam welds on A533, grade B, class 1 steel plate.

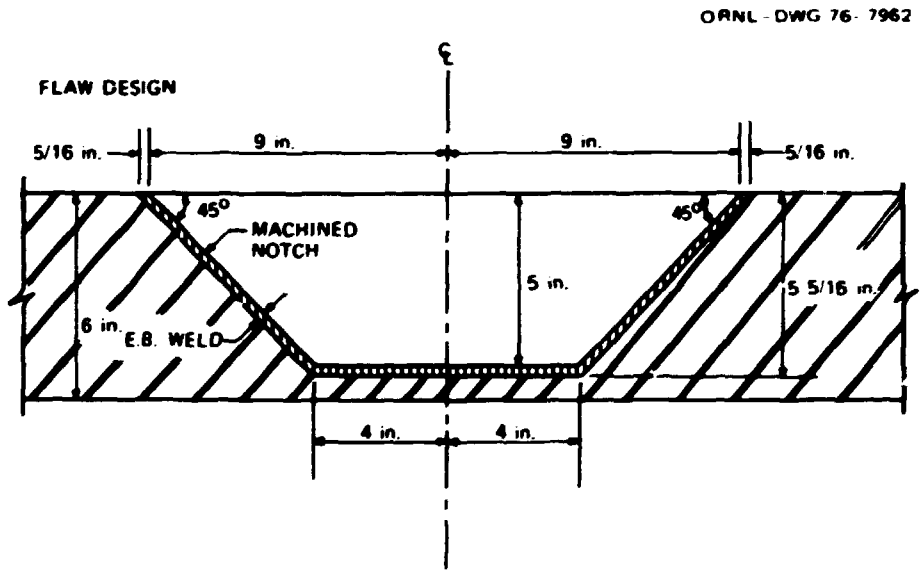

Fig. 3.4. Flaw design for HSST program intermediate test vessel V-7.

The flaw was sharpened by EB welding and hydrogen charging to an additional depth of about 8 mm (5/16 in.). The depth of the EB weld determines the nominal depth of the sharp crack. Hence, welding parameters that consistently gave the desired depth in trial welds were applied to the vessel itself.

The welding was performed in the ERDA-owned 2.7 × 1.6 × 2.3 m (108 × 62 × 92 in.) model VX Sciaky weld chamber in Oak Ridge. The floor of the chamber required the addition of load-distributing beams to properly support the 7.6 t (8½-ton) vessel weight (less head) without buckling. A cross-braced dual-beam track was built for transferring the vessel load to four adequately anchored chamber posts. The dual beams were also employed as skid rail tracks for transferring the vessel into and out of the chamber. An existing carrier dolly was altered to have corresponding beams mate and couple with the chamber track beams, and "[illegible]-alongs" were used to facilitate vessel movement from the carrier to the chamber. Figures 3.5 and 3.6 show the vessel entry into the chamber.

Hydrogen-charged EB welds had previously been used successfully to produce sharp cracks in miniature scale models of both tensile specimens and pressure vessels. The earlier work was performed on plate materials up to 25.4 mm (1 in.) thick employing a Hamilton Standard 0.91 × 0.76 × 0.76 m (36 × 30 × 30 in.) high-voltage EB weld chamber with 110 kV and 10 mA nominal weld power input at slow weld speeds. High-voltage EB welders are preferred because for like power output, the lower the weld current, the cooler the weld, the smaller the heat-affected zones, which result in a spiked weld bead with a low width-to-depth ratio. There were no high-voltage EB weld chambers available for flawing vessel V-7.

To assure satisfactory results in sharpening the notch in vessel V-7, an EB welding development program was organized and conducted. A 156-mm (6⅛-in.) torch-to-work distance on 40 kV welding voltage was selected. Thus the gun would ride approximately 25.4 mm (1 in.) above the outside surface of the vessel. Initial trials were run on flat plates to find amenable current-speed range combinations for welding the bottom flat portion of the trapezoid, and a current range of 150 to 180 mA and a speed range of 2.0 to 2.3 m/min (80 to 90 in./min) were selected. Follow-up trials were then held on flat plates set at 45° angles to simulate the trapezoidal side slopes. It was determined that it was necessary to integrate both horizontal and vertical torch travel at like speeds to obtain a resultant slope surface welding speed about equal to the speed selected for the groove bottom. Trials on combination flat plates placed horizontally and at 45° slopes and tack welded at their junctions established techniques for overlapping welds at the bottom trapezoid corner. It is imperative that welding be uphill to keep the weld puddle behind the weld beam because gravity in downhill welding causes the puddle to advance into the weld arc. Therefore, the trapezoid had to be welded in two segments: a combined horizontal and uphill slant weld, and a second slant weld with minimum horizontal run to overlap the first weld near one trapezoid corner. An overlap of 10 to 13 mm (⅜ to ½ in.) was necessary to retain uniform weld depth control when programming constant weld speed travel off the tungsten starter target at full welding current without using current upslope regulations.

Repeat trials were pursued on 152-mm-thick (6-in.) A533 materials with a slot 25 mm (1 in.) wide × 127 mm (5 in.) deep, as shown in the right view of Fig. 3.7, to investigate for weld beam distortion and beam attachment to the groove sides. Magnetic beam distortions were noted, especially where the slots were not perfectly balanced within the specimens or where the weld path was not well centered within the slot. Insertions of 0.1-mm-thick (5-mil) sheets of a soft-iron shielding material to groove sides to reduce or negate the effects from uneven magnetic distributions within the A533 work materials proved to be of little value. Handling and attachment difficulties prevailed and produced new problems, including frequent weld contamination where liners overheated or slipped. However, gaussmeter checks of a final prototype block (Fig. 3.7 left view) and of vessel V-7 indicated fairly even magnetic field distributions for both units. It was decided to purposely offset the weld bead in the prototype ±1.6 mm (1/16 in.) off the true center line of the slot by

Fig. 3.5. View of intermediate vessel V-7 entering the Scinky weld chamber.

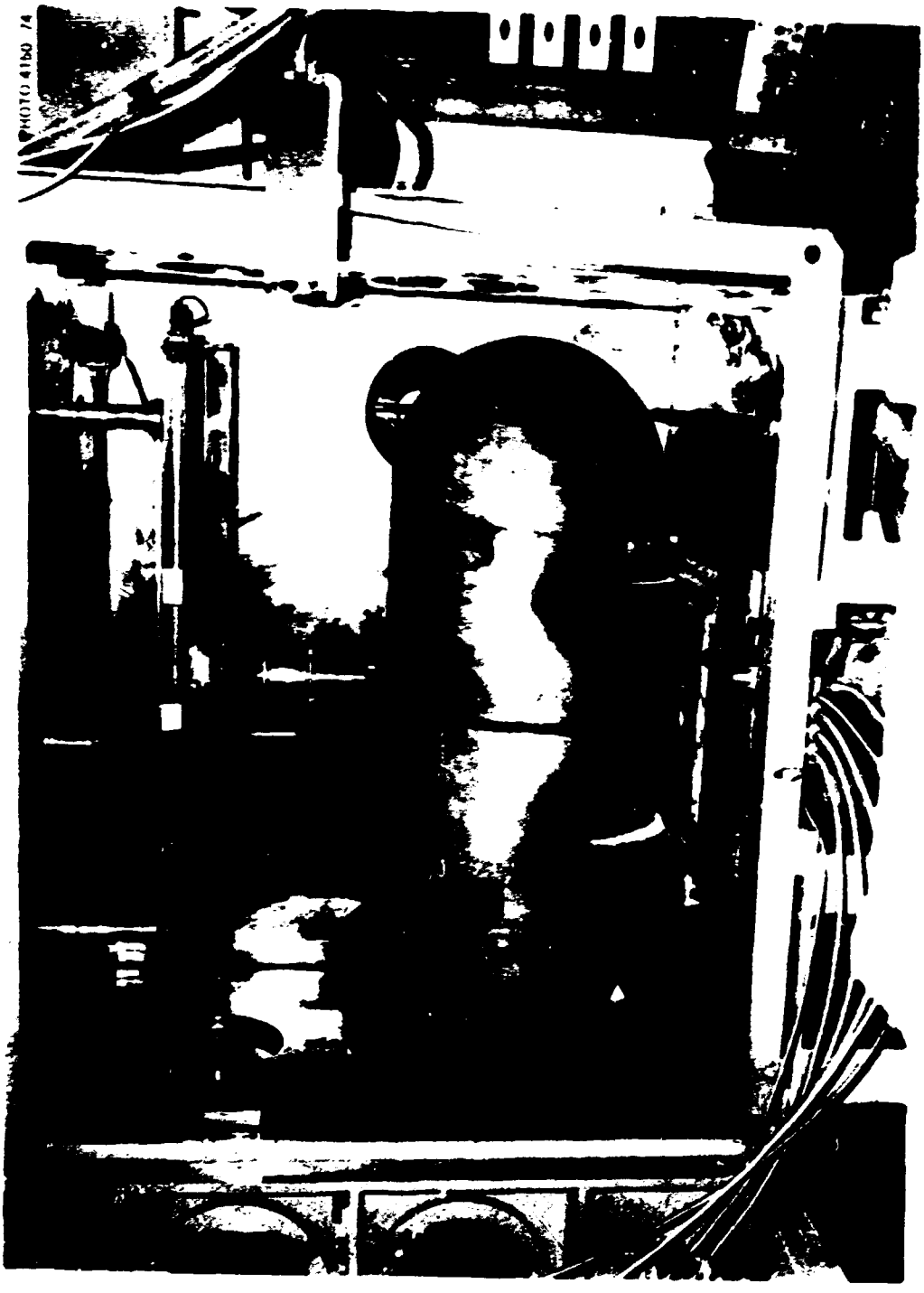

Fig. 3.6. Intermediate vessel V 7 inside the electron-beam weld chamber.

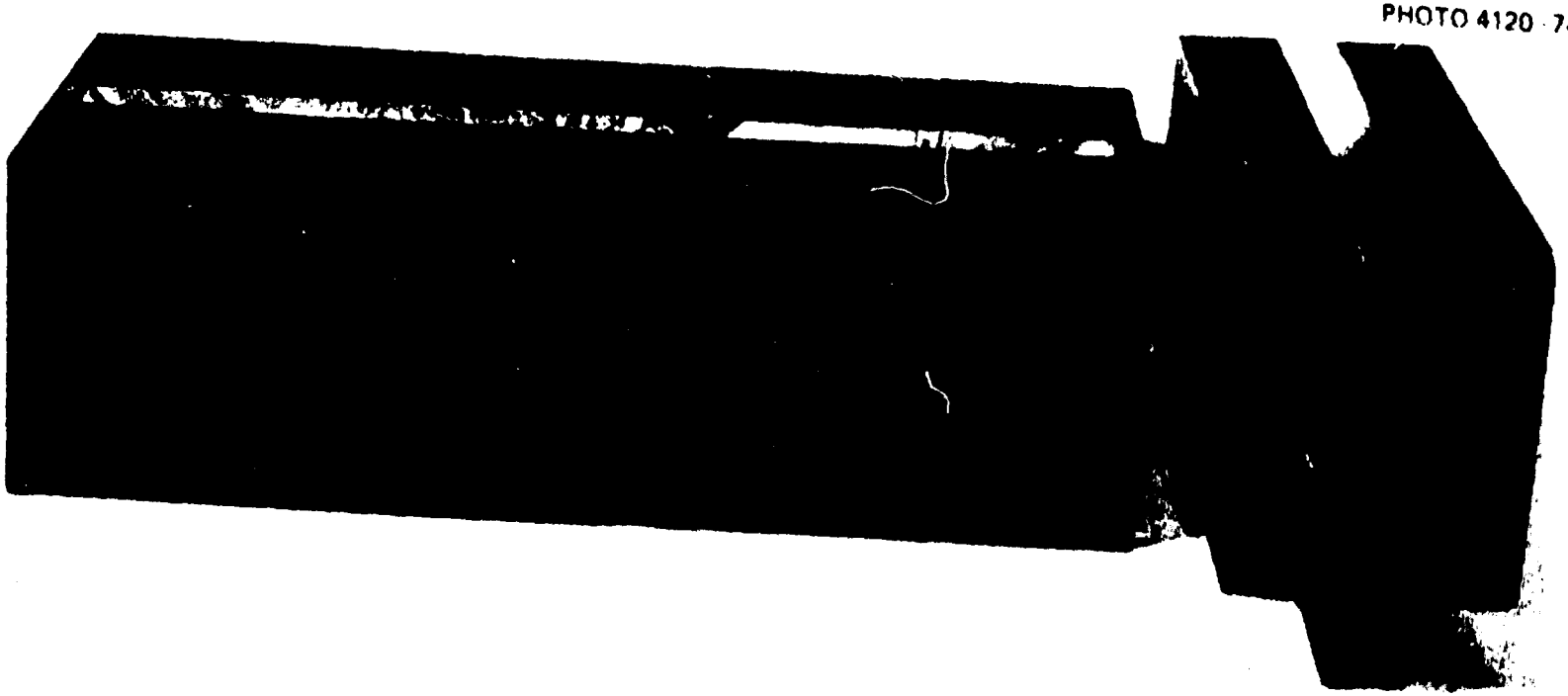

Fig. 3.7. Prototype blocks for flawing vessel V-7 by cracking electron-beam welds by hydrogen charging.

rotating the specimen about its longitudinal center. The resultant weld "pulled" no more than 4 mm ($^5/_{32}$ in.) from its actual center line. The V-7 weld slot was actually centered somewhat better; the autogenous bead in V-7 deviated less than 3 mm ($^1/_8$ in.) from the true center line.

The prototype blocks also served to develop the tooling and machining techniques used to machine the deep notch in V-7 with a large horizontal boring mill.

The autogenous EB weld bead was formed successfully on vessel V-7 on May 2, 1974. Welding parameters were as follows:

Power: 40 kV and 180 mA on horizontal surface and 135 mA on slopes.

Surface speed: 2.3 m/min (90 in./min).

Average bead contour: 3-mm ($^1/_8$-in.) surface width and 8-mm ($^5/_{16}$-in.) penetration.

Chamber vacuum: 0.67×10^{-3} Pa (5×10^{-6} torr).

During hydrogen charging of the EB weld, it is imperative that the time of cracking be known in order to know when to remove the acid electrotype. Prolonged acid exposure to a cracked weld tends to widen an otherwise hairline crack. Two techniques can be applied to monitor a weld during charging: acoustic-emission monitoring and a pulse-echo ultrasonic setup with multiple transducer pickups strategically placed about the weld. Composite Fig. 3.8 illustrates the ultrasonic and acoustic-emission setup used to detect EB weld cracking for both the prototype and the actual vessel. The ultrasonic devices confirm cracks at their respective positions and are helpful in monitoring crack growth, which, in these cases, started at approximately the longitudinal center of the weld and progressed toward both ends. Acoustic-emission signals register continuous crack growth; the frequency of emission in the prototype weld differed radically from that of the actual vessel weld. It had been hoped that the emission information obtained from the prototype specimen would furnish guidance for subsequent vessel monitoring. The different acoustic-emission characteristics shown in Fig. 3.8 may be attributable to overall shape and restraint factors which differ greatly between specimen and vessel. More experimentation will be required before more conclusive interpretations can be reached. The final and most conclusive confirmation that cracking has occurred by electrolytic hydrogen charging is by detailed microscopic visual observation. It entails emptying the electrolyte and drying the surface of the weld bead; hence it is impractical except during the latter stages of the charging operation. We have noted that whenever cracks do show up on the weld surface, they then extend throughout the entire weld depth.

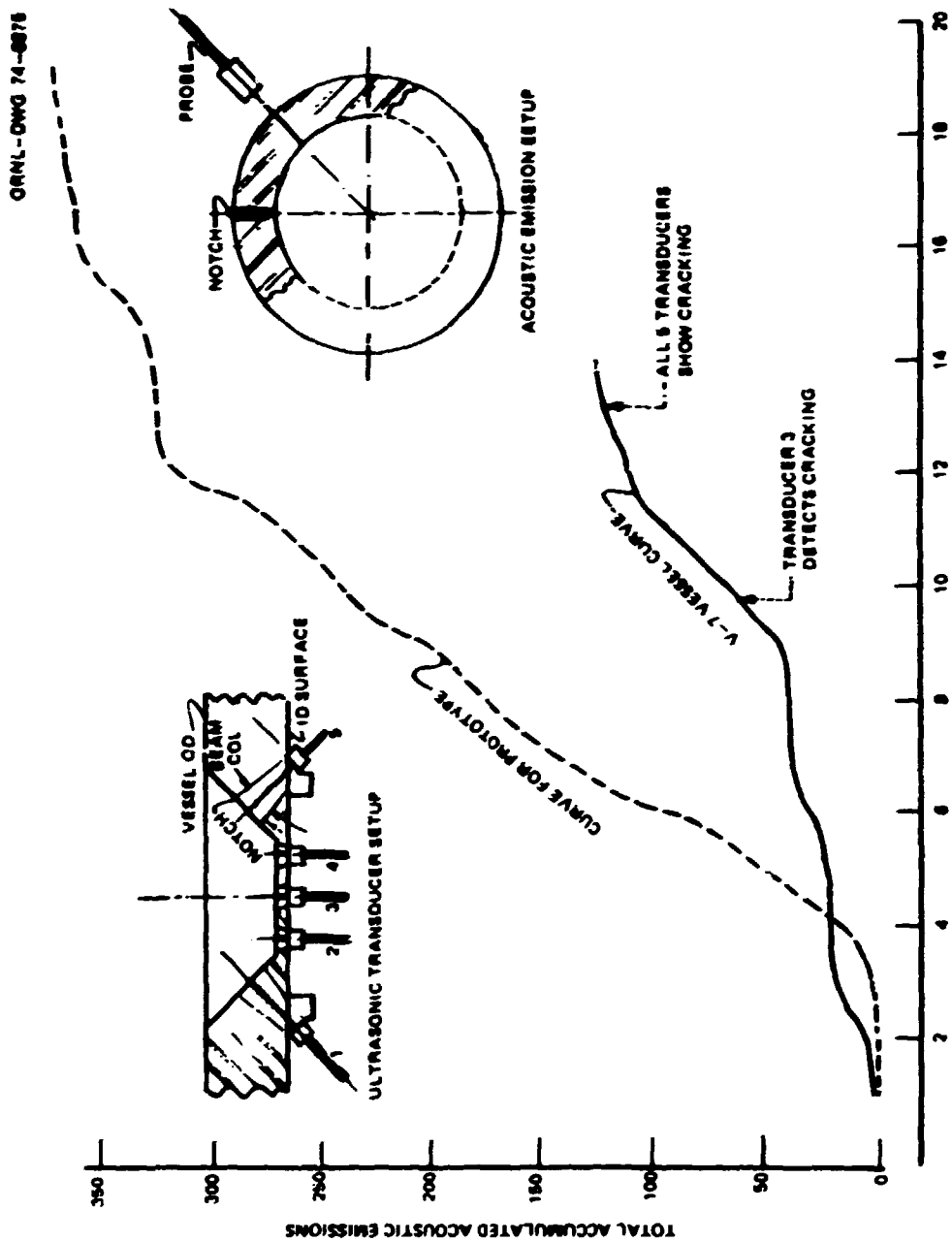

Fig. 3.8. Weld crack monitor arrangements.

4. Test Facility Design and Performance

TEST FACILITY

The test site for intermediate test vessel V-7 was the same as that used for all other vessels.[1,2] The criteria for site selection and design along with a detailed description of the facility are given in Ref. 2. The site is located at the old power plant adjacent to the Oak Ridge Gaseous Diffusion Plant (ORGDP), where the vessels were pressurized to failure in a concrete bunkered cell that was converted from an old steam turbine foundation. A sectional view of the test pit is shown in Fig. 4.1, and a typical overhead view of a test vessel in the pit is shown in Fig. 4.2.

The test facility is capable of controlling vessel temperatures from 46 to 177°C (50 to 350°F) and pressurization output to 345 MPa (50,000 psi). Figure 4.3 is a schematic flow diagram of the facility.

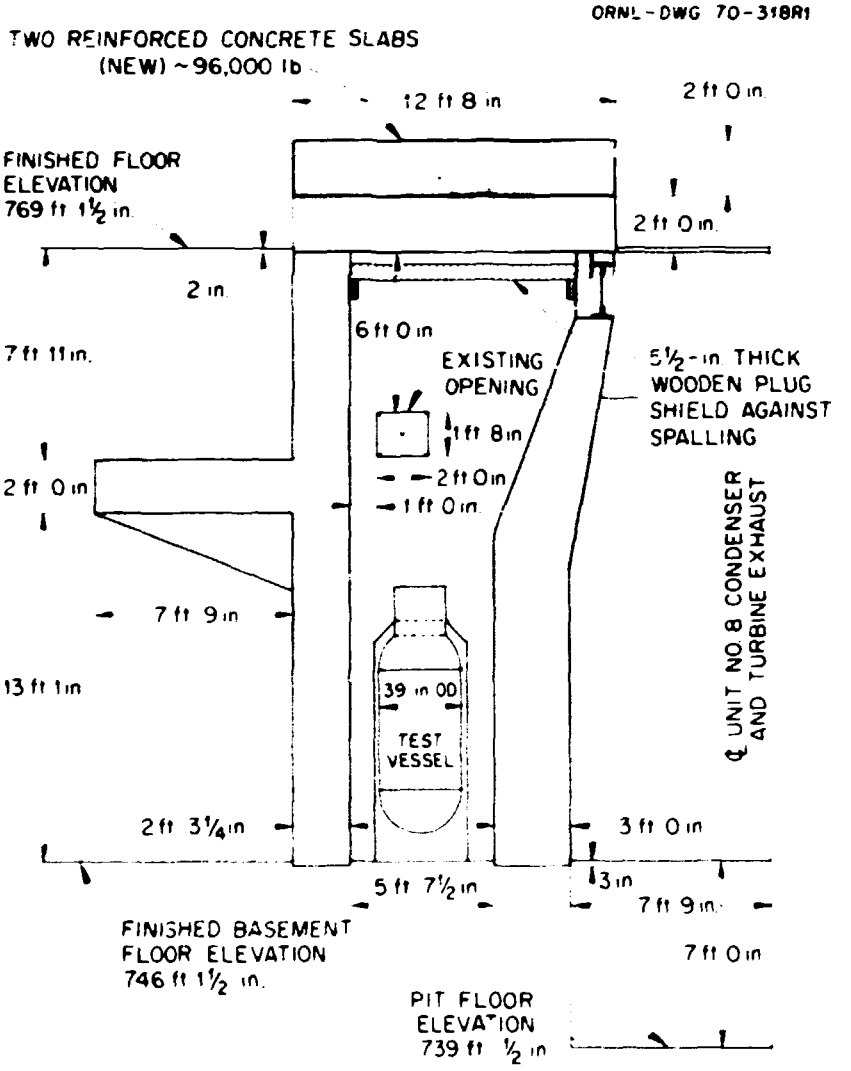

Fig. 4.1. Sectional view of intermediate vessel test pit.

Fig. 4.2. View of test pit from turbine room floor with a typical vessel and associated equipment in place.

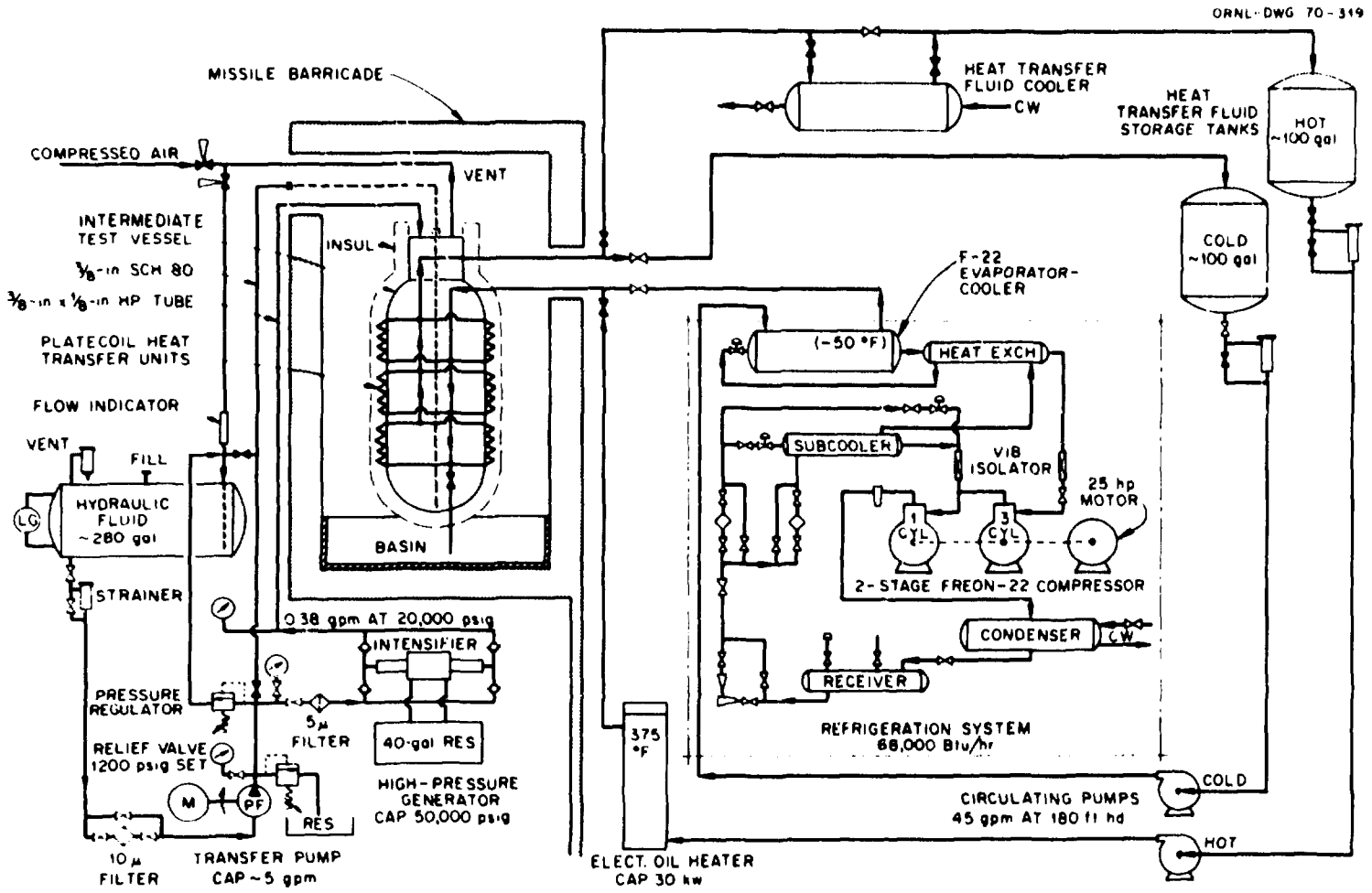

Fig. 4.3. Schematic flow diagram of intermediate vessel test facility.

INSTRUMENTATION

Five types of measurements of vessel behavior were made on test vessel V-7. The location of thermocouples, strain gages, crack-opening-displacement (COD) transducers, and ultrasonic sensors are shown in Fig. 4.4. Acoustic-emission sensors were installed and measurements taken by Dunegan/Endevco and Westinghouse. The report of Dunegan/Endevco is included as Appendix D, and ultrasonic instruments and results are discussed separately later in this chapter.

There were 14 Chromel-Alumel thermocouples used to monitor vessel temperature and insure the adequacy of the prescribed test conditions in the regions of interest. Multipoint Brown (Honeywell) recorders were used to record temperatures.

The inner and outer surfaces of vessel V-7 were instrumented with 66 strain gages. Two types of strain gages were used: Micromeasurements type EP-08-250-120 and Ailtech type SG-125. The Micromeasurements foil gages are made from annealed Constantan foil on a flexible polyamide back and are used primarily where large strains are to be encountered. They were installed using M-Bond 200 cement. The Ailtech (Microdot) weldable gages utilize nickel-chrome gage elements encapsulated in stainless steel with MgO insulation. They are spot welded in place and have MgO insulated stainless steel integral leads. The gage qualification and installation procedures were presented in Refs. 1 and 2. A Datum System 70 computer-controlled data-acquisition system (DAS) and portable BLH strain indicators were used to record the strain data. A complete tabulation of strains is given in Appendix B.

Crack-opening-displacement (COD) measurements were made at three locations along the crack. Transtek linear displacement transducers, model 354-000, were mounted in clevis supports as shown in Fig. 4.5. These transducers, which are self-oscillating and demodulating direct-current differential transformers (DCDT), were used as backup devices on vessel V-4 and were evaluated during that test.[1] The data from these COD sensors were also recorded by means of the DAS.

As in the previous tests, two completely independent systems were used to monitor pressure. A closed-circuit television system was used to directly view a conventional Bourdon pressure gage mounted near the high-pressure pump. This was a backup to a more precise system that consisted of a strain-gage-based pressure transducer, a signal-conditioning system, and an L&N recorder. After calibration at a standards laboratory, this device was accurate to ±1.72 MPa (250 psi) in a range of 207 MPa (30,000 psi).

Scanning closed-circuit television systems were also utilized for general surveillance of the test pit and pressurization equipment. A close-up view of the flaw was recorded by means of video tape during the test.

TEST PROCEDURES

Vessel Preparation

After the vessel was flawed (see Chapter 3), it was transported to another Y-12 facility of the Reactor Division for instrumentation.[2] After all inside and part of the outside instrumentation was complete, the head was installed and the vessel sealed. The vessel was then moved to the test site and installed in the test pit. Figure 4.6 shows the instrumented vessel after exterior instrumentation was complete. Heating-cooling plates were installed, the instrumentation lead wires to the control room were connected, and insulation was applied to the vessel. It was then ready to be filled with demineralized water, followed by the connection of the pressurization lines. During the filling operation and while the vessel was being brought to the test temperature, installation of television, acoustic-emission, and ultrasonic monitoring equipment was completed. After final checks on all recording equipment, the vessel was ready to test.

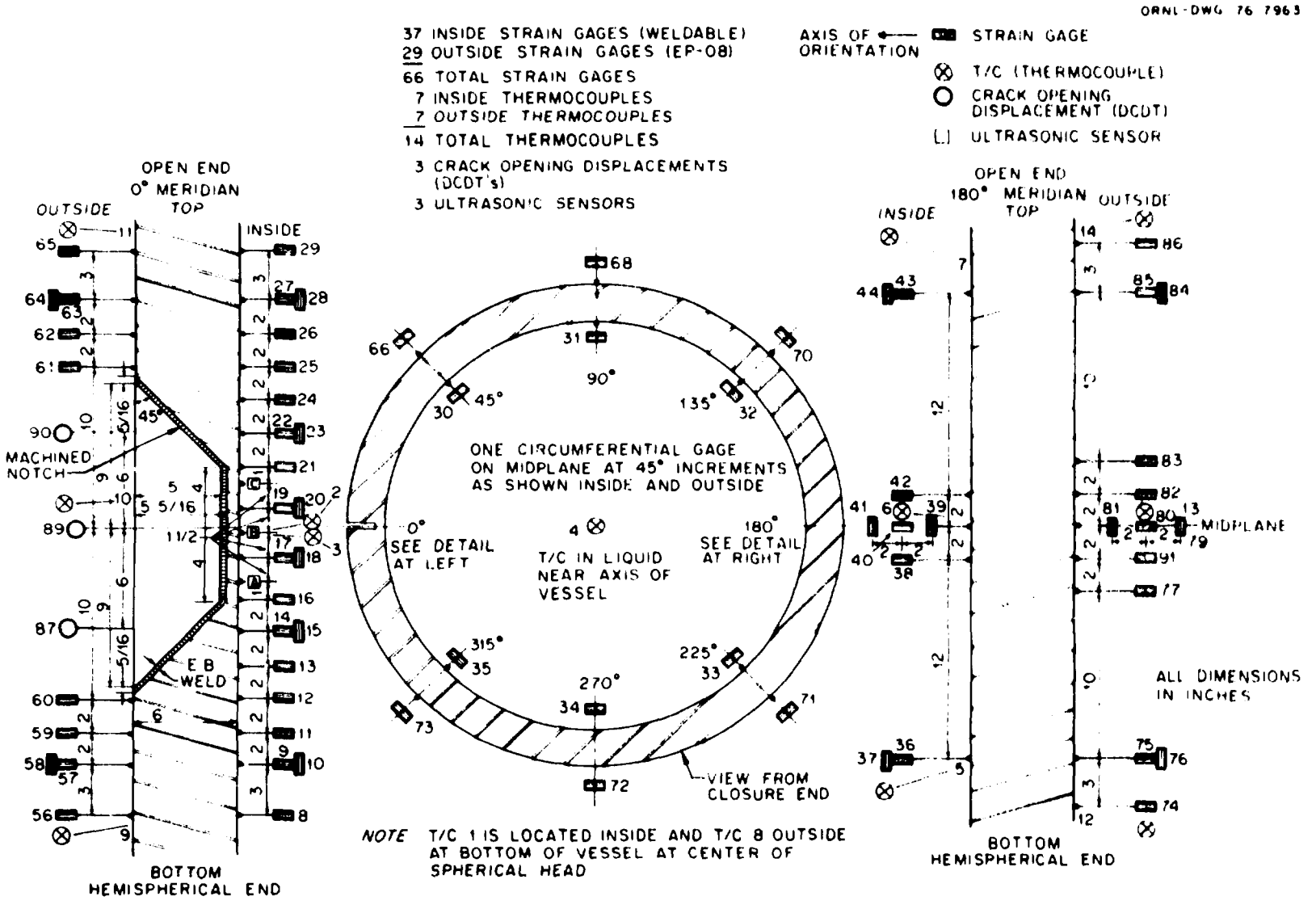

Fig. 4.4. Location of instrumentation on intermediate test vessel V-7.

Fig. 4.5. Crack-opening displacement transducers mounted on test vessel V-7.

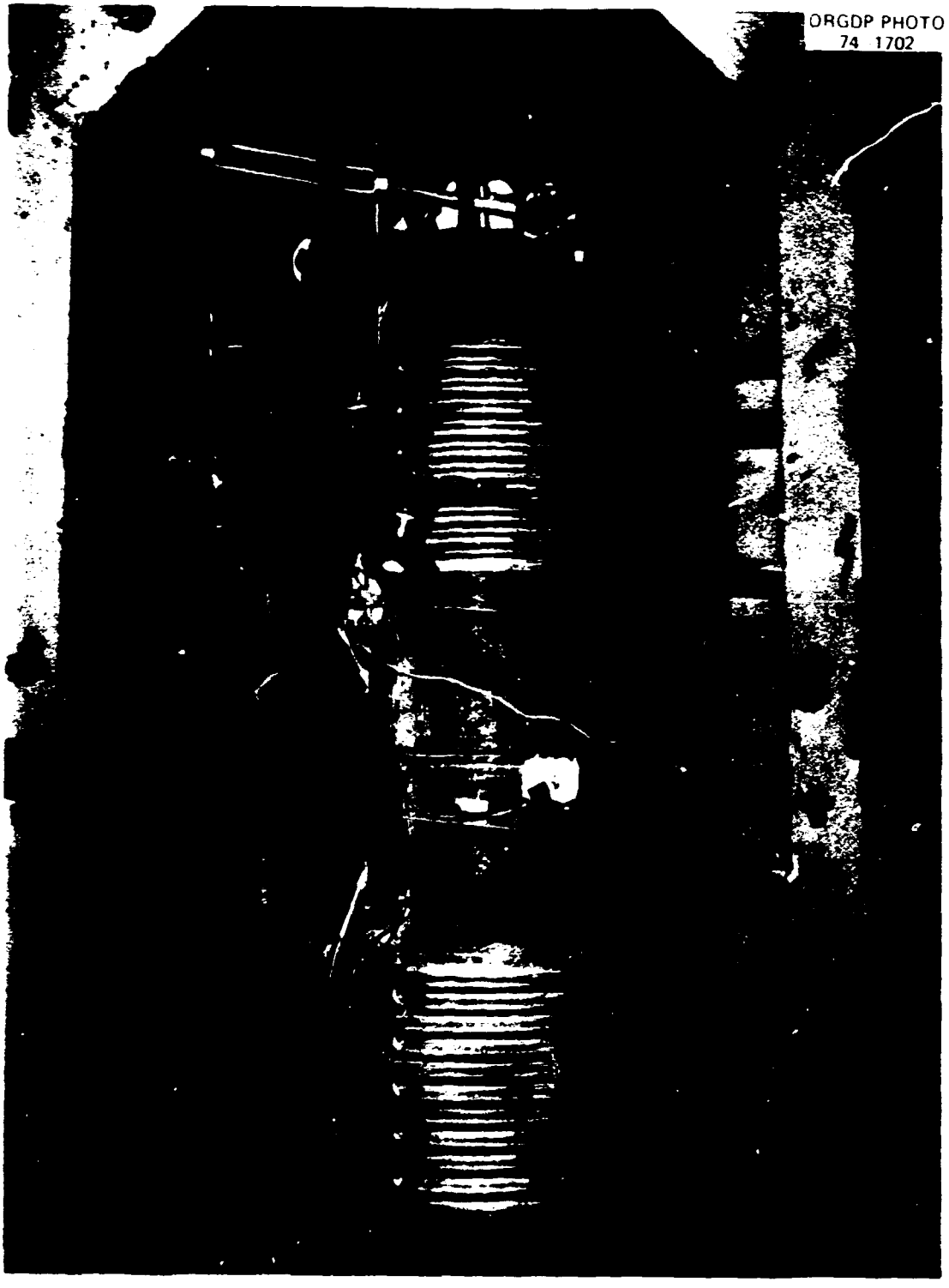

Fig. 4.6. Instrumented test vessel V-7 in test pit.

Pressure Testing

The vessel was brought slowly to the testing temperature. A time-vs-temperature plot for a thermocouple located near the flaw is shown in Fig. 4.7. An initial zero pressure data run was recorded, and pressurization was started. Periodic hold times were scheduled during which a complete set of data was taken. These holds were set at 6.9-MPa (1000-psi) intervals until 124 MPa (18,000 psi) was reached, at which point the pressure was raised in smaller increments until failure. Often, more than one set of data were taken during a hold period, during which the pressure dropped due to crack extension, localized yielding, and compliance of the pressurizing system at high pressure. Immediately following a leak at the flaw, data were recorded on important gages until the crack closed and sealed at about 129 MPa (18,700 psi). The pressure-vs-time function is shown in Fig. 4.8. A final set of data was recorded from surviving instrumentation after failure.

Ultrasonic Monitoring

Crack growth during the test was monitored by an ultrasonic pulse-echo technique that consisted of placing three 5-MHz transducers on the inside surface of the vessel in line with the flaw location as shown in Fig. 4.9. The transducers were mounted in a special holder (Fig. 4.10) designed to maintain an on couplant between the transducer face and the vessel wall during vessel expansion and to prevent water from reaching the electrical connections when the vessel was pressurized.

The transducers were pulsed at a repetition rate of 2000 pulses/sec and individually monitored by ultrasonic flaw detectors. The output from the detectors was fed into video-tape recorders modified to record the ultrasonic signals. This system provided a recorded echo from the crack every 0.5 msec. The signals could later be examined on slow playback to evaluate the crack propagation.

A test of the transducers after installation revealed that the conductor to transducer B had been grounded out during the instrumentation of the vessel; transducers A and C were satisfactory. After the vessel was installed at the test site, the ultrasonic system was again checked and strong reflections were received from the bottom of the notch with transducers A and C. After the vessel was brought up to test temperature of 91°C (196°F), the response from transducer C was still normal, but the notch reflection to transducer A had disappeared. The signal from transducer A reappeared after the pressure reached 55 MPa (8000 psi). It is assumed that a small air bubble trapped in the couplant at the transducer face had expanded with an increase in temperature to prevent transmission of the signal and had compressed with pressure, or escaped the interface, to permit acoustic coupling again.

Prior to vessel pressurization, the ultrasonic instruments were calibrated for depth measurement with the bottom surface of the machined notch as the datum. This was necessary because the EB weld crack was not visible on the scope at zero pressure; therefore all the depth readings include the initial EB weld crack depth. The composite crack depth is shown in Fig. 4.11 as a function of pressure. The EB weld crack produced no indication until between 14 and 20 MPa (2000 and 3000 psi), at which time a perceptible indication appeared at a depth of 4 mm (0.16 in.). At 20 MPa (3000 psi), a positive indication of the crack was showing at 5 mm (0.20 in.) where it remained stationary in depth until after 34 MPa (5000 psi) pressure. Between 34 and 131 MPa (5000 and 19,000 psi), the crack depth increased with pressure at a relatively uniform rate during the pressurization periods. After 131 MPa, the crack depth increased more rapidly with each increase in pressure. After 138 MPa (20,000 psi), the crack indication continued to move for a short time after the pressure pumps were shut off, indicating an increase in depth with no increase in pressure.

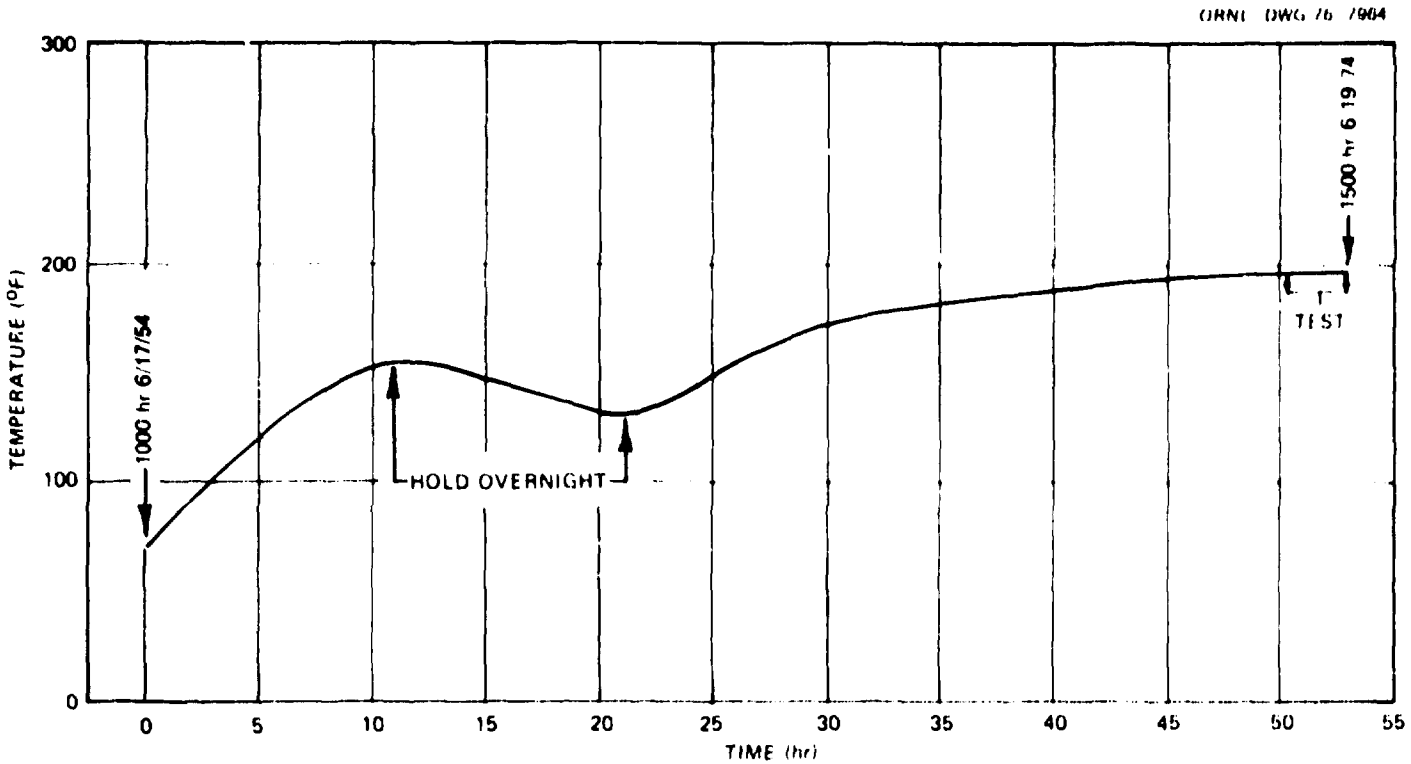

Fig. 4.7. Time vs temperature for location at thermocouple.

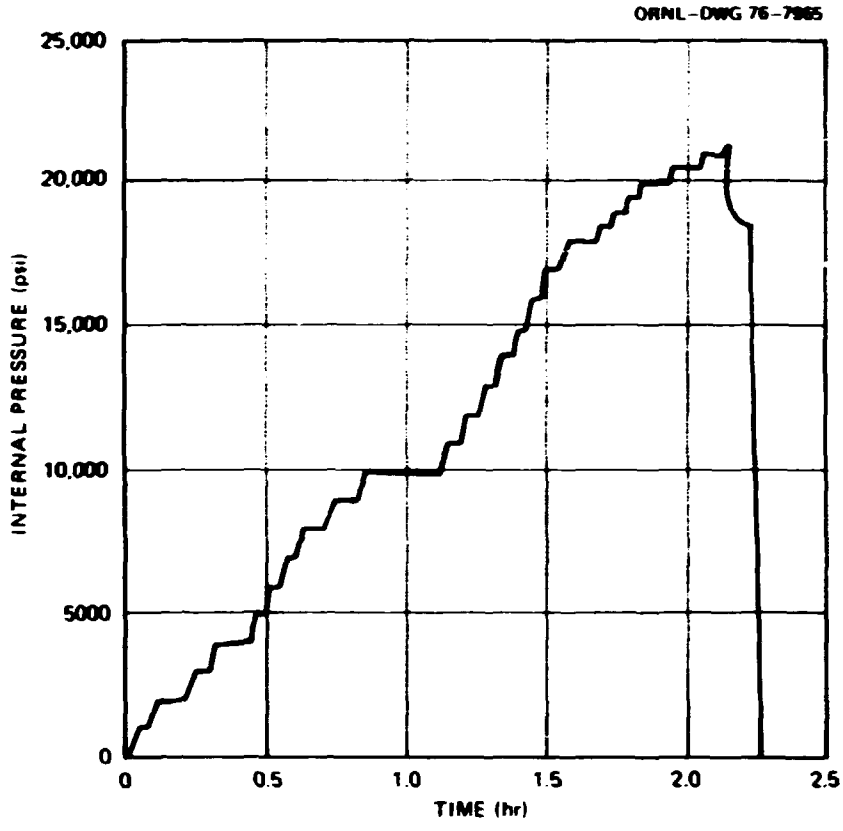

Fig. 4.8. Time vs pressure for test vessel V-7.

The signal from the inside surface of the vessel began moving toward the back surface signal (bottom of the notch) at approximately 131 MPa, indicating a reduction in thickness (Fig. 4.11). This reduction in thickness continued at an accelerated rate until vessel failure. At failure, the distance between the front surface signal and the crack signal was 1.3 mm (0.05 in.) at transducer C, which was located 76 mm (3 in.) from the center point of the notch.

TEST RESULTS

The final test results for test vessel V-7 are summarized in Table 4.1 along with a similar summary of the previously tested vessels.[1,2] The COD data from the three external displacement transducers are presented vs pressure in Fig. 4.12. Figure 4.13 shows circumferential strain at 180° from flaw vs pressure, and inside surface ligament strains are depicted in Figs. 4.14 and 4.15. The circumferential ligament strains as a family of curves at different pressures vs location and vs pressure are shown in Figs. 4.14 and 4.15 respectively.

A posttest view of vessel V-7 is given in Fig. 4.16, where the permanent crack opening is visible along the base of the machined notch. This opening is shown more clearly in Fig. 4.17. The crack was probed with a sharp thin instrument to determine the depth of the visibly open crack. The contour of the crack determined in this way is given in Fig. 4.18. The actual precracked depth was also verified approximately by visual examination of the flaw. The inside surface of the vessel beneath the notch is shown in Fig. 4.19.

ORNL-DWG 74-10467

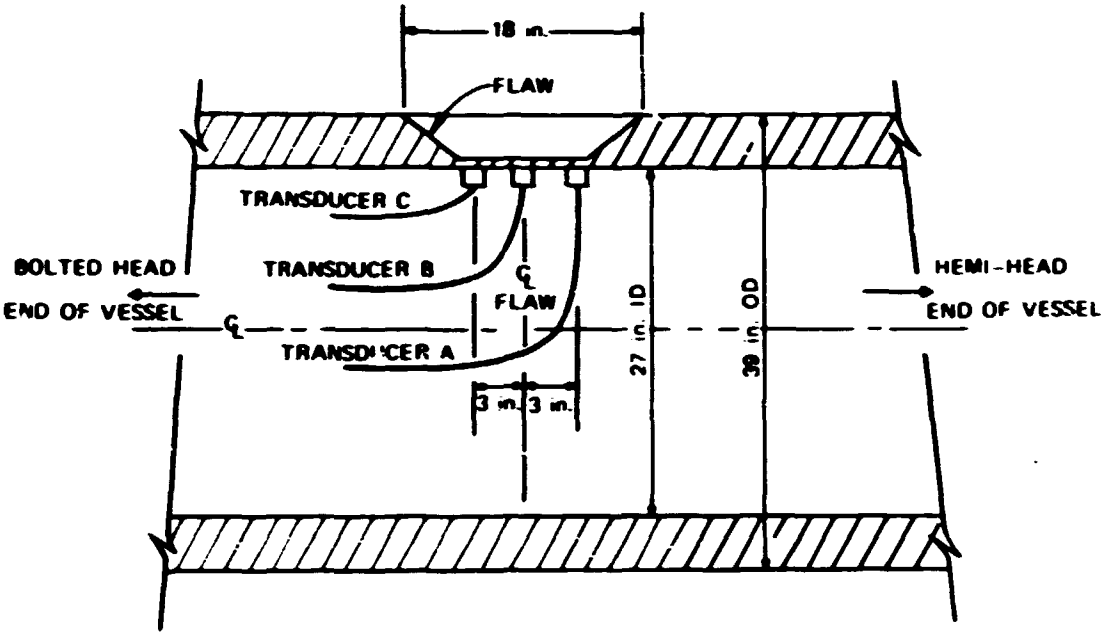

Fig. 4.9. Ultrasonic transducer placement in vessel V-7.

ORNL-DWG 76-7966

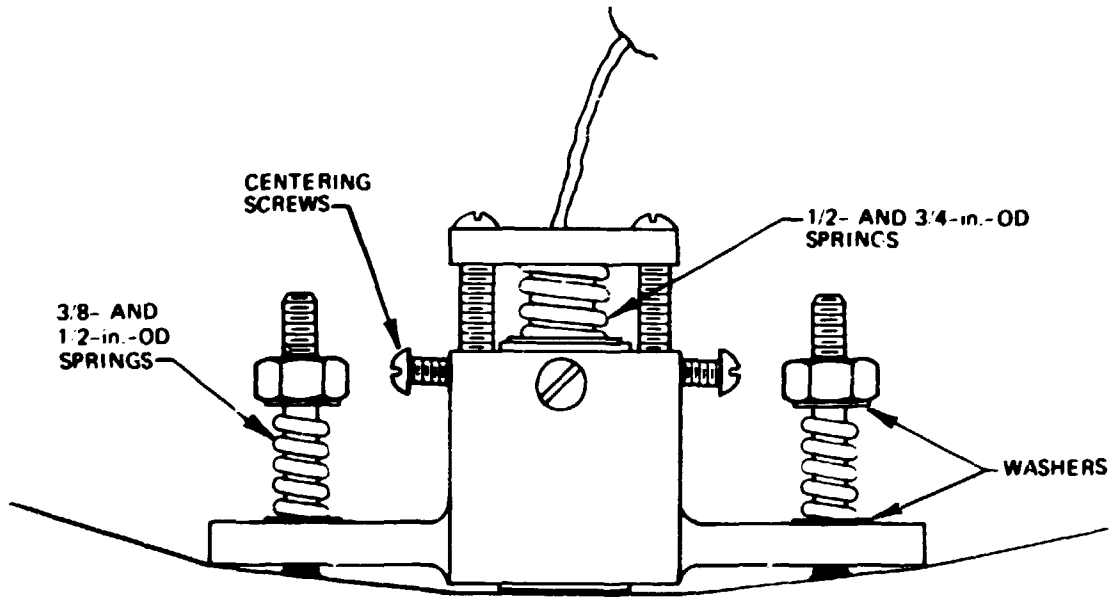

Fig. 4.10. Transducer holder for vessel V-7.

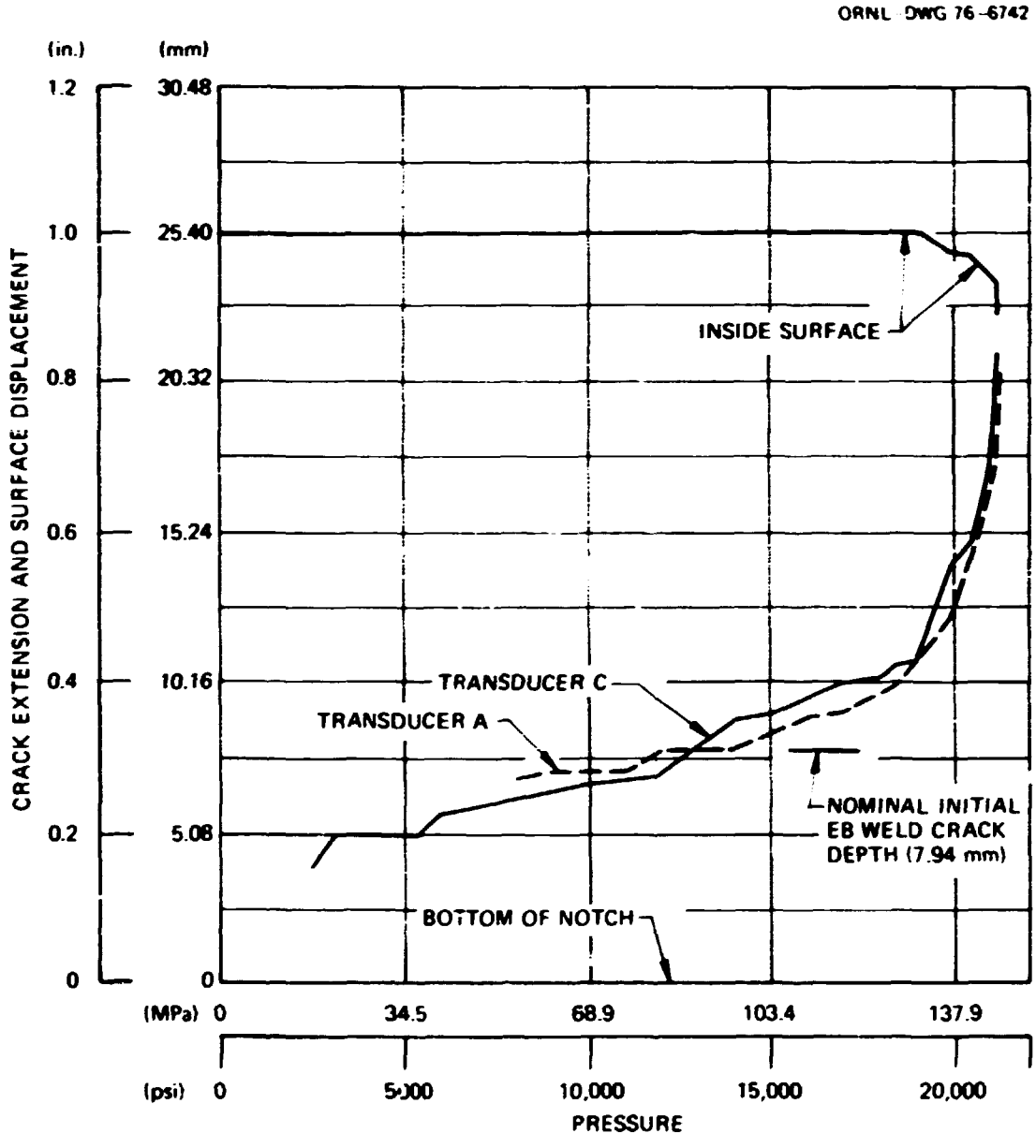

Fig. 4.11. Crack depth and inside surface deformation vs pressure measured ultrasonically in vessel V-7.

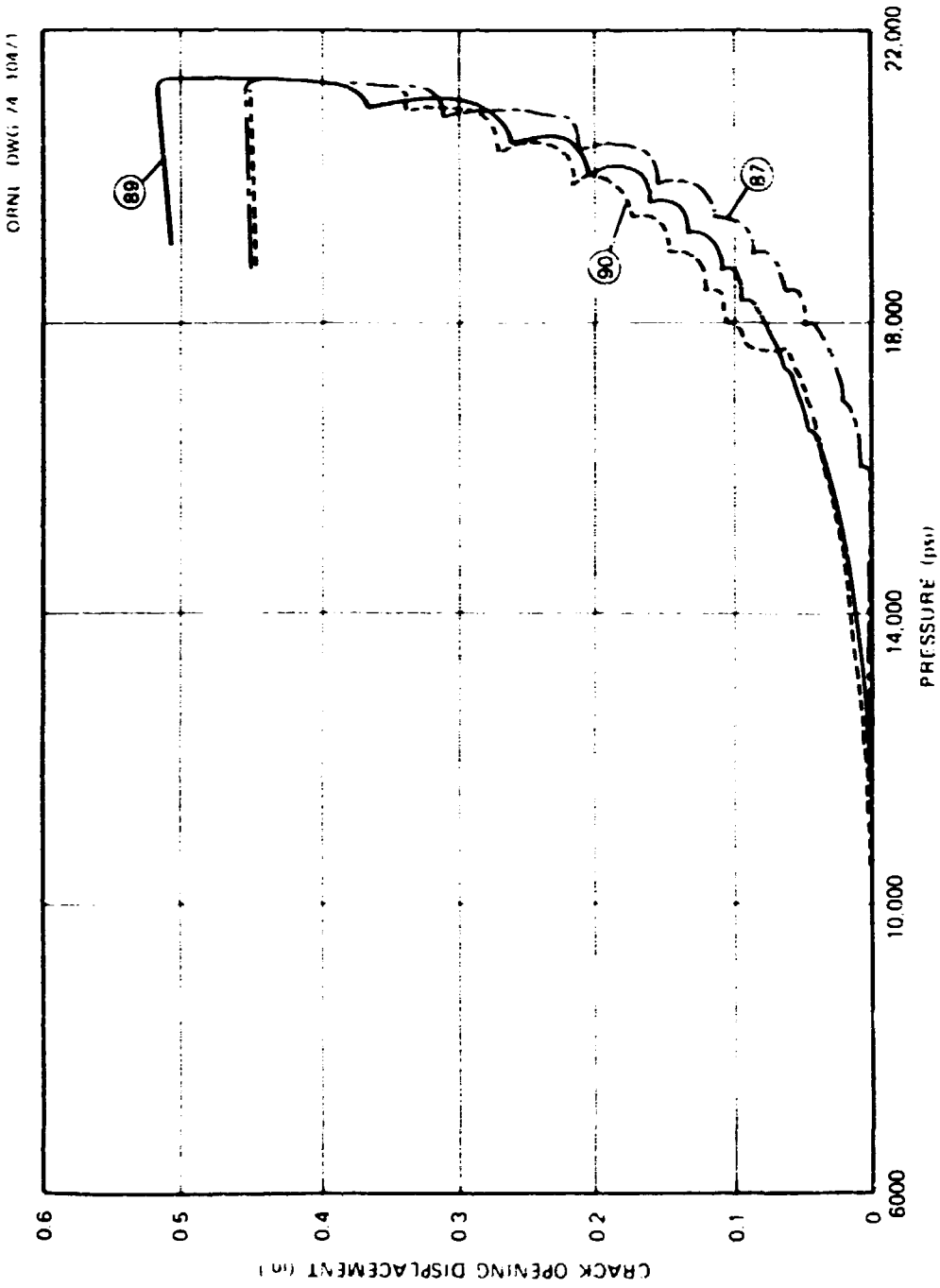

Fig. 4.12. Crack-opening displacement vs pressure for vessel V-7.

Table 4.1. Summary of test results from six 152-mm-thick (6-in.) intermediate test vessels

Vessel No.	Test temperature [°C (°F)]	Flaw dimensions (in.)		Flaw location[a]	Fracture pressure (ksi)	Nominal fracture strain[b] (%)
		Depth	Length			
V-1	54 (130)	2.56	8.25	Base metal (o)	28.8	0.92
V-2	0 (32)	2.53	8.30	Base metal (o)	27.9	0.19
V-3	54 (130)	2.11	8.50	Weld metal (o)	31.0	1.47
V-4[c]	24 (75)	2.95	8.25	Weld metal (o)[d]	26.5	0.17
	24 (75)	3.12	8.05	Base metal (o)	26.5	0.17
V-6[e]	88 (190)	1.87	5.25	Weld metal (o)[f]	33.9	2.0
	88 (190)	1.34	5.20	Base metal (o)	31.9	2.0
	88 (190)	1.94	5.30	Weld metal (i)	31.9	2.0
V-7	88 (190)	5.31	18.6	Base metal (o)	21.35	0.123

[a] Letter o = outside surface; i = inside surface.
[b] Outside circumferential strain on center line of vessel remote from flaw.
[c] Contained two flaws.
[d] Flaw where fracture occurred.
[e] Contained three flaws.

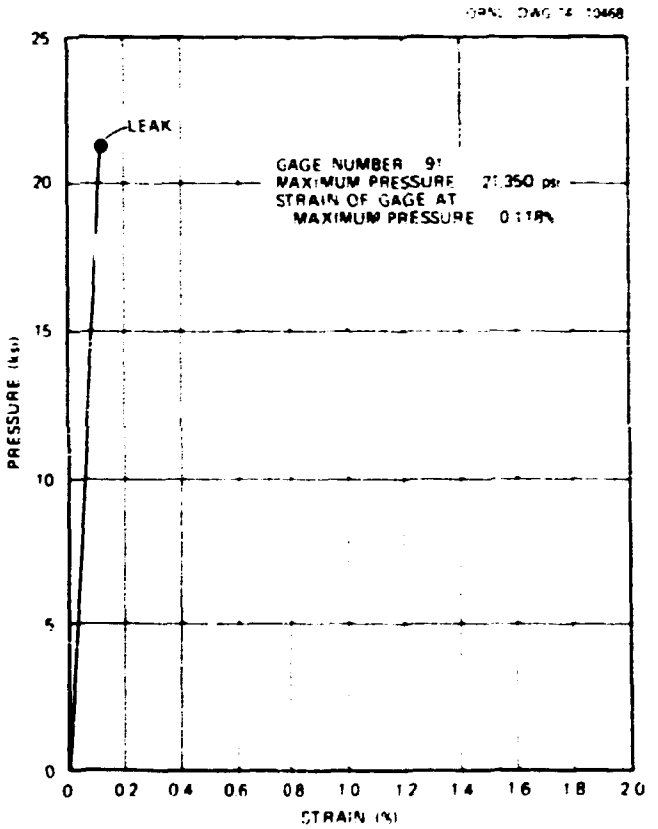

Fig. 4.13. Pressure vs outside surface circumferential strain 180° from flaw for test of vessel V-7.

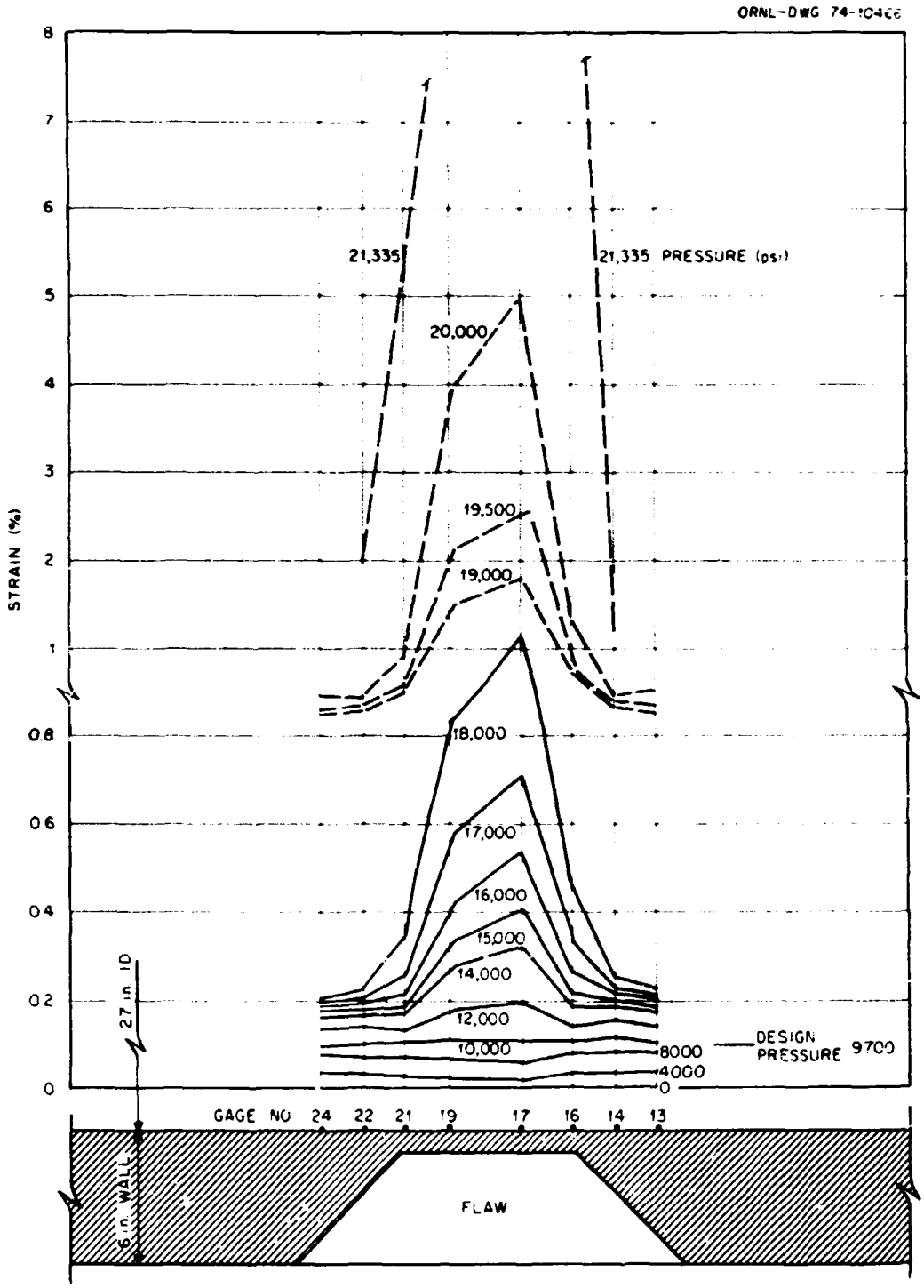

Fig. 4.14. Circumferential strain vs ligament location as a function of pressure. Test of intermediate vessel V-7.

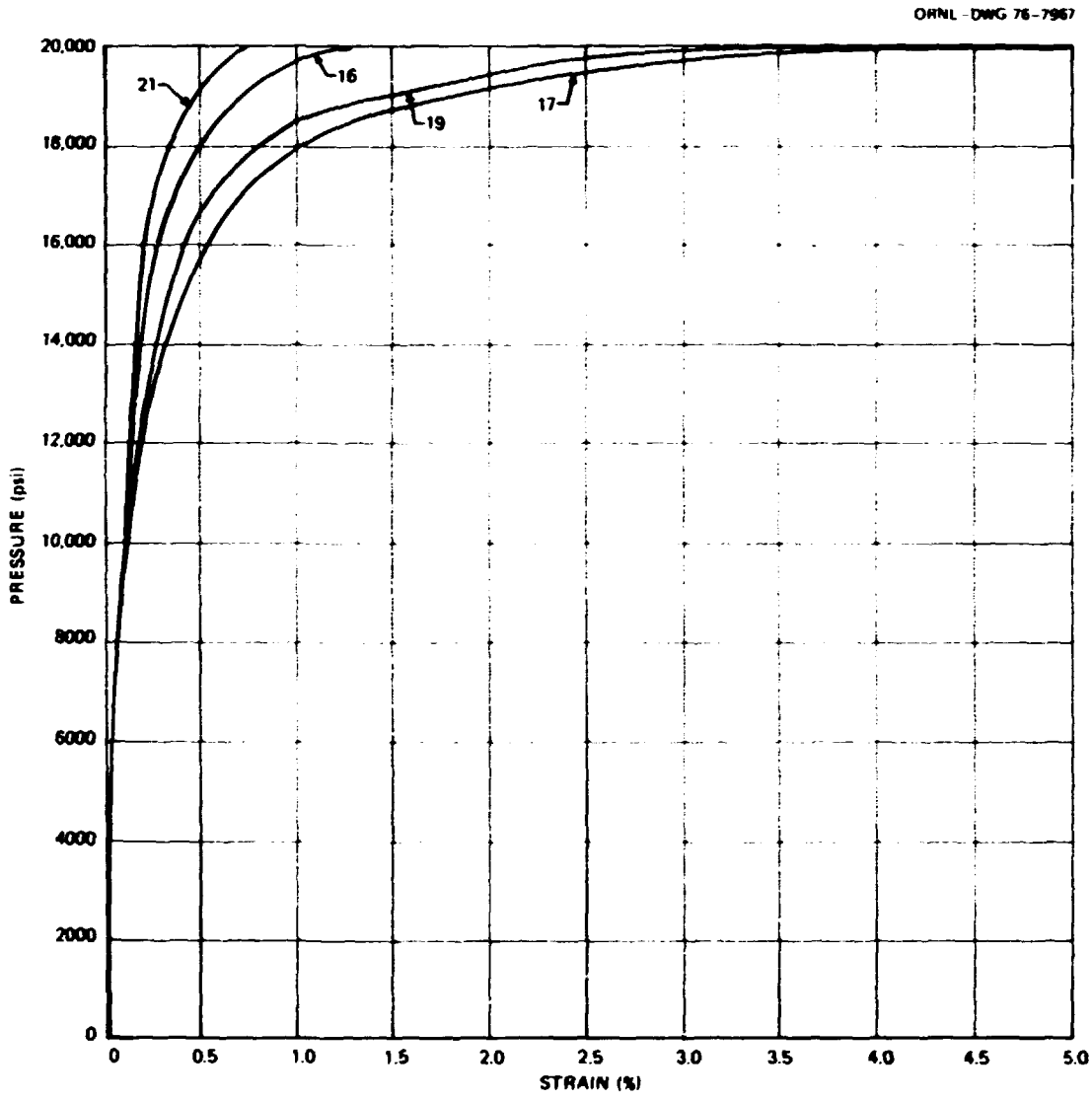

Fig. 4.15. Circumferential strain vs pressure as a function of ligament location. Test of intermediate vessel V-7.

Fig. 4.16. Intermediate vessel V-7 after testing.

Fig. 4.17. Permanent crack opening of vessel V-7 flaw after test.

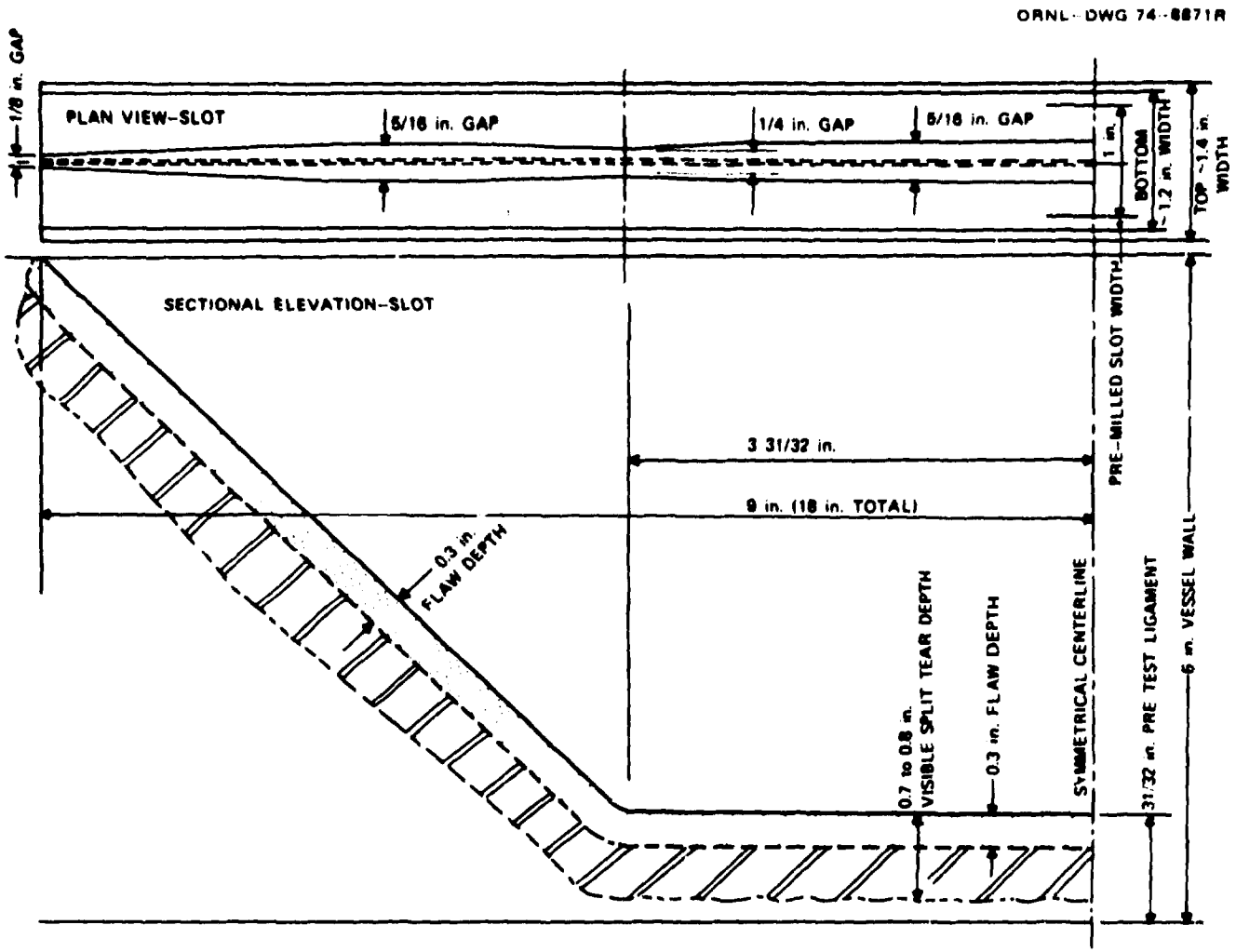

Fig. 4.18. Contour of visible crack in vessel V-7 after test.

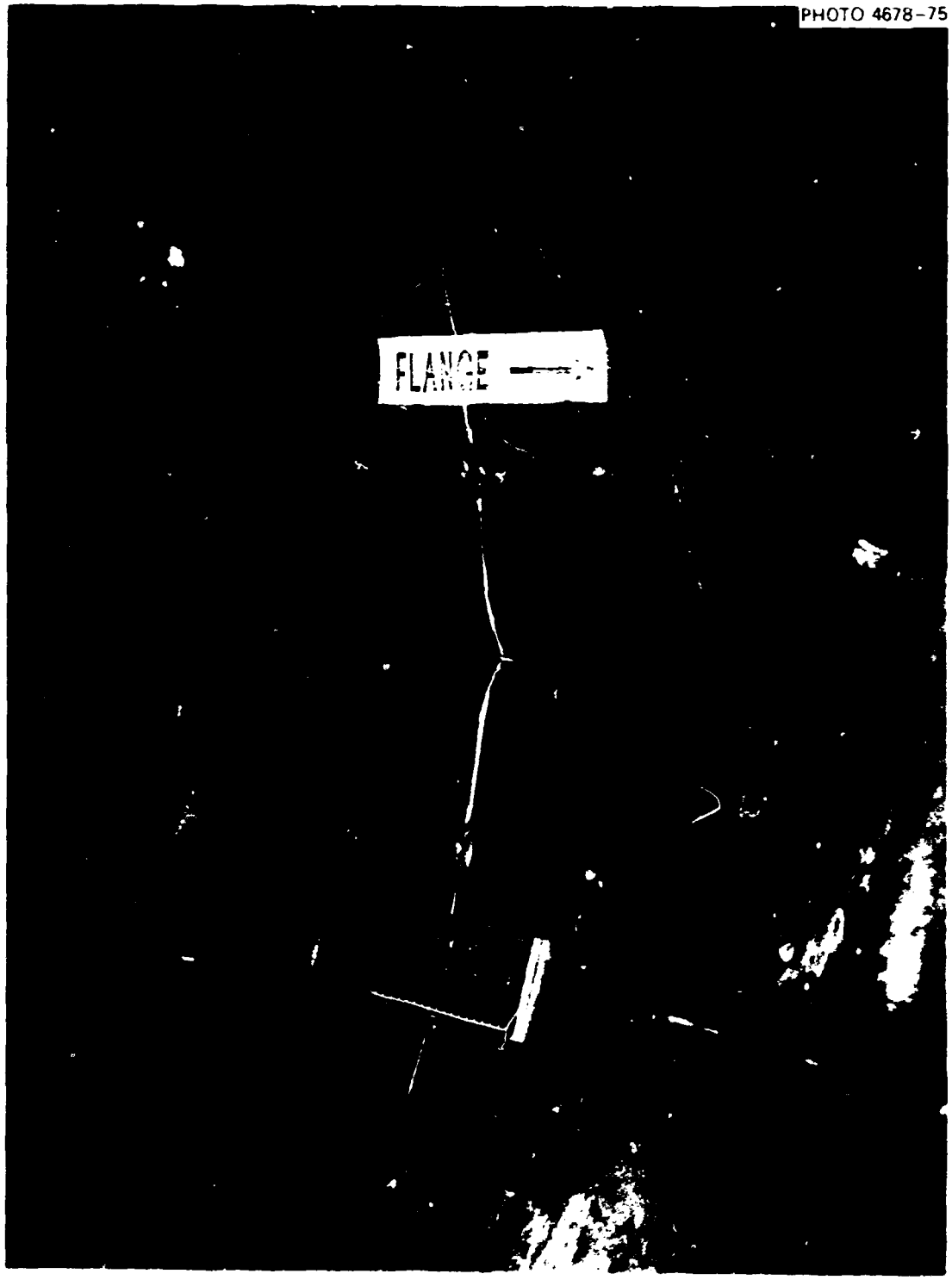

Fig. 4.19. Inside view of rupture zone of vessel V-7 after test. Chalk line marks circumferential center line of notch, and vestiges of studs are from the UT transducer holders.

The visible rupture extends for about 130 mm (5 in.) along the straight portion of the dimple on the inside surface.

REFERENCES

1. R. H. Bryan et al., *Test of 6-in.-thick Pressure Vessels. Series 2: Intermediate Test Vessels V-3, V-4, and V-6*, ORNL-5059 (November 1975).

2. R. W. Derby et al., *Test of 6-in.-thick Pressure Vessels. Series 1: Intermediate Test Vessels V-1 and V-2*, ORNL-4895 (February 1974).

5. Fracture Analysis Methods and Results

BACKGROUND

Early in the development of quantitative methods of fracture prevention for nuclear pressure vessels, consideration was given to the possibility of applying a "leak-before-break" criterion to these vessels, despite the fact that their wall thicknesses greatly exceed those of the high-yield-strength aerospace pressure vessels for which the criterion was originally developed. The leak-before-break criterion originally stated that a through crack of total length equal to double the vessel wall thickness should not propagate at a nominal stress equal to the yield stress. This criterion was later modified to include specified nominal stresses less than the yield stress.[1] For an axial through crack in a pressurized cylinder, a linear elastic fracture mechanics leak-before-break calculation involves consideration of (1) the plastic zone size, (2) bulging, (3) transverse restraint, and (4) loading rate.

Neglecting bulging effects, illustrative leak-before-break calculations based on dynamic plane stress conditions, including a plastic zone size correction and with an elevation of fracture toughness due to less than full transverse restraint, were made by Irwin.[1] These calculations indicated that a 305-mm-thick (12-in.) pressure vessel could satisfy the leak-before-break criterion at 93°C (200°F) at a stress level of 214 MPa (31 ksi) if the dynamic plane strain fracture toughness of the material was at least 205 MN·m$^{-3/2}$ (187 ksi $\sqrt{\text{in.}}$). The elevation of fracture toughness due to less than full transverse restraint was estimated by means of the empirical equation[1]

$$K_c^2 = K_{Ic}^2 \left(1 + 1.4\beta_{Ic}^2\right) , \tag{1}$$

where

$$\beta_{Ic} = \frac{1}{B}\left(\frac{K_{Ic}}{\sigma_Y}\right)^2 . \tag{2}$$

and B is the specimen thickness. Although fracture toughness values for nuclear pressure vessel steels had not been measured at 93°C (200°F), the resulting value of fracture toughness required to satisfy the above stated leak-before-break criterion was nevertheless considered achievable.[1]

Early reviews of the plans for the HSST program brought forth comments and questions concerning the effects of sustained loading in actual reactor pressure vessels (referred to as pneumatic loading), low upper-shelf toughness conditions, modes of failure involving reasonably large flaws partly through thick sections, energy requirements for crack initiation vs crack propagation, and the feasibility of determining the ability of thick-walled pressure vessels containing fatigue-grown flaws to meet a leak-before-break criterion at service temperatures under partially pneumatic loading.[2,3] Some experimental evidence concerning most of these factors was already available,[4] but it was not considered sufficient to support any firm conclusions.

In response to Refs. 2 and 3, leak-before-break calculations were made by Corten in the process of preparing a recommended test plan for the HSST program simulated service test vessels, and these calculations led to a negative conclusion.[5] The calculations were based on static plane strain, full-restraint conditions, including a plastic zone size correction; assumed a nominal applied stress equal to the yield stress of 414 MPa (60 ksi); and included the effects of bulging, which, however,

were not large. It was concluded that a plane strain fracture toughness of 454 MN·m$^{3/2}$ (414 ksi $\sqrt{\text{in.}}$) would be required to satisfy the leak-before-break criterion for a 305-mm-thick (12-in.) pressure vessel at a nominal applied stress equal to the yield stress. The existence of such a level of fracture toughness was considered, at the time, not to be a reasonable assumption for 305-mm-thick pressure vessels. Because of this conclusion, the test plan for the HSST program intermediate pressure vessels was originally based on the objective of experimentally defining what were expected to be the two most prominent modes of fracture behavior for thick-walled pressure vessels: frangible (below yield stress) fracture at low temperatures and tough (above yield stress) fracture at higher temperatures.[6] Original test plans therefore did not include a deliberate attempt to produce a leak without rupture.[7]

An important series of experiments that was carried out before and during the tests of the intermediate pressure vessels was the testing of over 40 smaller scale flawed steel models.[8] Failure by leakage without bursting occurred in several of the higher temperature hydraulically loaded models, and experimental data were also obtained on models tested at elevated temperature under pneumatic loading.[8,9] All of the elevated-temperature pneumatic loading tests resulted in burst failures, all but two of which occurred above the gross yield pressure of models that contained external surface flaws of depths less than half the wall thickness. Figure 5.1 shows hydraulically loaded model 6 undergoing failure by leakage at an internal pressure of 234 MPa (34 ksi) at 16°C (61°F). The model was 76.2 mm (3 in.) in diameter and 11.4 mm (0.45 in.) in wall thickness. Figure 5.2 shows three 7.62-cm-diam (3-in.) pneumatically loaded models after testing at temperatures near 260°C (500°F). The data for these models are listed in Table 5.1. The difference in failure mode between models 9 and 6, which had comparable initial flaw sizes, is clearly evident from Figs. 5.1 and 5.2. The decrease in residual crack opening after failure under pneumatic loading with increasing initial crack size is also clearly evident in Fig. 5.2. The initial flaw size in pneumatically loaded model 10 (Fig. 5.2), which burst at 152 MPa (22 ksi), is geometrically similar, based on wall thickness, to a flaw 508 mm (20 in.) long and 115 mm (4.53 in.) deep in an intermediate test vessel.

The intermediate vessel test series derived its name from the fact that it was originally intended to be a series of ultimate strength evaluation tests on vessels of a size intermediate between smaller scale models and larger scale safety margin demonstration tests. However, when the testing of vessels larger than the intermediate test vessels was determined to be unfeasible because of cost, the intermediate test vessels assumed the additional role of safety margin demonstration tests. For this reason, Kooistra[10] suggested that the plan for testing the intermediate vessels be enlarged to include

Table 5.1. Summary of 260°C (500°F) pneumatic burst tests conducted on 762-mm-diam (3-in.) flawed model pressure vessels of A533, grade B, class 1 steel[a]

Vessel No.	Burst pressure [MPa (ksi)]	Flaw depth [mm (in.)]	Flaw length [mm (in.)]
9	218 (31.6)	4.32 (0.17)	19.1 (0.75)
8	181 (26.3)	6.10 (0.24)	26.7 (1.05)
10	152 (22.0)	8.64 (0.34)	38.1 (1.5)

[a]Tests conducted at ORNL by R. W. Derby, Sept. 2, 1971.

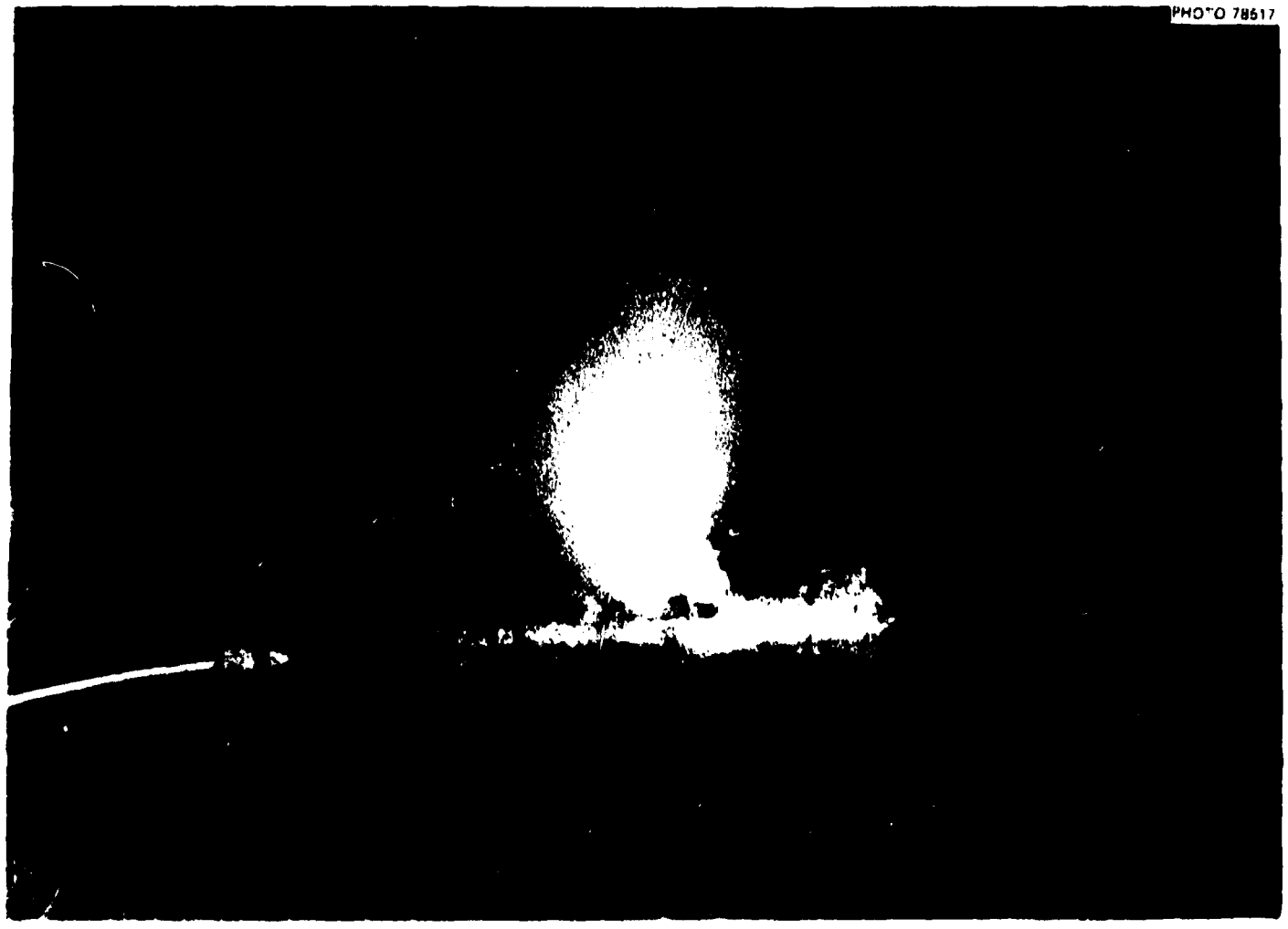

Fig. 5.1. Hydraulically loaded model 6 (A533 grade B, class 1 steel) undergoing failure by leakage through test flaw at 16°C (61°F). Model was 76.2 mm (3 in.) in diameter and 11.4 mm (0.45 in.) in wall thickness.

PHOTO 78988

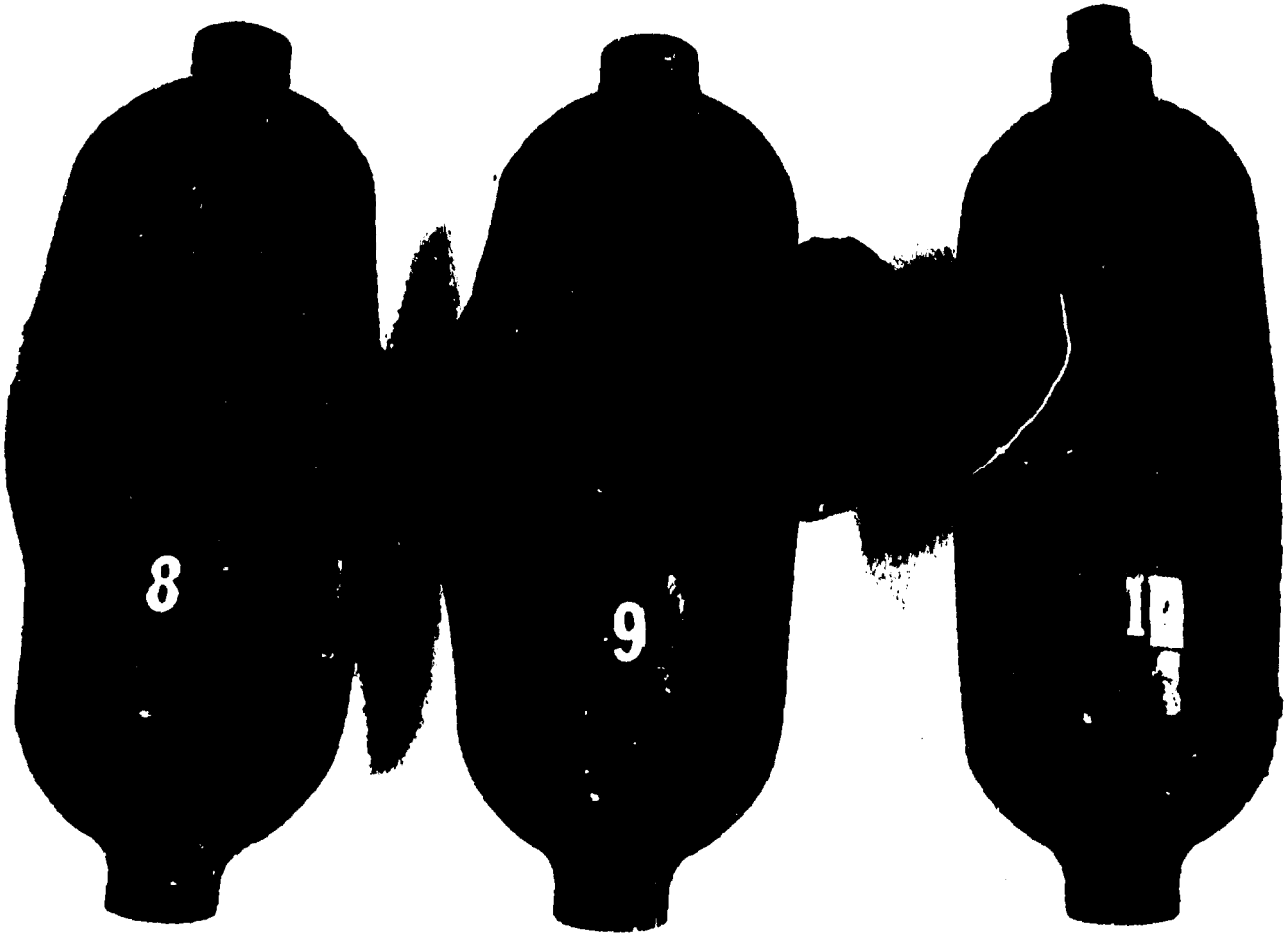

Fig. 5.2. Posttest photograph of three flawed 76.2 mm-diam (3-in.) steel models tested pneumatically at about 260 C (509 F). Model 9 contained the smallest flaw; model 10 contained the largest flaw.

a demonstration of the flaw size required to cause failure at a specified pressure, perhaps 1½ times code design pressure. An estimate of the flaw size required to cause failure of an intermediate test vessel at design pressure and temperature was then made by Derby,[11] based on the pneumatic test data listed in Table 5.1. Derby estimated that a flaw 483 mm (19 in.) long and 124 mm (4.9 in.) deep would be required to cause failure of an intermediate test vessel at its code design pressure at elevated temperature.[11] The matter of flaw size was raised again by Prof. H. T. Corten at the Oct. 25-26, 1972, meeting of the HSST Program Planning Committee, one month after the test of intermediate test vessel V-2. Following the test of intermediate test vessel V-3 on Nov. 8, 1972, definite planning began for the testing of an intermediate test vessel with a flaw size large enough to cause failure at near design conditions.[12] The flaw dimensions proposed at this time were a depth of 102 mm (4 in.) and a surface length of 457 mm (18 in.).

MODEL TESTS FOR FLAW SIZE SELECTION

Although the pneumatically tested models (Table 5.1) provided valuable information with respect to the tentative selection of a flaw size for intermediate test vessel V-7, they were not considered to be an adequate basis for final flaw size selection for several reasons:

1. they were constructed of plate material having a different variation of fracture toughness with temperature and possibly with specimen size in the upper-shelf temperature range than the intermediate test vessel cylinder materials;
2. they were of smaller diameter and wall thickness than the 140-mm-diam (5½-in.) models being used as companion models for the other intermediate test vessels;
3. they contained rectangular surface flaws, a configuration that was not desired for use in the intermediate test vessels;
4. they were not instrumented with strain gages because of their high testing temperatures.

Consequently, three 140-mm-diam (5½-in.), 21.6-mm (0.85-in.) wall thickness models containing relatively large trapezoidal flaws of three different sizes were tested hydraulically at 88°C (190°F) to provide a better basis for the final selection of the flaw dimensions in intermediate test vessel V-7. One of these models (model V4.3) was fabricated from vessel V-4 prolongation material, and the other two (models V7E-A2 and V7E-A3) were fabricated from vessel V-7 prolongation material.[8] The test data for these three models are summarized in Table 5.2. As indicated in the table, the flaws in models V4.3, V7E-A3, and V7E-A2 were trapezoidal rather than rectangular or part-circular. The trapezoidal shape was selected in order to provide a remaining ligament of uniform thickness and because plans were to machine the notch in vessel V-7 on a horizontal boring mill, on which it would have been difficult to machine a continuously curving notch contour. The trapezoidal shape was also chosen in preference to a rectangular shape in order to reduce the chances of initial crack extension occurring at the ends of the remaining ligament rather than near its midpoint, and because this shape was considered to approximate the shape of flaws that grow naturally by fatigue better than a rectangle.

The initial objective of the model tests summarized in Table 5.2 was to determine the surface length of the flaw to be used in vessel V-7, assuming that the flaw depth would be between 102 mm (4 in.) and 127 mm (5 in.). However, the analyses of the data, to be discussed later, indicated that the thickness of the remaining ligament, which is directly related to the crack depth, is actually the flaw dimension that controls the failure pressure most directly.

Table 5.2. Data from the three 140-mm-diam ($5\frac{1}{2}$-in.) steel models[a] tested hydraulically at 88 C (190 F)

Model No.	Date tested	Prolongation material	Trapezoidal flaw dimensions (mm (in.))			Failure conditions		Mode of failure
			Depth	Surface length	Ligament length	Pressure (MPa (ksi))	Strain	
V4.3	10 16 73	V-4	15.2 (0.60)	42.2 (1.66)	25.9 (1.02)	194 (28.2)	0.42	Burst
V7E-A3	11 9 73	V-7	18.0 (0.71)	64.8 (2.55)	47.0 (1.85)	165 (23.9)	0.12	Leak
V7E-A2	12 18 73	V-7	18.0 (0.71)	43.2 (1.70)	25.4 (1.00)	190 (27.5)	0.193	Leak

[a]Data from these models provided the basis for the final design of the flaw in vessel V-7.

At the beginning of the preparations for the test of vessel V-7, neither the exact flaw size nor a reliable method for sharpening the flaw in the test vessel were known. The model testing discussed here that provided a firm basis for selecting a flaw size and the experiments discussed in Chapter 3 that led to the development of a reliable method for sharpening the flaw in vessel V-7 were carried out concurrently. The final flaw design for vessel V-7 was based on the results of both investigations.

During the investigations of flaw-sharpening techniques, it was determined that a flaw of the approximate size and shape desired for vessel V-7 could not be sharpened by fatigue using cyclic notch pressurization because of notch sealing difficulties, flaw shape, and limitations on cyclic pumping volume. This led to the brief consideration of using a small machined notch root radius in vessel V-7, but this approach was abandoned because existing specimen test data showed that natural cracks and sharply machined notches may differ with respect to the load at the onset, and the eventual extent of, stable crack extension. Consequently, attention was directed toward the use of electron-beam (EB) welding and hydrogen charging as a crack-sharpening procedure; after an extensive development effort, this approach proved to be successful, as discussed in Chapter 3.

ANALYSES OF HYDRAULIC MODEL TEST DATA

Plastic Instability Analyses of Models V4.3 and V7E-A3

The three models listed in Table 5.2 were analyzed separately as they were tested, and then additional analyses were performed after the third model was tested. The first calculation was made immediately following the test of model V4.3, which had the smallest flaw of the three models tested. A photograph of the crack region of model V4.3 after testing is shown in Fig. 5.3. The calculation was a conventional local plastic instability analysis of the type described in Appendix C of Ref. 13, and, ignoring stable crack growth, resulted in a calculated pressure of 189 MPa (27.4 ksi), which was only 3% less than the actual failure pressure. However, the accuracy of this calculation was later found to be fortuitous, since by oversight it was based on the machined notch depth of 12.4 mm (0.49 in.), ignoring the additional depth of the electron-beam weld, and assumed the crack to be semielliptical instead of trapezoidal.

Model V7E-A3, which contained the largest flaw of the three models, was tested next. The flaw in this model was geometrically similar to a trapezoidal flaw in an intermediate test vessel with a depth of 12.7 mm (5 in.), a surface length of 45.7 mm (18 in.), and a ligament length of 33.0 mm (13 in.). A posttest photograph of the crack region of model V7E-A3 is shown in Fig. 5.4. A pretest local plastic instability analysis of the model, based conservatively on a rectangular rather than a trapezoidal effective load-bearing

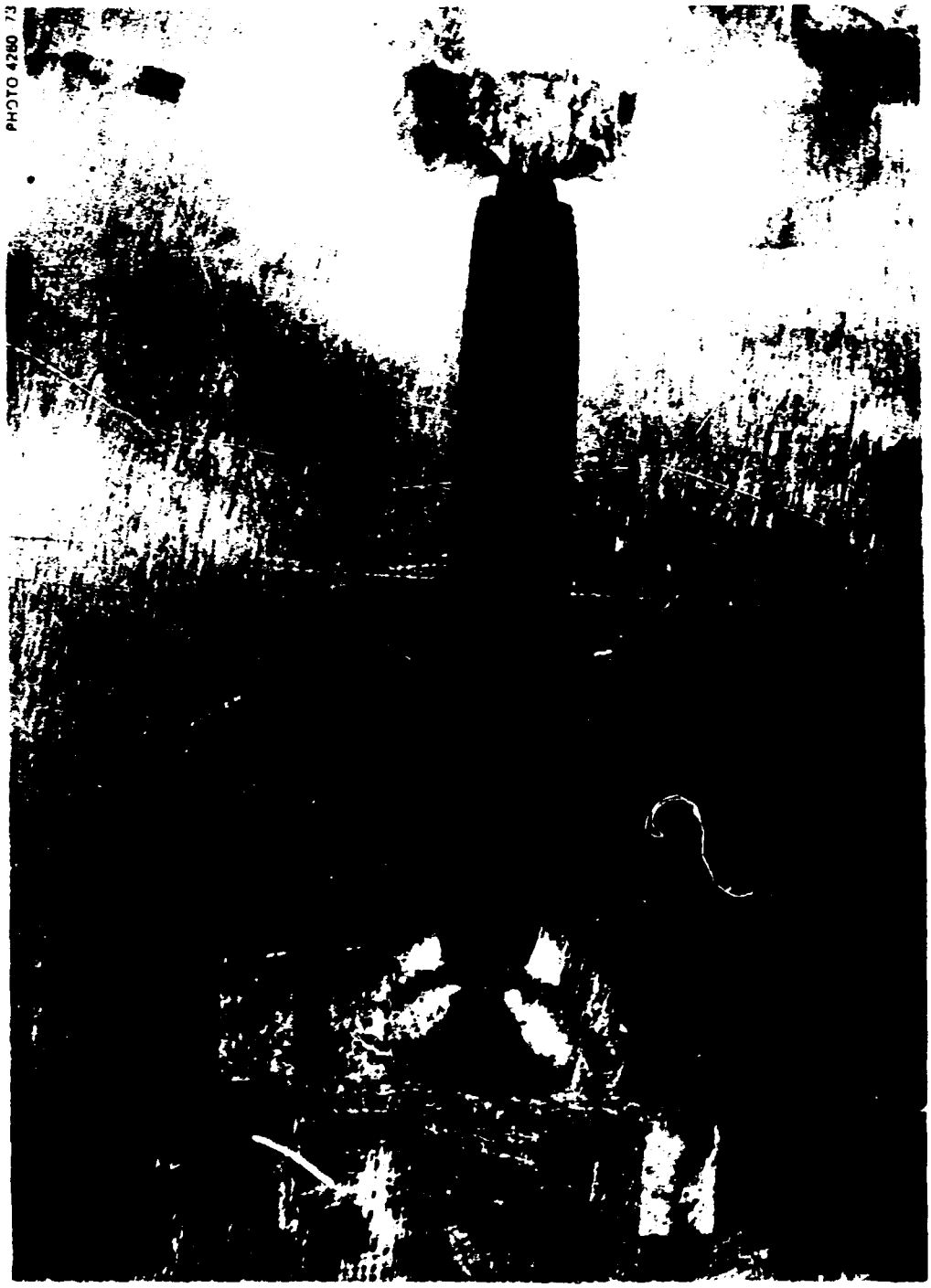

Fig. 5.3. Posttest photograph showing flaw region of model V-3.

Fig. 5.4. Posttest photograph showing flow region of model V7E-A3.

area, resulted in a calculated pressure of 75.2 MPa (10.9 ksi), which was considerably less than the actual failure pressure of 165 MPa (23.9 ksi). A posttest local plastic instability analysis of model V7E-A3, based on the conventional assumption of a trapezoidal effective load-bearing area,[13] resulted in a calculated pressure of 134 MPa (19.5 ksi), which was still 23% less than the actual failure pressure. Thus it was apparent that, for this model, the development of plastic instability in the region surrounding the flaw had not caused immediate crack extension, and therefore that the onset of crack extension would have to be analyzed in terms of a calculation based on fracture toughness.

The third model tested, model V7E-A2, had a flaw depth equal to that in model V7E-A3 but a flaw surface length only slightly greater than the flaw in model V4.3. Model V7E-A2 was not analyzed before testing, but it was expected to and did fail at a pressure between the failure pressures of the other two models. A posttest photograph of the crack region of model V7E-A2 is shown in Fig. 5.5. The failure points of all three models are shown plotted in Fig. 5.6, along with a calculated pressure-strain curve for the intermediate test vessels. It can be seen from the figure that with flaw size being the only important variable, failures were produced above, at, and below the gross yield pressure of the models.

Following the testing of the three models, it was clear that a plastic instability analysis alone would not be a sufficient basis for the design of the flaw in vessel V-7 and that a calculation based on fracture toughness would also be required. At this point it was decided to state that in selecting or developing a method for designing the flaw in vessel V-7, the governing criterion would be that the method of analysis chosen should agree with the results of the three models tested. Thus the next step in the analytical investigation was to find a method of analysis based on fracture mechanics that agreed reasonably well with the results of the three models tested, especially with those from model V7E-A3, which failed below its gross yield pressure.

Elastic Shape Factor Calculations for Model V7E-A3

In anticipation of calculations based directly or indirectly on linear elastic fracture mechanics (LEFM), shape factors were estimated for the trapezoidal flaw in model V7E-A3 by several different methods in order to select the most appropriate method for estimating these factors. For these calculations, the flaw was represented as either a semielliptical or a part-circular surface crack having the same depth and area as the actual trapezoidal crack, as recommended by Harms and Smith[14] and by Kiefner et al.[15] The flaw in model V7E-A3 is shown in Fig. 5.7*a*. Denoting the ligament distance of the trapezoidal crack as w and the surface length of the trapezoidal crack as $2b$, the surface length of the equivalent semielliptical crack $2b_e$ is given by

$$\frac{2b_e}{2b} = \frac{1 + (w/2b)}{\pi/2} \tag{3}$$

The equivalent semiellipse for the flaw in model V7E-A3, for which $2b_e = 711$ mm (2.80 in.), is shown in Fig. 5.7*b*.

The equivalent part-circular surface crack is determined by the equation

$$\frac{\theta - \sin\theta\cos\theta}{(1 - \cos\theta)^2} = \left(\frac{b}{a}\right) + \frac{1}{2}\left(\frac{w}{a}\right), \tag{4}$$

where θ is defined in Fig. 5.7*c*. The other dimensions related to the equivalent part-circular surface crack

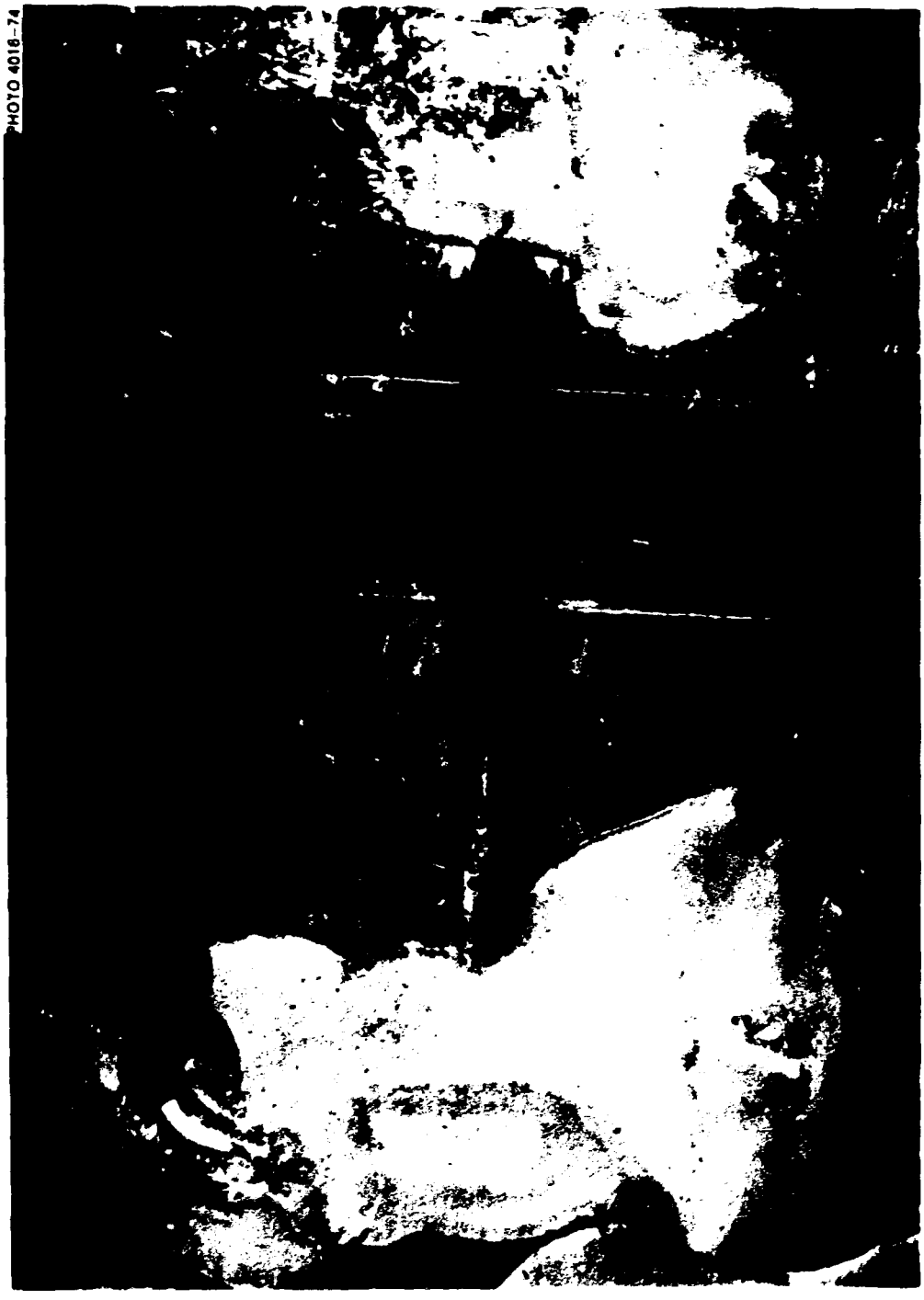

Fig. 5.3 Postiest photograph showing flaw region of model V7E-A2.

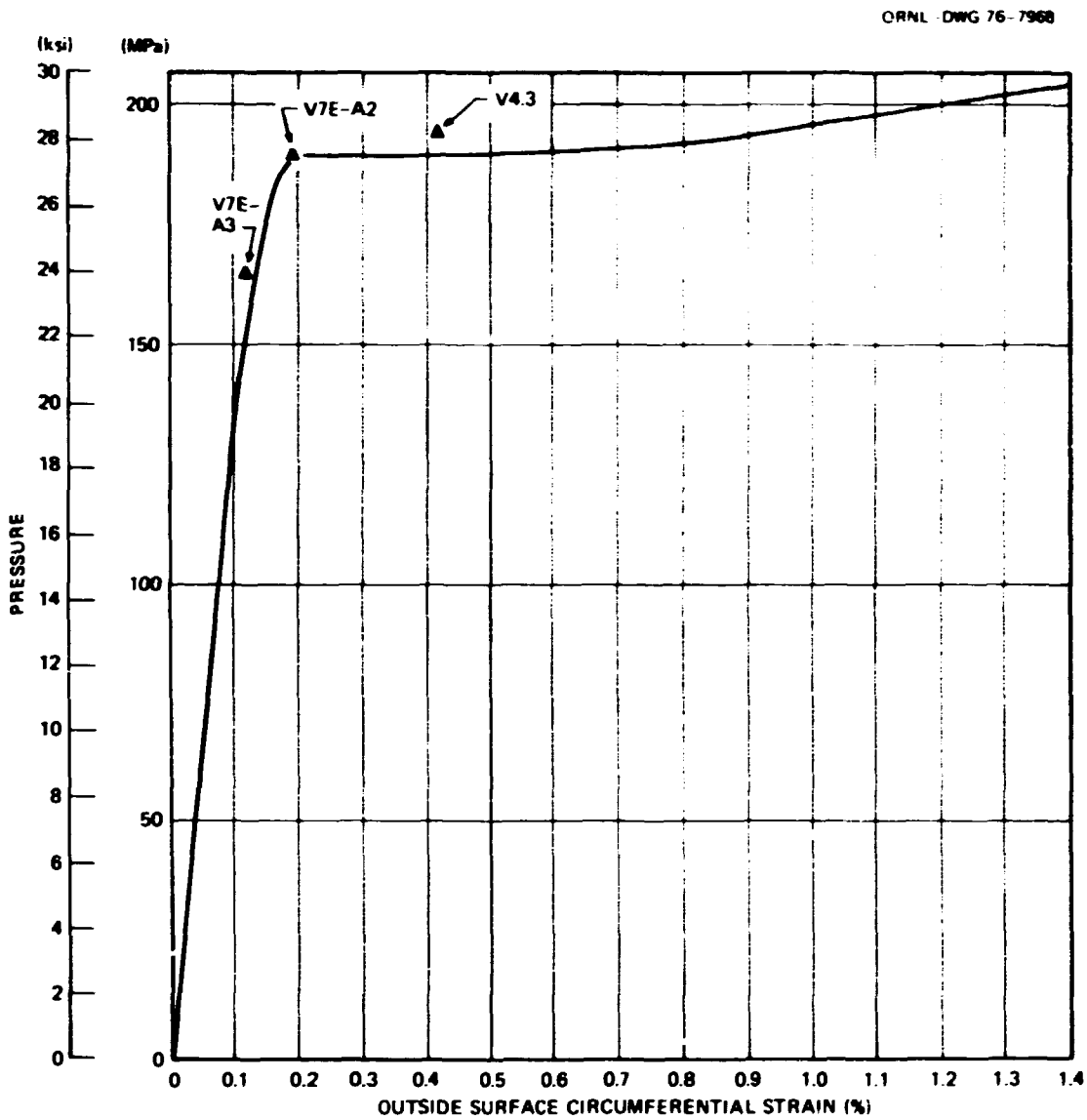

Fig. 5.6. Calculated pressure-strain curve and measured failure conditions for models V4.3, V7E-A2, and V7E-A3.

are determined by[16,17]

$$r_t = \frac{a}{1 - \cos\theta} , \tag{5}$$

$$b_c = r_t \sin\theta , \tag{6}$$

and

$$d = r_t \cos\theta . \tag{7}$$

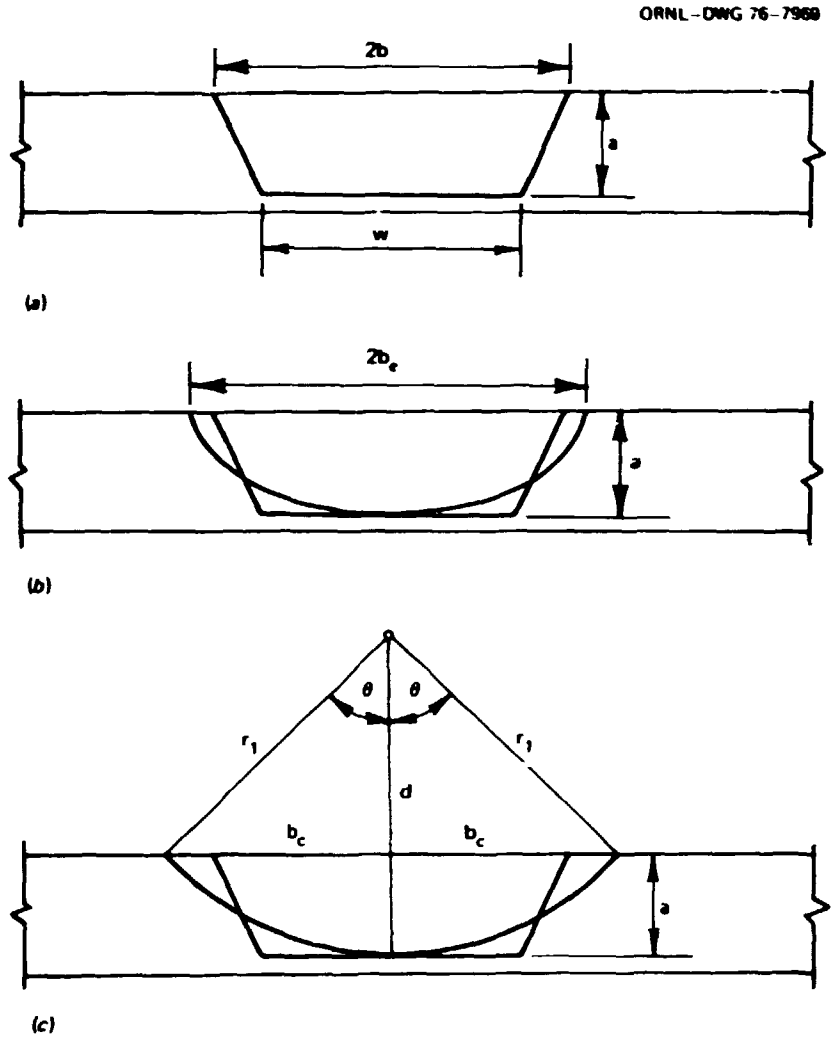

Fig. 5.7. Actual trapezoidal, equivalent semielliptical and equivalent part-circular crack configurations for model V7E-A3.

The equivalent part-circular surface crack for model V7E-A3, for which $2b_c$ = 831 mm (3.27 in.), is shown in Fig. 5.7*c*.

The shape factor at the deepest point of the equivalent part-circular surface crack, assuming uniform tensile loading, is given by[16,17]

$$C = \frac{\psi_0(0)}{(\pi/2)\sqrt{1-D}} M_2 \ , \tag{8}$$

where

$$D = \cos\theta = \frac{1 - (a/b_c)^2}{1 + (a/b_c)^2} \tag{9}$$

and M_2 is the back face free surface magnification factor. For the equivalent part-circular surface crack in model V7E-A3, $D = 0.682$, and from either Ref. 16 or 17, $\psi_0(0) = 0.79$ and $M_2 = 1.185$. Substituting these values into Eq. (8) gives $C = 1.06$.

Shape factor estimates for the equivalent semielliptical crack in model V7E-A3, assuming uniform tensile loading, were made by three different methods. The first estimate was made by a semiempirical equation developed by Newman,[18] which, for a specimen of effectively infinite width, is

$$C = \frac{M_1}{\sqrt{Q}} + \left(\sqrt{\frac{b_e}{a}} - \frac{M_1}{\sqrt{Q}}\right)\left(\frac{a}{t}\right)^z , \tag{10}$$

where

$$M_1 = 1.13 - 0.1\left(\frac{a}{b_e}\right) , \tag{11}$$

$$Q = 1 + 1.47\left(\frac{a}{b_e}\right)^{1.64} , \tag{12}$$

and

$$z = 2 + 8\left(\frac{a}{b_e}\right)^3 . \tag{13}$$

(Note that in this chapter, thickness is denoted by either t or B to be consistent with the original nomenclature of the method of analysis being applied.) For $a/b_e = 0.506$ and $a/t = 0.835$, Eqs. (10) through (13) give $C = 1.19$.

The second shape factor estimate for the equivalent semielliptical surface crack in model V7E-A3 was made by a semiempirical method developed at ORNL.[19] For the deepest point of a semielliptical surface crack under uniform tensile loading, the shape factor is given by

$$C = \frac{\psi_0(0) M_2(0)}{\Phi} , \tag{14}$$

where $\psi_0(0) = 1.025$ and

$$M_2(0) = \left[\frac{\tan(\pi a/2t)}{\pi a/2t}\right]^{1/2} . \tag{15}$$

Using the values of a/b_e and a/t for model V7E-A3 given previously and noting that, neglecting yielding, Φ and $\sqrt{Q}$ are identical, the value of Φ was determined from Eq. (12). Consequently, Eq. (14) gives $C = 1.44$.

The third shape factor estimate for the equivalent semielliptical surface crack in model V7E-A3 was made by the method described in Appendix A to Section XI of the ASME code for nuclear pressure vessels.[20] For uniform tensile loading, the value of the shape factor is determined from the values given graphically in Appendix A of Ref. 20 by

$$C = \frac{M_m}{\sqrt{Q}} . \tag{16}$$

For $a/2b_e = 0.253$ and $a/t = 0.835$, Fig. A-3300-3 of Appendix A gives $M_m = 1.712$ for small values of σ/σ_Y. Fig. A-3300-1 of Appendix A gives $Q = 1.48$. Substituting these values into Eq. (16) gives $C = 1.40$. Thus the four shape factor estimates for the flaw in model V7E-A3 were 1.06, 1.19, 1.44, and 1.40. Considering the spread in these values and the fact that two of the three models tested failed at or after the onset of gross yielding, it was apparent that the choice of a method for estimating shape factors for deep part-through surface cracks would have to be made in conjunction with the choice of an overall method of analysis based on the criterion of satisfactory agreement with the model experimental data.

Equivalent-Energy and LEFM Strain-Based Calculations for Model V7E-A3

The first fracture mechanics calculation made for model V7E-A3 was an equivalent-energy calculation based on a fracture toughness value of $K_{Ic(0.85)} = 312$ MN·m$^{-3/2}$ (284 ksi$\sqrt{\text{in.}}$), which is the average of the six toughness values measured by Westinghouse for the intermediate test vessel V-7 prolongation material.[21] (The same fracture toughness data are listed in Ref. 22, but there is a discrepancy between the values of fracture toughness for specimen V7D-6 as listed in Refs. 21 and 22.) Using the value of $C = 1.19$ obtained by Newman's method, the pseudoelastic failure pressure for model V7E-A3 was estimated from the equation[23]

$$p_f^* = \frac{K_{Ic}d}{C\left(\frac{r}{t}\right)\sqrt{\pi a}} , \tag{17}$$

which, for $d = 0.85$, gives $p_f = 490$ MPa (71.1 ksi). The corresponding estimate of failure strain for an LEFM analysis based on strain[23] is given by

$$\lambda_f = \frac{p_f^*}{M_p} . \tag{18}$$

where $M_p = 1321$ MPa·%$^{-1}$ (191.5 ksi·%$^{-1}$) for the intermediate test vessels. The resulting estimate of failure strain is 0.37%. The above values are extremely high with respect to the actual failure pressure of 165 MPa (23.9 ksi) and failure strain of 0.12% and clearly could not be corrected simply by using one of the higher shape factor values estimated previously. Thus it was apparent that the yielding of the remaining ligament plays a dominant role in the process of crack extension for deep cracks and that a satisfactory method of analysis for such cracks would have to take this phenomenon into account.

Crack-Opening-Displacement Calculations for Model V7E-A3

Two versions of a method of analysis based on the crack-opening-displacement (COD) concept that were developed specifically for the purpose of considering the yielding of the net ligament ahead of a deep part-through surface crack were used next for the analysis of model V7E-A3. The first version of the COD analysis was developed by Irwin and Corten[24] and the second by Irwin.[25] Referring to Fig. 5.8, in the Irwin-Corten analysis,[24] the actual part-through surface crack is analyzed as a through crack of the same total length as the actual crack, but with a uniform tensile stress applied to the through-crack surfaces of such magnitude that the total tensile force tending to close the crack is the same as the tensile force carried by the fully yielded ligament ahead of the part-through crack. The through crack is increased in length by a plane stress plastic zone size correction, and the COD at the center line of the crack is used as the failure criterion. The working equation of this method of analysis is

$$\delta_c = \frac{4b(\sigma'/\sigma_Y)}{1 - \frac{1}{2}(\sigma'/\sigma_Y)^2} , \tag{19}$$

where

$$\sigma' = \sigma - (t_N/B)\sigma_Y , \tag{20}$$

and

$$\delta_c = \frac{K_c^2}{E\sigma_Y} . \tag{21}$$

Combining Eqs. (19) and (21) results in the quadratic equation

$$\left(\frac{\sigma'}{\sigma_Y}\right)^2 + \frac{8b}{(K_c/\sigma_Y)^2}\left(\frac{\sigma}{\sigma_Y}\right) - 2 = 0 . \tag{22}$$

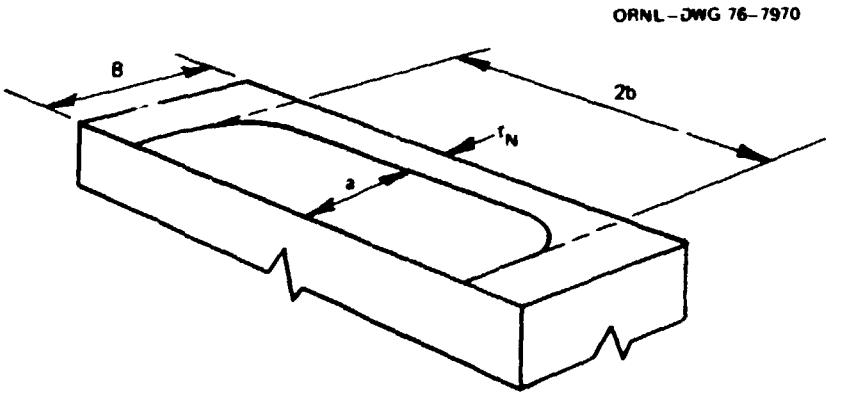

Fig. 5.8. Net section flaw configuration for COD analyses.

For model V7E-A3, using b = 32.39 mm (1.275 in.), σ_Y = 497 MPa (72 ksi) ((which takes some account of the proximity of the flawed region of the model to the quenched surface of the forging prolongation), and K_c = 312 MN·m$^{-3/2}$ (284 ksi $\sqrt{\text{in.}}$). Eq. (22) gives σ/σ_Y = 1.13 and a rearrangement of Eq. (20) gives σ/σ_Y = 1.30. Consequentiy, from

$$p = \frac{\sigma}{(r/B)} , \tag{23}$$

the estimated failure pressure is 287 MPa (41.6 ksi), which is still considerably above the actual failure pressure.

Irwin's second version of the COD analysis for the central region of a deep part-through surface crack[25] differs from the previous analysis in three respects. First, the stress in the fully yielded ligament is estimated to be 15% above the uniaxial yield stress σ_Y due to strain hardening. Second, the equation for estimating the center-line COD of the fictitious through crack is based on the strip yield model, instead of LEFM with a small scale yielding plastic zone size correction. Third, the total stress acting across the strip yield plastic zones is estimated to be 5% above the uniaxial yield stress to take account of biaxiality. Thus, the basic equation of this method of analysis, for uniform tensile loading, is[25]

$$\delta_c = \frac{8\sigma_Y b}{\pi E} \tanh^{-1}\left(\sin\frac{\pi\sigma}{2\sigma_Y}\right) , \tag{24}$$

where σ is the effective remote tensile stress, which is related to the actual remote tensile stress σ by

$$\sigma' = \sigma - 1.15\sigma_Y\left(1 - \frac{a}{B}\right) , \tag{25}$$

and where the effective yield stress in the plastic zone σ_Y' is given by

$$\sigma_Y' = 1.05\sigma_Y - 1.15\sigma_Y\left(1 - \frac{a}{B}\right) . \tag{26}$$

Using

$$\delta_c = \frac{4}{\pi}\frac{K_c^2}{E\sigma_Y} , \tag{27}$$

the resulting expression for failure pressure becomes

$$\frac{p}{\sigma_Y} = \frac{\frac{\sigma_Y'}{\sigma_Y}\frac{\sin^{-1}u}{\pi/2} + 1.15\left(1 - \frac{a}{B}\right)}{(r/B)} . \tag{28}$$

where

$$u = \tanh x = \frac{e^{2x} - 1}{e^{2x} + 1} . \tag{29}$$

and

$$2x = \frac{(K_c \sigma_y)^2}{b[1.15(a/B) + 0.10]} \tag{30}$$

For the same input values used in the first version of the COD analysis, the calculated failure pressure is 232 MPa (33.7 ksi), which is still too high.

Calculations for Model V7E-A3 Based on a Ligament-Size-Dependent Fracture Toughness

Because all the previous calculations based on fracture toughness had overestimated the strength of model V7E-A3, it was considered likely that a common factor could have been responsible for the overestimates. Since the analytical models themselves were quite different but the same value of the fracture toughness was used for all three of the calculations, it was considered most probable that the value of the fracture toughness used was the common factor responsible for the overestimates. Upper-shelf fracture toughness values obtained at test specimen maximum loads tend to decrease with decreasing specimen size,[26] but the distance parallel to the crack tip for a deep part-through surface crack in a pressure vessel cylinder, which plays the same role as the test specimen thickness, is effectively infinite. Therefore, the thickness of the remaining ligament ahead of the crack tip appeared to be the only dimension to which upper-shelf fracture toughness could be related. Consequently, some of the previous calculations were repeated, using a value of the upper-shelf fracture toughness that was related to the size of the remaining ligament. For very small specimen sizes, the upper-shelf fracture toughness varies approximately in proportion to the square root of the specimen size. Since the ligament thickness in model V7E-A3 was one-sixth the vessel wall thickness, the effective upper-shelf ligament fracture toughness was estimated as

$$K_{Ic} = K_{Ic(0.85)} \sqrt{\frac{1}{6}} = 127 \text{ MN·m}^{-3/2} (116 \text{ ksi}\sqrt{\text{in.}}) . \tag{31}$$

Using $K_{Icd} = K_{Ic}$ and $C = 1.44$ as estimated by the ORNL method, Eq. (17) gives an estimated failure pressure of 166 MPa (24.0 ksi), which agrees very well with the actual failure pressure. Applying the same value of K_{Ic} to the second type of COD analysis,[25] Eq. (30) gives $2x = 2.37$, Eq. (29) gives $u = 0.829$, and Eq. (28) gives an estimated failure pressure of 160 MPa (23.3 ksi), which is only slightly higher than the actual failure pressure. Thus, the approach of using a ligament-size-dependent value of fracture toughness for deep part-through surface cracks in the upper-shelf temperature range resulted in good estimates of fracture strength for model V7E-A3. Furthermore, the use of the ORNL method for estimating the shape factor for a deep part-through surface flaw was supported by these results, as well as by the agreement obtained previously between the ORNL method and the method described in Appendix A to Section XI of the ASME code for nuclear vessels.

Calculations for Model V7E-A2

The foregoing calculations for model V7E-A3 indicate that, for deep part-through surface cracks in the upper-shelf temperature range, plastic instability may occur in the region surrounding the crack before the onset of crack extension. If such is the case, then failure occurs at the onset of crack extension in the ligament, which is controlled by a value of the fracture toughness that depends on the thickness of the remaining ligament. This hypothesis was tested by applying it to model V7E-A2. For consistency, both the plastic instability and the fracture mechanics calculations were based on the equivalent semielliptical part-through surface crack. Substituting the trapezoidal flaw dimensions for model V7E-A2 given in Table 5.2 into Eq. (3) gives $2b_e/2b = 1.01$. The pressure[13,23] for local plastic instability around the flaw was estimated from

$$p_f = \sigma^* (Y - 1)\left(1 - \frac{A_c}{A}\right) . \tag{32}$$

where σ^* is the hoop stress for plastic instability in a thin-walled cylinder under internal pressure with closed ends.[13]

$$Y = \frac{r_o}{r_i} . \tag{33}$$

and, neglecting stable crack growth, A_c is the crack area for the equivalent semiellipse. A_c is given by

$$A_c = \frac{\pi a b_e}{2} . \tag{34}$$

and A is the effective trapezoidal load-bearing area[13] given by

$$A = (2b_e + t)\,t . \tag{35}$$

Using the flaw dimensions given in Table 5.2, a value of $\sigma^* = 609$ MPa (88.3 ksi) taken from Ref. 13, and noting that for the intermediate test vessels and their geometrically similar models, $Y = 1.444$, Eq. (32) gives a pressure for local plastic instability around the flaw in model V7E-A2 of 152 MPa (22.0 ksi), which is less than the measured failure pressure of 190 MPa (27.5 ksi), as expected.

The elastic shape factor for the equivalent semielliptical surface crack in model V7E-A2 was estimated by the ORNL method. The value of Φ was calculated from the equation[17]

$$\Phi^2 = 1 + 4.593\left(\frac{a}{2b_e}\right)^{1.65} . \tag{36}$$

which, for $a/2b_e = 0.414$, gives $\Phi^2 = 2.07$. For $a/t = 0.835$, Eq. (15) gives $M_2(0) = 1.70$. Thus, from Eq. (14),

$$C = \frac{(1.025)(1.70)}{\sqrt{2.07}} = 1.21 .$$

Since the crack depths in models V7E-A2 and V7E-A3 were the same, the ligament fracture toughnesses were also expected to be the same. Therefore, the elastically calculated failure pressure for model V7E-A2 was estimated as the value calculated for model V7E-A3 from Eq. (17) multiplied by the ratio of the shape factors (1.44/1.21), or 197 MPa (28.6 ksi). Since this value exceeds the gross yield pressure, it was substituted into Eq. (18) to obtain an elastic estimate of the strain at failure, which was 0.149%, a value somewhat less than the actual failure strain. Then, entering the pressure-strain diagram in Fig. 5.6 at this value of strain, the failure pressure was reestimated as 174 MPa (25.2 ksi), which is also somewhat less than the actual failure pressure.

Since model V7E-A2 failed at about the onset of gross yielding in the cylindrical region of the model (Fig. 5.6), the above underestimate of the failure pressure and strain by an LEFM calculation based on strain was not surprising. Consequently, an analysis by the tangent modulus method[23] was performed next to further check the value of the elastically calculated shape factor, which is supposed to retain its value in the elastic-plastic range for this method of analysis, and also to establish a capability for estimating failure pressures for intermediate test vessel V-7 in the elastic-plastic range, at least up to the gross yield pressure of the vessel. The tangent modulus method is an approximate incremental method of elastic-plastic fracture analysis and is described in detail in Appendix H of Ref. 23. The basic equation of this method of analysis is

$$\Delta\epsilon_f \sqrt{\rho} = 2C\sqrt{a}\sqrt{\frac{E_g}{E_n}}\,\Delta\lambda \quad . \tag{37}$$

where ϵ_f is the notch root strain at fracture, ρ is the notch root radius, C is the elastically calculated fracture mechanics shape factor, a is the flaw size, E_g is the tangent modulus corresponding to the gross (nominal) strain λ, and E_n is the tangent modulus at the notch tip. The quantity $\epsilon_f \sqrt{\rho}$, known as the notch ductility factor, is related to the fracture toughness by[23]

$$\epsilon_f \sqrt{\rho} = \frac{20}{\sqrt{\pi}} \epsilon_Y \left(\frac{K_c}{\sigma_Y}\right)^2 . \tag{38}$$

where ϵ_Y is the yield strain. For a surface flaw in the cylindrical region of a pressure vessel,[23]

$$\sqrt{\frac{E_g}{E_n}} = 10 \quad , \quad 0 \leq \lambda \leq \epsilon_Y \quad . \tag{39}$$

For a yield stress of 497 MPa (72 ksi), $\epsilon_Y = 0.247\%$, and $K_c = 127$ MN·m$^{-3/2}$ (116 ksi$\sqrt{\text{in.}}$), $K_c/\sigma_Y = 25.7$ mm$^{1/2}$ (1.61 $\sqrt{\text{in.}}$). Therefore, from Eq. (38), $\epsilon_f \sqrt{\rho} = 69.5 \times 10^{-2}$ mm$^{1/2}$ (4.36×10^{-2} $\sqrt{\text{in.}}$). Rearranging Eq. (37) and integrating, under the assumption that $\lambda_f \leq \epsilon_Y$,

$$\lambda_f = \frac{\epsilon_f \sqrt{\rho}}{2C\sqrt{a}\,\sqrt{E_g/E_n}} . \tag{40}$$

Substituting the values given above along with a = 18.0 mm (0.71 in.) and C = 1.21 into Eq. (40) gives λ_f = 0.213%, which is less than the yield strain, as assumed, and only slightly greater than the measured failure

strain. From Fig. 5.6, the corresponding failure pressure is 190 MPa (27.5 ksi), which agrees exactly with the measured failure pressure.

The above results were interpreted to indicate that a satisfactory procedure for estimating failure pressures for deep external part-through surface cracks had been developed. Calculations were also made for model V4.3, but because of the erroneous flaw dimensions used, as mentioned earlier, the results were only fortuitously useful. Even though the flaw dimensions used were too small, the estimate of failure pressure for model V4.3 by LEFM based on strain was still conservative. However, the tangent modulus method overpredicted both the failure pressure and the failure strain because of the input error in flaw dimensions.

In summary, the above exploratory calculations for the hydraulically loaded 1/7.06-scale models with different flaw sizes established the method of analysis to be used for designing the flaw in intermediate test vessel V-7. The method of analysis was (1) plastic instability, using a trapezoidal effective load-bearing area, as used previously,[13,27] and (2) LEFM based on strain, assuming no stable crack growth, a ligament-size-dependent fracture toughness, and a shape factor estimated by the ORNL method

FLAW DESIGN FOR INTERMEDIATE TEST VESSEL V-7

Flaw Shape

As discussed previously, a trapezoidal shape was selected for the flaw in intermediate test vessel V-7 in order to promote crack extension over a significant distance at the base of the crack. Concurrent with the flawed model experiments discussed above, EB welding experiments were performed on pieces of steel plate inclined at various angles to the direction of the welding beam and on steel blocks with deeply machined trapezoidal notches (Fig. 3.7) in order to select a slope angle for the notch sides and to choose a machined notch width that would minimize magnetic effects on the electron beam. It was determined that a machined notch width of 25.4 mm (1 in.) would be satisfactory with respect to vessel magnetic-field-induced deviations in the direction of the electron beam. This width was also considered acceptable with respect to its effects on crack tip conditions, based on an estimated EB weld depth of 7.94 mm ($^5/_{16}$ in.), especially in view of the expected complete yielding of the ligament before failure. A slope angle of 45° was selected for the sides of the trapezoid in order to operate the vertical and horizontal speed control motors of the EB welder at the same speed and thereby avoid small welding speed variations due to interaction between the two motors. Welding on the side slopes was done in the uphill direction to prevent the molten metal droplet on the bottom of the notch from running downhill into the weld beam.

Ligament Fracture Toughness

In order to estimate the effective fracture toughness of the ligament beneath the tip of the crack and the inside surface of intermediate test vessel V-7, the fracture toughness data obtained by ORNL and by Westinghouse[21,22] from specimens removed from near the inside surface of the vessel cylinder prolongation were examined closely. Those data are listed in Table 5.3. A rearrangement of the data is given in Table 5.4, from which a plot of $(K_{Icm}/K_{Icl})^2$ vs the reciprocal of the specimen ligament size was prepared, as shown in Fig. 5.9. The value of K_{Icm} used for plotting Fig. 5.9 was an arbitrary selection for normalization purposes and was chosen as the value of K_{Icl} for precracked Charpy specimen 7V-201, as indicated in Table 5.4. Fitting a straight line by eye to the majority of the points plotted in Fig. 5.9, as discussed in Ref. 27, produced an estimate of the dependency of fracture toughness on ligament size, as

Table 5.3. Lower-bound static fracture toughness properties for near inside surface material of vessel V-7 at 93°C (200°F)[a]

Specimen No.	Thickness (mm)	Type of specimen	Orientation	Distance in from outside surface (mm)	K_{Icd} (MN·m$^{-3/2}$)
			ORNL specimens		
7V-201	10	PCCV	CA	129	219
7V-202	10	PCCV	CA	129	201
7V-228	10	PCCV	AC	129	162
7V-244	10	PCCV	CA	153	220
			Westinghouse specimens[21,22]		
V7D-8	21.6	CT	CA		319
V7D-9	21.6	CT	CA		336
V7D-31	102	CT	CA		446

[a]1 MN·m$^{-3/2}$ = 0.9101 ksi $\sqrt{\text{in.}}$

Table 5.4. Data for estimating fracture toughness at 93°C (200°F) of near inside surface material of vessel V-7[a]

Specimen No.	$\frac{a}{W}$	$1-\frac{a}{W}$	a (mm)	l (mm)	$\frac{1}{l}$ (mm^{-1})	K_{Icd} (MN·m$^{-3/2}$)	$\left(\frac{K_{Icm}}{K_{Icl}}\right)^2$
7V-201	0.475	0.525		5.25	19.0	219	1.000
7V-202	0.506	0.494		4.94	20.2	201	1.194
7V-228	0.496	0.504		5.04	19.8	162	1.826
7V-244	0.530	0.470		4.70	21.3	220	0.990
V7D-8			22.2	21.0	4.76	319	0.472
V7D-9			23.9	19.3	5.18	336	0.424
V7D-31			102.1	101	0.99	446	0.241

[a]1 MN·m$^{-3/2}$ = 0.9101 ksi $\sqrt{\text{in.}}$

given by

$$K_{Icl} = \frac{K_{Icm}}{\sqrt{0.2 + (l_0/l)}}, \tag{41}$$

where K_{Icm} = 219 MN·m$^{-3/2}$ (200 ksi $\sqrt{\text{in.}}$) and l_0 = 4.23 mm ($\frac{1}{6}$ in.).

Determination of the Ligament Size

Having determined, on the basis of the analysis of model test data discussed above, that the ligament size rather than the crack surface length was the most appropriate design variable for the flaw in intermediate test vessel V-7, a series of calculations was performed relating ligament size to the calculated

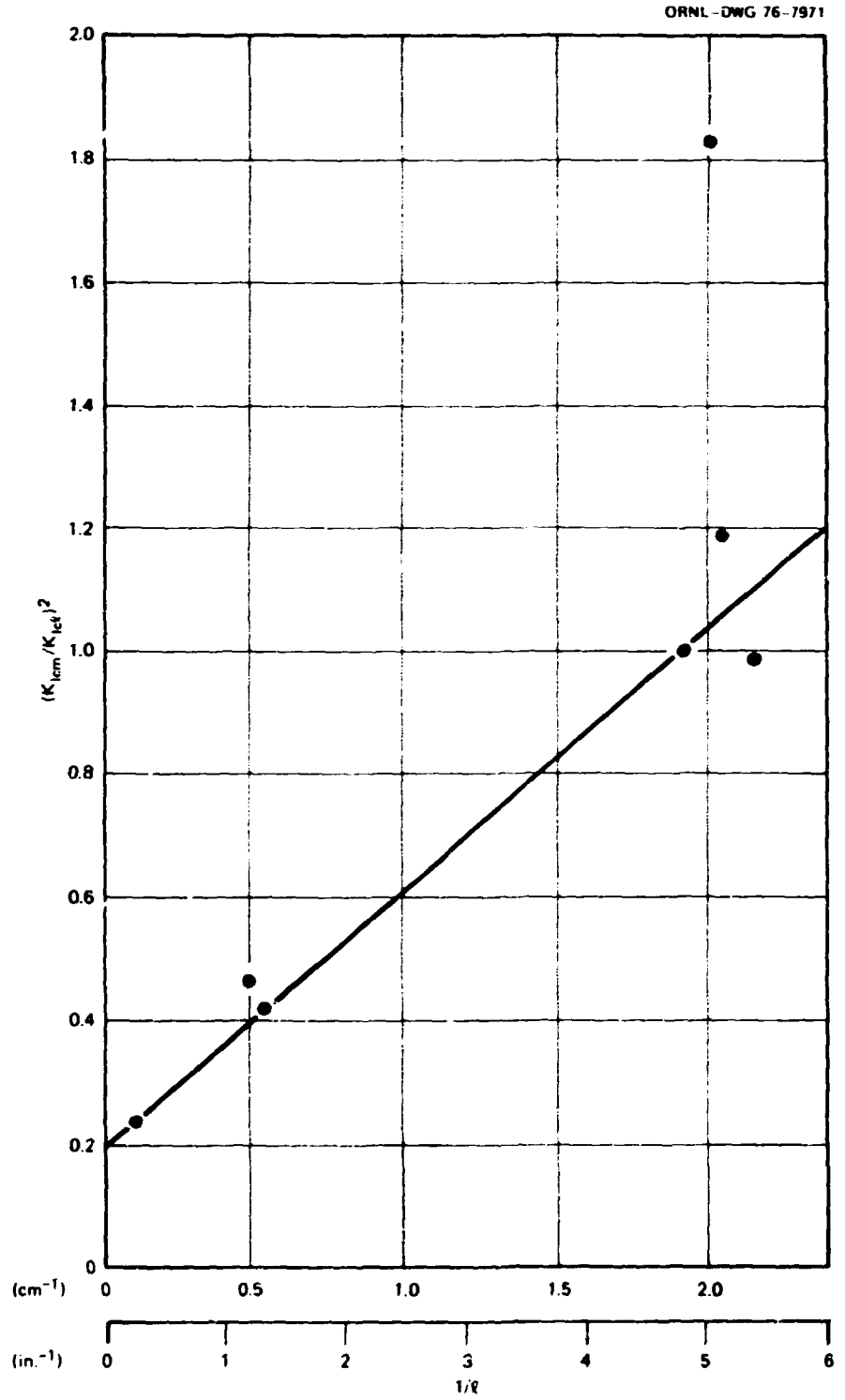

Fig. 5.9. Plot for determination of upper-shelf fracture toughness at 93°C (200°F) vs ligament thickness for intermediate test vessel V-7.

failure pressure. The basis of the calculations was Eq. (17), with the fracture toughness being the ligament-size-dependent fracture toughness, so that failure pressure was calculated from

$$p_f = \frac{K_{Ic}}{C\,(r/t)\sqrt{\pi a}} . \tag{42}$$

The shape factor C was estimated by the ORNL method, using Eqs. (14), (15), and (36). Thus, substituting Eqs. (41), (14), and (15) into Eq. (42) gives

$$p_f = \frac{K_{Icm}\,\Phi\sqrt{\cot \pi/2\,(a/t)}}{(r/t)\,\psi_0(0)\,\sqrt{2t}\,\sqrt{0.2 + (l_0/l)}} . \tag{43}$$

where

$$\frac{a}{t} = 1 - \frac{l}{t} . \tag{44}$$

For a trapezoidal flaw with 45° side slope angles,

$$w = 2(b - a) , \tag{45}$$

so that substituting Eq. (45) into Eq. (3) gives

$$\frac{2b_e}{2b} = \frac{2(1 - a/2b)}{\pi/2} . \tag{46}$$

Choosing a crack surface length $2b$ of 457 mm (18 in.) and estimating the crack depth as 127 mm (5 in.), Eq. (45) gives $2b_e/2b = 0.92$. Thus, $a/2b_e = 0.302$, and substituting this value into Eq. (36) gives $\Phi = 1.278$. Thus, for $K_{Icm} = 219$ MN·m$^{-3/2}$ (200 ksi $\sqrt{\text{in.}}$), $r/t = 2.25$, $\psi_0(0) = 1.025$, and $t = 152$ mm (6 in.), Eq. (43) reduces to

$$p_f = k\,\frac{32.0\sqrt{\cot \pi/2\,(a/t)}}{\sqrt{0.2 + (l_0/l)}} , \tag{47}$$

where $k = 1.0$ for pressure (ksi) and 6.895 for pressure (MPa), and $l_0 = 4.23$ mm ($\frac{1}{6}$ in.). The resulting elastically calculated values of crack initiation pressure vs ligament thickness for intermediate test vessel V-7, based on Eqs. (47) and (44), are listed in Table 5.5 and are shown plotted in Fig. 5.10. Considering the fact that the innovation of a ligament-size-dependent fracture toughness was involved in the calculations and that an upward extrapolation by a size factor of 7.06 from the model test data was also required, it was decided to choose a ligament thickness that would correspond to a calculated failure pressure lying about midway between the code design pressure and the gross yield pressure of the vessel. Thus, a ligament

Table 5.5. Elastically calculated values of crack initiation pressure vs ligament thickness for vessel V-7

Ligament thickness [mm (in.)]	Pressure [MPa (ksi)]
25.4 (1.0)	189 (27.4)
22.9 (0.9)	174 (25.3)
20.3 (0.8)	159 (23.1)
17.8 (0.7)	143 (20.8)
15.2 (0.6)	127 (18.4)
12.7 (0.5)	110 (15.9)
10.2 (0.4)	91 (13.2)
7.6 (0.3)	71 (10.3)

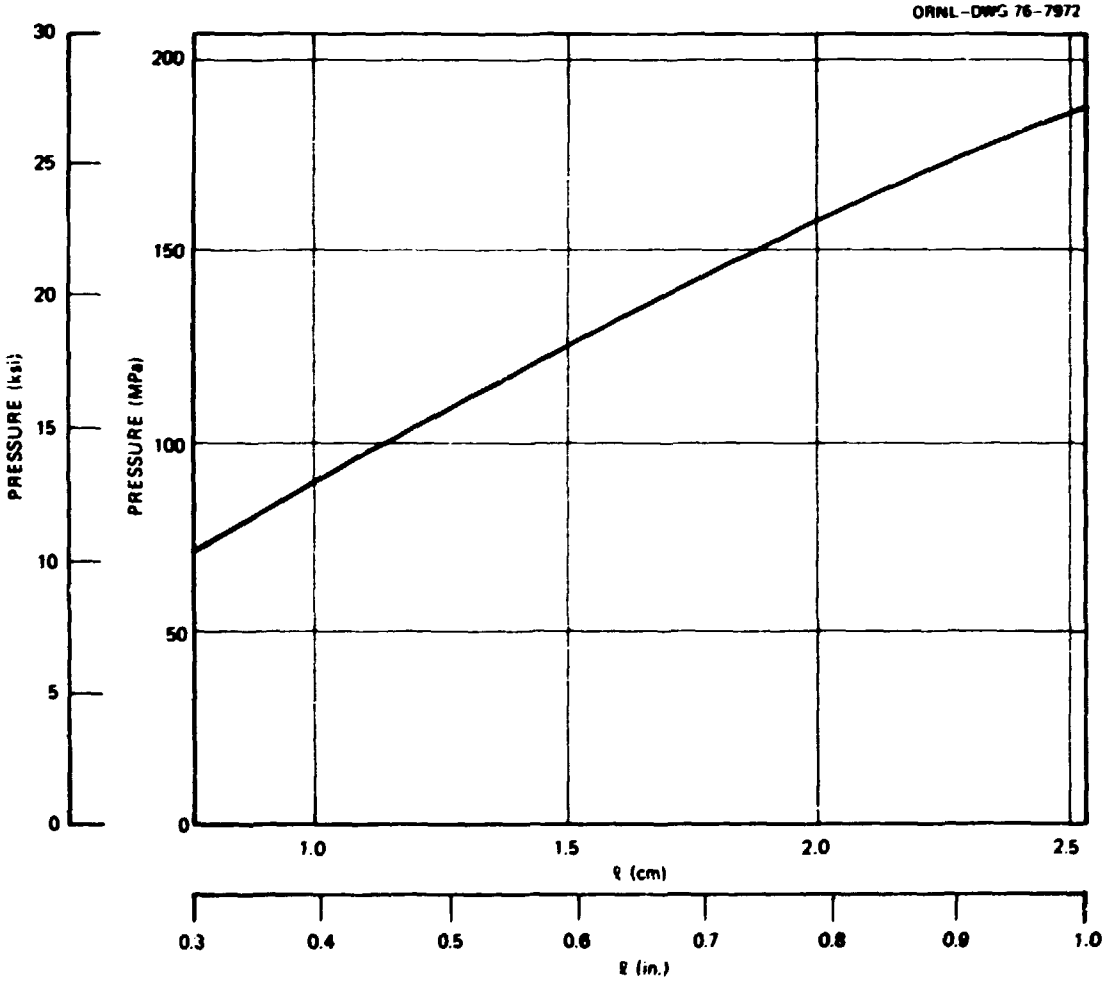

Fig. 5.10. Approximate failure pressure vs ligament thickness for intermediate test vessel V-7.

thickness of 17.5 mm ($^{11}/_{16}$ in.) was selected, and since the expected electron-beam weld depth was 7.94 mm ($^{5}/_{16}$ in.), the notch in intermediate test vessel V-7 was machined 127 mm (5 in.) deep. The estimated failure pressure, as determined from Fig. 5.10, was 141 MPa (20.5 ksi).

ORNL PRETEST STRENGTH ANALYSIS OF INTERMEDIATE TEST VESSEL V-7 FOR THE SELECTED FLAW DIMENSIONS

Equivalent Semiellipse

The final design of the flaw in intermediate test vessel V-7 is shown in Fig. 3.4. Note that the expected electron-beam weld depth along the ligament and the expected horizontal distance across the electron-beam weld on the inclined portions of the flaw were both 7.94 mm ($^{5}/_{16}$ in.). Thus, the crack dimensions used for analysis were $2b = 473.1$ mm (18.625 in.), $a = 135.0$ mm (5.313 in.), and $w = 203.2$ mm (8 in.). Thus, from Eq. (3), $2b_e/2b = 0.910$ and therefore $2b_e = 430.5$ mm (16.95 in.).

Pressure for Local Plastic Instability

The pressure for local plastic instability around the flaw was estimated from Eq. (32). Based on Eqs. (34) and (35), the ratio of crack area to effective load-bearing area was 0.513. Thus, for $(Y - 1) = 0.444$ and $\sigma^* = 609$ MPa (88.3 ksi), Eq. (32) gives $p_f = 132$ MPa (19.1 ksi). This pressure was expected to be less than the actual failure pressure.

Pressure for Crack Initiation

The elastic shape factor for the flaw in intermediate test vessel V-7 was calculated from Eq. (14). For $2b_e = 430.5$ mm (16.95 in.), $a/2b_e = 0.313$. Substituting this value into Eq. (36) gives $\Phi = 1.294$. For $a/t = 0.885$, Eq. (15) gives $M_2(0) = 1.985$. Thus, for $\psi_0(0) = 1.025$, Eq. (14) gives $C = 1.572$.

The ligament fracture toughness was calculated from Eq. (41). For $K_{Icm} = 219$ MN·m$^{-3/2}$ (200 ksi $\sqrt{\text{in.}}$), $l = 17.5$ mm ($^{11}/_{16}$ in.), and $l_0 = 4.23$ mm ($^{1}/_{6}$ in.), Eq. (41) gives $K_{Icl} = 330$ MN·m$^{-3/2}$ (301 ksi $\sqrt{\text{in.}}$).

The failure pressure was calculated from Eq. (42). Using the values of K_{Icl} and C given above, with $a = 135$ mm (5.31 in.) and $r/t = 2.25$, Eq. (42) gives a calculated failure pressure of 143 MPa (20.8 ksi). Therefore, crack initiation was expected to occur after the onset of local plastic instability and thus lead immediately to failure.

Leak or Break Estimate

The question of whether intermediate test vessel V-7 could leak without bursting was investigated by calculating the elastic stress-intensity factor for the through-thickness crack that forms upon the separation of the remaining ligament beneath the deep surface crack and then comparing that value to the estimated full-thickness fracture toughness. The through-thickness full-restraint fracture toughness for intermediate test vessel V-7 was estimated from Eq. (41) to be $K_{Ic6} = 460$ MN·m$^{-3/2}$ (419 ksi $\sqrt{\text{in.}}$).

The stress-intensity factor for a through-thickness longitudinal crack in vessel V-7 was calculated from the equation[17]

$$K_I = \frac{C\sigma\sqrt{\pi c}}{\sqrt{1 - (C^2/2)(\sigma/\sigma_Y)^2}} , \qquad (48)$$

where c is the half length of the through-thickness crack and the denominator in Eq. (48) provides a plane stress plastic zone size correction to the crack size. The shape factor C was estimated from the equation[28]

$$C = M\sqrt{\frac{1+4\nu}{2}}, \tag{49}$$

where, for $\nu = 0.3$, $(1 + 4\nu)/2 = 1.1$, and M is a bulging factor that was determined graphically from the curve for M_{exact} in Fig. 5.11. Based on a mean shell radius R of 419 mm (16.5 in.) and a conservatively estimated half crack length c of 236 mm (9.31 in.), the value of M obtained from Fig. 5.11 was 1.45. At a pressure of 143 MPa (20.8 ksi), the nominal circumferential stress is 323 MPa (46.9 ksi); therefore, using a yield stress of 497 MPa (72 ksi), Eq. (48) gives $K_I = 593$ MN·m$^{-3/2}$ (541 ksi $\sqrt{\text{in.}}$). Thus, if full transverse restraint conditions prevailed, leakage without burst was not predicted. However, in a cylindrical vessel under internal pressure, through-thickness contraction must occur, and therefore full transverse restraint along the leading edge of a through-thickness crack cannot exist. Using Irwin's estimate of the elevation of fracture toughness due to less than full through-thickness transverse restraint as given by Eq. (1) and an even more conservative value (for this purpose) of $\sigma_Y = 517$ MPa (75 ksi), the effective value of the fracture toughness resisting continued extension of a through-thickness longitudinal crack was estimated to be 2863 MN·m$^{-3/2}$ (2610 ksi $\sqrt{\text{in.}}$). Thus, considering the development of less than full transverse restraint along the crack front, a leak without break was seen to be a distinct possibility. However, for purposes of a conservative prediction, a leak without break was still not considered a certainty.

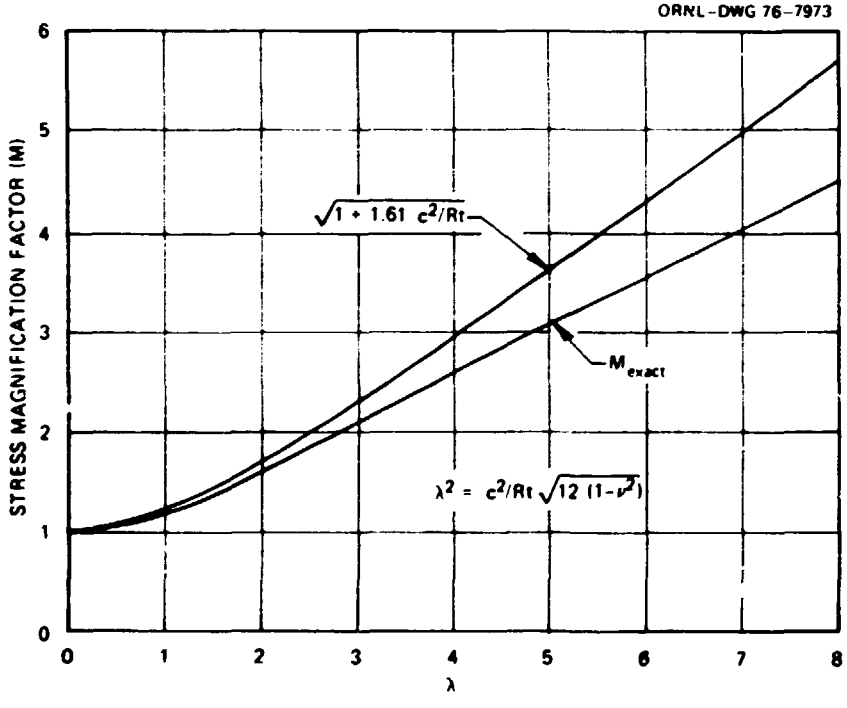

Fig. 5.11. Stress-intensity factor magnification due to bulging for a longitudinal crack of half length c in a cylindrical shell of mean radius R and thickness t under internal pressure loading.[28]

OTHER PRETEST ESTIMATES FOR INTERMEDIATE TEST VESSEL V-7

Linear Elastic Fracture Mechanics based on Strain
(analysis performed by C. Buchalet, Westinghouse PWR Systems Division)

For this analysis, the trapezoidal flaw was considered to be 457 mm (18 in.) long on the surface and 135 mm (5.31 in.) deep and to have a ligament length of 203 mm (8 in.). The surface length of a semielliptical flaw with equal depth and equal area is 420.4 mm (16.55 in.). The equation used for the stress-intensity factor, assuming a uniform tensile stress equal to the average circumferential stress, was

$$K_I = \frac{F_1}{\Phi}(2.25p)\sqrt{\pi a} \ . \tag{50}$$

where F_1 is the corresponding shape factor for a continuous external surface crack of the same depth and Φ is the elliptical integral of the second kind for the equivalent semielliptical surface flaw. The value of F_1 was actually obtained by using an unpublished version of the Levy-Rice line spring model, but in this case it can be closely approximated by multiplying the value of F_1 given in Fig. 5.12, which is taken from Ref. 29, by the prescribed front face free surface magnification factor of 1.12. The value of F_1 used by Buchalet was 2.55; the value of $1.12F_1$ obtained by using Fig. 5.12 is 2.50. The curves in Fig. 5.12 are based on the assumption that the back surface does not change curvature due to bending. The value of Φ used by Buchalet was 1.32; the value obtained from Eq. (36), which agrees with exact tabulated values, is 1.305. The fracture toughness value used in these calculations was $K_{Icd} = 436\ \mathrm{MN \cdot m^{-3/2}}$ ($397\ \mathrm{ksi}\sqrt{\mathrm{in.}}$), which is the average value of K_{Ic4} obtained by Westinghouse[22] with three 4T compact-tension specimens machined from the cylinder prolongation of vessel V-7.

Rearranging Eq. (50) to calculate a pseudoelastic failure pressure gives

$$p_f^* = \frac{\Phi K_{Icd}}{2.25F_1\sqrt{\pi a}} \ . \tag{51}$$

which, using Buchalet's numerical values, leads to a calculated pressure of 154 MPa (22.4 ksi). Substituting this pressure into Eq. (18) gives an elastically calculated failure strain of 0.12%, which, from Fig. 5.6, corresponds to an estimated failure pressure of 152 MPa (22 ksi). The elastically calculated failure pressure based on the value of $1.12F_1$ obtained by using Fig. 5.12 and the value of Φ obtained from Eq. (36) differs from the value given above by less than 1%, thus leading to virtually the same final estimate of failure pressure and failure strain. No comments were made in this analysis concerning whether the vessel would leak or burst.

Estimate Based on Metallurgical Considerations
(estimate prepared by D. A. Canonico, ORNL)

Based presumably on the fact that the yield stress in the near inside surface ligament considerably exceeds the yield stress of the midthickness material and on the appearance of previous fracture surfaces examined,[13] it was predicted (by an unspecified method) that failure would occur by rapid crack extension at an internal pressure of 159 MPa (23 ksi). The propagating crack was expected to arrest before reaching the circumferential welds, but a leak without rupture failure was not expected.

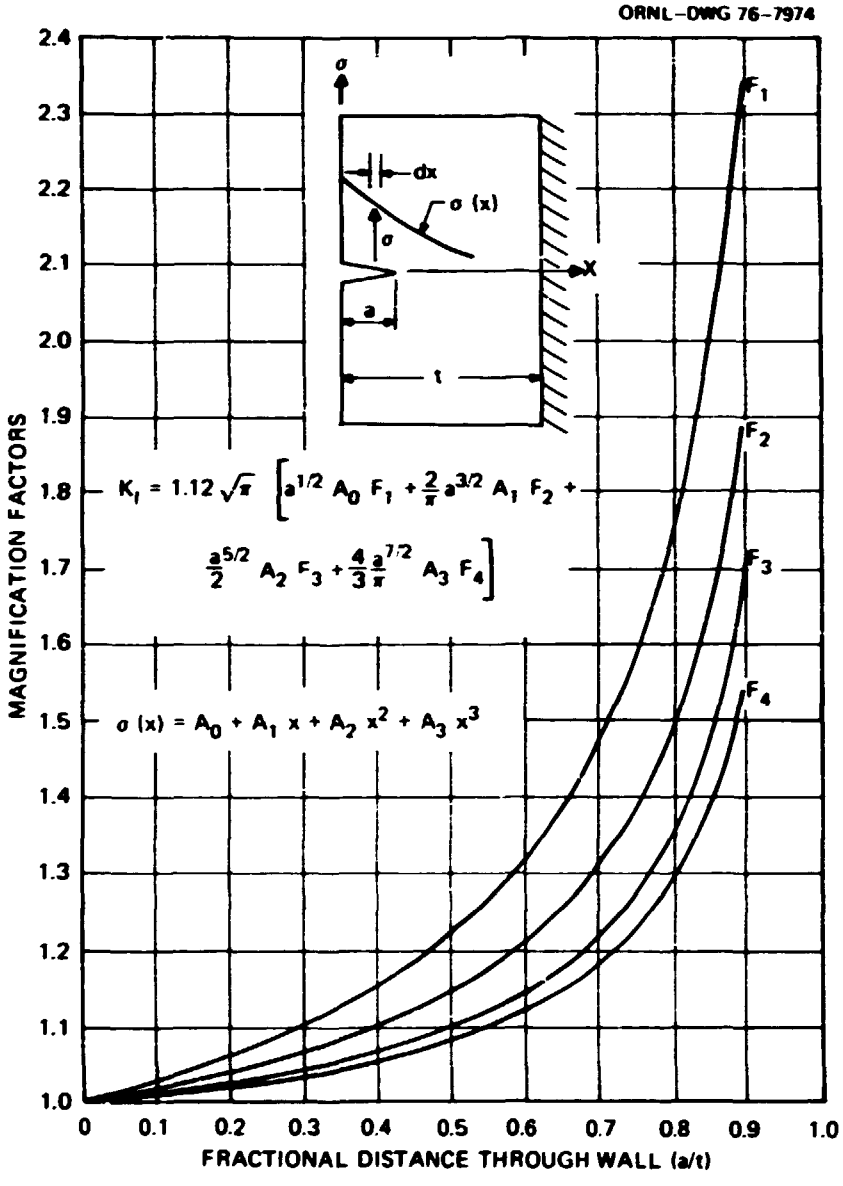

Fig. 5.12. Finite-thickness stress-intensity factor magnification curves for a continuous edge crack in a plate restrained against back surface curvature and subjected to a nominal stress distribution described by a cubic polynomial.[29]

DISCUSSION

Since both the ORNL and the Westinghouse pretest estimates of failure pressure for intermediate test vessel V-7 were accurate within 3%, no posttest calculations were considered necessary for the test vessel itself. However, since the Westinghouse pretest analysis was based on a higher elastic fracture mechanics shape factor than the ORNL analysis, but, implicitly, also on the full section fracture toughness, it is of interest to apply this same method of analysis to model V7E-A3 to see if it retains its accuracy. Because of

the unavailability of the line spring analysis, the shape factor for this calculation was estimated by means of Fig. 5.12, as discussed earlier, and the equation

$$C = \frac{1.12F_1}{\Phi} . \tag{52}$$

For a/t = 0.835, Fig. 5.12 gives F_1 = 1.91 and, for $a/2b_e$ = 0.253, Eq. (36) gives Φ = 1.215. Thus, substituting these values into Eq. (52) gives C = 1.761. The value of $K_{Ic(0.85)}$ given previously is 312 $MN \cdot m^{-3/2}$ (284 ksi $\sqrt{in.}$) and the crack depth is 4.32 mm (0.71 in.), so that Eq. (17) gives an elastically calculated failure pressure of 332 MPa (48.1 ksi). Substituting this value of pressure into Eq. (18) then gives a failure strain estimate of 0.25%, which is considerably above the actual failure strain of 0.12%. Thus, there is some question, although based on only indirect evidence, concerning the expected consistent accuracy of the Westinghouse analysis method for vessel and crack dimensions other than those used for intermediate test vessel V-7.

REFERENCES

1. G. R. Irwin et al., "Basic Aspects of Crack Growth and Fracture," Chapter 7 in *Technology of Steel Pressure Vessels for Water-Cooled Nuclear Reactors*, G. D. Whitman, G. C. Robinson, and A. W. Savolainen, eds., ORNL-NSIC-21 (December 1967); see also NRL-6598 (Nov. 21, 1967).
2. Letter from R. F. Fraley, Executive Secretary of the Advisory Committee on Reactor Safeguards, to Milton Shaw, Director, USAEC Division of Reactor Development and Technology, Jan. 16, 1967.
3. L. E. Steele, Questions Related to the Proposed Simulated Pressure Vessel Service Test, Enclosure 3 to Minutes of the Fifth Meeting of the HSST Program Planning Committee held at Oak Ridge National Laboratory, Oak Ridge, Tenn., Sept. 11–12, 1967.
4. J. G. Merkle, S. E. Moore, and F. J. Witt, "Design of Nuclear Pressure Vessels," Chapter 6 in *Technology of Steel Pressure Vessels for Water-Cooled Nuclear Reactors*, G. D. Whitman, G. C. Robinson, and A. W. Savolainen, eds., ORNL-NSIC-21 (December 1967).
5. H. T. Corten, Simulated Service Test in HSST Program, Enclosure 1 to Minutes of the Sixth Meeting of the HSST Program Planning Committee held at Oak Ridge National Laboratory, Oak Ridge, Tenn., Oct. 23–24, 1967.
6. H. T. Corten, The Simulated Service Tests in the HSST Program (preliminary draft 3), notes prepared at Oak Ridge National Laboratory for presentation to the HSST Program Planning Committee, Mar. 21 and 22, 1968.
7. F. J. Witt, The Intermediate Vessel Test Series of the Simulated Service Tests, notes prepared at Oak Ridge National Laboratory for presentation to the Reactor Pressure Vessel Subcommittee of the Advisory Committee on Reactor Safeguards, Washington, D.C., Apr. 4, 1972.
8. J. G. Merkle, "Summary of Small-Scale Steel Model Test Data," *Quart. Progr. Rep. Reactor Safety Programs Sponsored by the NRC Division of Reactor Safety Research April–June 1975*, ORNL/TM-5021, Vol. II, pp. 14–15.
9. R. W. Derby, "Fracture Studies of Model Pressure Vessels Made of Nuclear Grade Steel," *Proceedings of the First International Conference on Structural Mechanics in Reactor Technology, Berlin, Germany, Sept. 20–24, 1972*, Paper G 6/5, Vol. 4, Part G, pp. 469–85.

10. L. F. Kooistra, letter to R. W. Derby concerning intermediate vessel tests, Oak Ridge National Laboratory, Oak Ridge, Tenn., Oct. 26, 1971 (internal correspondence).
11. R. W. Derby, letter to G. D. Whitman concerning the influence of flaw depth, Oak Ridge National Laboratory, Oak Ridge, Tenn., Oct. 3, 1972 (internal correspondence).
12. Letter from D. B. Trauger, Associate Director, Oak Ridge National Laboratory, to Milton Shaw, Director, Division of Reactor Development and Technology, USAEC, concerning "Testing of Intermediate Test Vessels at Near Design Conditions – HSST Program," Nov. 24, 1972.
13. R. W. Derby et al., *Test of 6-in.-thick Pressure Vessels. Series 1: Intermediate Test Vessels V-1 and V-2*, ORNL-4895 (February 1974).
14. A. E. Harms and C. W. Smith, *Stress Intensity Factors for Long, Deep Surface Flaws in Plates Under Extensional Fields*, VPI-E-73-6, Virginia Polytechnic Institute and State University, Blacksburg, Va. (February 1973).
15. J. F. Kiefner et al., "Failure Stress Levels of Flaws in Pressurized Cylinders," ASTM STP-536, pp. 461–81 (1973).
16. F. W. Smith and M. J. Alavi, "Stress Intensity Factors for a Part-Circular Surface Flaw," *Proceedings of the First International Conference on Pressure Vessel Technology, Delft, the Netherlands*, Part II, pp. 793–80, ASME, 1969.
17. J. G. Merkle, *A Review of Some of the Existing Stress Intensity Factor Solutions for Part-Through Surface Cracks*, ORNL/TM-3983 (January 1973).
18. J. C. Newman, "Fracture Analysis of Surface and Through-Cracked Sheets and Plates," paper presented at the Symposium on Fracture and Fatigue, Washington, D.C., May 3–5, 1972.
19. J. G. Merkle, "Stress Intensity Factor Estimates for Part-Through Surface Cracks in Plates Under Combined Tension and Bending," *Quart. Progr. Rep. Reactor Safety Programs Sponsored by the NRC Division of Reactor Safety Research July–September 1974*, ORNL/TM-4729, Vol. II, pp. 3–32.
20. ASME Boiler and Pressure Vessel Code, Section XI, Rules for Inservice Inspection of Nuclear Power Plant Components, 1974 Edition, American Society of Mechanical Engineers, New York, July 1, 1974.
21. G. D. Whitman, *Quart. Progr. Rep. Reactor Safety Programs Sponsored by the NRC Division of Reactor Safety Research April–June 1974*, ORNL/TM-4655, Vol. II.
22. T. R. Mager, S. E. Yanichko, and L. R. Singer, *Fracture Toughness Characterization of HSST Intermediate Pressure Vessel Material*, WCAP-8456 (also HSSTP TR-38) (December 1974).
23. R. H. Bryan et al., *Test of 6-in.-thick Pressure Vessels. Series 2. Intermediate Test Vessels V-3, V-4, and V-6*, ORNL-5059 (November 1975).
24. G. R. Irwin and H. T. Corten, *Evaluating the Feasibility of Basing Pipeline Operating Pressure on In-Place Hydrostatic Test Pressure*, report to Northern Natural Gas Company and El Paso Natural Gas Company (November 1968).
25. G. R. Irwin, "Characterization of Part-Through Cracks in Tension," *The Surface Crack: Physical Problems and Computational Solutions*, pp. 1–10, ASME, 1972.
26. F. J. Witt and T. R. Mager, *A Procedure for Determining Bounding Values on Fracture Toughness K_{Ic} at Any Temperature*, ORNL/TM-3891 (October 1972).
27. J. G. Merkle, "Analytical Applications of the J-Integral," *Progress in Flaw Growth and Fracture Toughness Testing*, ASTM STP-536, pp. 264–80, 1973.
28. R. J. Eiber et al., *Review of Through-Wall Critical Crack Formulations for Piping and Cylindrical Vessels*, BMI-1883 (May 1970).
29. C. Buchalet, "Fracture Prevention for Reactor Vessels, Part I: Proposed Fracture Analysis Method for Complex Geometries, and Loadings" (draft), Westinghouse Electric Corporation, Pittsburgh, Pa. (June 1973).

6. Conclusions

Intermediate test vessel V-7 was the sixth intermediate-size vessel to be tested with a flaw in the cylindrical section. The flaws at which failure occurred in the intermediate test vessels were all on the outside surface with the plane of the flaw lying in a radial-axial plane. The flaw sizes and test conditions are summarized in Table 6.1. Vessel V-7 is the only intermediate vessel tested with a flaw in ASTM A533, grade B, class 1 material.

The five tests in series 1 and 2 were performed with flaws extending less than halfway through the thickness of the cylinders. As indicated in Tables 6.1 and 6.2, the test conditions and modes of failure ranged from low temperature (in the toughness transition range), for which fracture was rapid and extensive, to high temperature (in the static and dynamic toughness upper-shelf range). In the latter condition, test vessel V-6 ruptured in a shear mode and arrested. This result was obtained with test conditions more typical of normal reactor operating conditions insofar as toughness is concerned. While earlier tests had already demonstrated that crack initiation could be conservatively predicted for thick structures, the V-6 test also demonstrated that dynamic high-toughness upper-shelf conditions are not conducive to flat fracture.

Table 6.1. Intermediate vessel test conditions[a] for series 1, 2, and 3

Vessel No.	Flaw size (in.)		Test temperature [°F (°C)]	Fracture toughness K_c (ksi $\sqrt{in.}$)	Flaw description	
	a	2b			Location	Material
2[b]	2.53	8.30	32 (0)	184	Outside	A508-2
4[c]	3.00	8.25	75 (24)	160	Outside	Weld
1[b]	2.56	8.25	130 (54)	311	Outside	A508-2
3[c]	2.11	8.50	130 (54)	325	Outside	Weld
6[c]	1.87	5.25	190 (88)	369	Outside	Weld
7[d]	5.30	18.6	196 (91)	301	Outside	A533-B1

[a] 1 in. = 25.4 mm; 1 ksi $\sqrt{in.}$ = 1.0988 MN-m$^{-3/2}$.
[b] Series 1 tests.
[c] Series 2 tests.
[d] Series 3 tests.

The objectives of the V-7 test were generally the same as those of the earlier tests, but the specific objectives were unique, namely to investigate the potential for a leak without break in a reactor pressure vessel. To serve this purpose, it was desirable to design a test in which the leak could be induced while nominal stresses were at or below yield. As in the test of V-6, a test temperature was chosen to provide toughness in the specimen similar to that in an operating reactor vessel. The test of V-7 demonstrated a leak without break at a loading for which the inside surface of the vessel was about at yield. The vessel did not fail structurally during the test and possibly could have sustained the maximum pressure loading without failure if the system had been capable of maintaining the pressure.

As indicated in Table 6.1, the flaw in V-7 was much longer and deeper than the flaws in any other test. The failure pressure relative to design pressure was the lowest of all the intermediate vessel tests, 2.2 times

Table 6.2. Intermediate vessel test results for series 1, 2, and 3

Vessel No.	Maximum pressure p_f (ksi) and strain λ_f (%) at failure		Mode of failure	Calculated results		Load factor[b] (p_f/p_d)	Remarks
				LEFM[a] based on strain	Plastic instability		
2	p_f	27.9	Flat	27.4[c]		2.87	Transition range
	λ_f	0.194		0.206			
4	p_f	26.5	Mixed	26.2		2.73	
	λ_f	0.168		0.163			
1	p_f	28.8	Mixed	27.5[c]	29.9[d]	2.96	Static upper shelf
	λ_f	0.92		0.345			
3	p_f	31.0	Mixed	27.5[c]	31.5[d]	3.19	
	λ_f	1.47		0.398			
6	p_f	31.9	Shear	27.5	33.7[d]	3.28	Static and dynamic upper shelf
	λ_f	2.0		0.479			
7	p_f	21.4	Leak	20.8	19.1	2.20	
	λ_f	0.12		0.109			

[a] Linear elastic fracture mechanics.

[b] Design pressure p_d = 67.0 MPa (9.71 ksi).

[c] Earlier estimates of pressure, including those of Ref. 1, were based upon a less accurate estimate of the pressure-strain relationship for the intermediate vessels.

[d] Assuming 15% stable crack growth as suggested in Ref. 1.

design. One must note that, since burst did not occur as in the other tests, there is still no experimental determination of the ultimate failure loading of a thick cylinder containing a long flaw. Thus analytical predictions of burst pressures cannot be evaluated quantitatively by this test.

The testing of V-6 and V-7 leaves the question unresolved experimentally as to whether sustained loading would affect the observed apparent stable crack growth. Real reactor pressure vessels with growing flaws or with small leaks (as in vessel V-7) would experience essentially a constant load. Plans are to repeat the V-7 test in an effort to determine the effect of sustained loading in a thick-wall vessel. During the test, more detailed observations of crack extension will be made.

The following general conclusions have been drawn from the test of vessel V-7.

1. The test was performed under the conditions planned. Performance of the testing apparatus and data-acquisition equipment was satisfactory. Crack growth was successfully observed and measured ultrasonically.

2. Stable crack extension commenced at low pressure in the ligament region and progressed throughout the pressurization.

3. The vessel was pressurized to 147 MPa (21,350 psi) before the crack tore completely through the ligament. Pressure dropped abruptly at first but stabilized at about 129 MPa (18,700 psi).

4. Posttest measurements of the crack extension indicated an axial extension of about 20 mm (0.8 in.) (beyond each end).

5. The pretest analyses, which were based on prior tests of 1/7-scale steel models and which predicted the maximum test pressure within 3%, indicated that leakage would be preceded by local plastic instability and that leakage without burst was the expected (but not certain) mode of failure, because the lack of full restraint along the through-the-wall crack front elevated the effective fracture toughness. Test results confirmed these expectations.

6. The dependence of stable crack extension in the axial direction on level of loading has not been determined, nor has the influence of sustained loading on crack growth and stability been observed.

REFERENCE

1. R. W. Derby et al., *Test of 6-in.-thick Pressure Vessels. Series 1: Intermediate Test Vessels V-1 and V-2*, ORNL-4895 (February 1974.)

Appendices

Appendix A

Material Properties of the Prolongation of Vessel V-7

Properties of base metal of the prolongation of vessel V-7 were determined by W. J. Stelzman of the Metals and Ceramics Division of Oak Ridge National Laboratory and by T. R. Mager, S. E. Yanichko, and L. R. Singer of the Westinghouse Electric Corporation.*[1] This appendix provides the raw data obtained by Stelzman and shown previously in curve form in Chapter 2. All the Westinghouse data are presented in Chapter 2.

Stelzman tested precracked Charpy V-notch specimens taken from the prolongation of the vessel. The locations of the specimens in the prolongation are shown in Figs. A-1 through A-3, and orientations are as defined in Fig. 2.7. Table A-1 gives the data and fracture toughness values determined from these specimens. When these slow-bend tests were made, the specimen deflection was obtained from the crosshead motion; consequently, conservative (low-fracture toughness) values were deduced. These

*Work sponsored by the HSST program under UCCND Subcontract 3196 between Union Carbide Corporation and Westinghouse Electric Corporation.

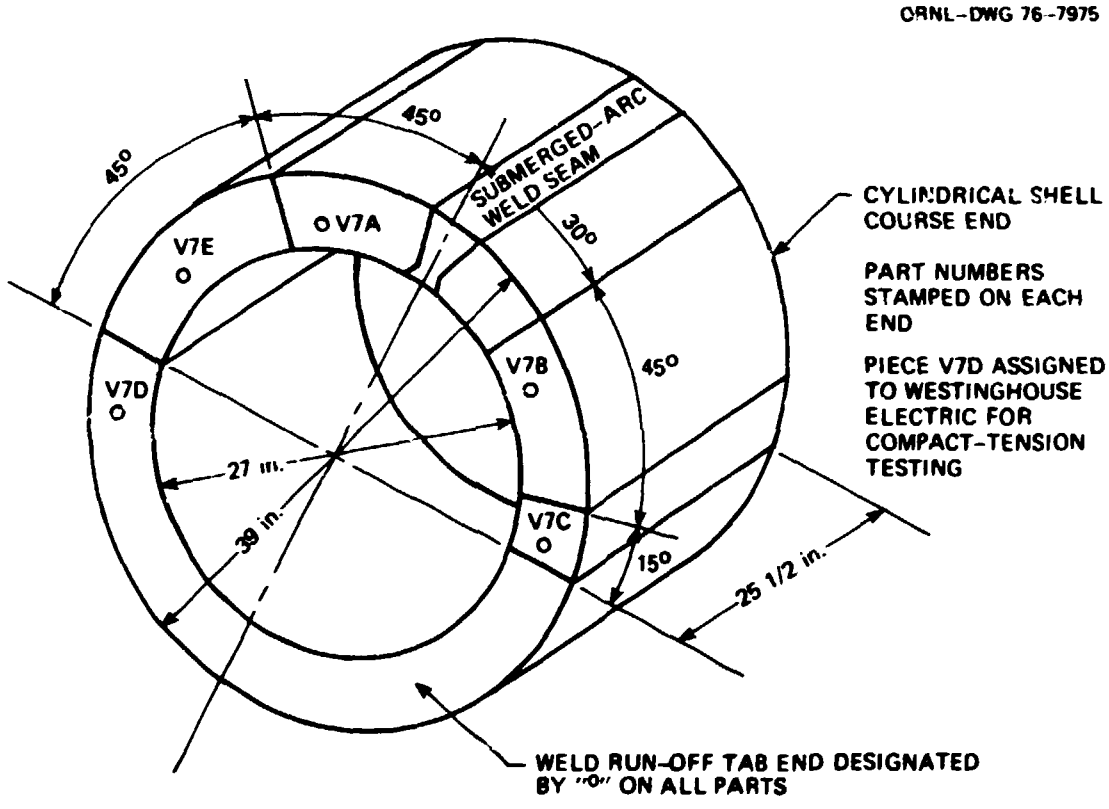

Fig. A-1. Cutting plan for prolongation of vessel V-7.

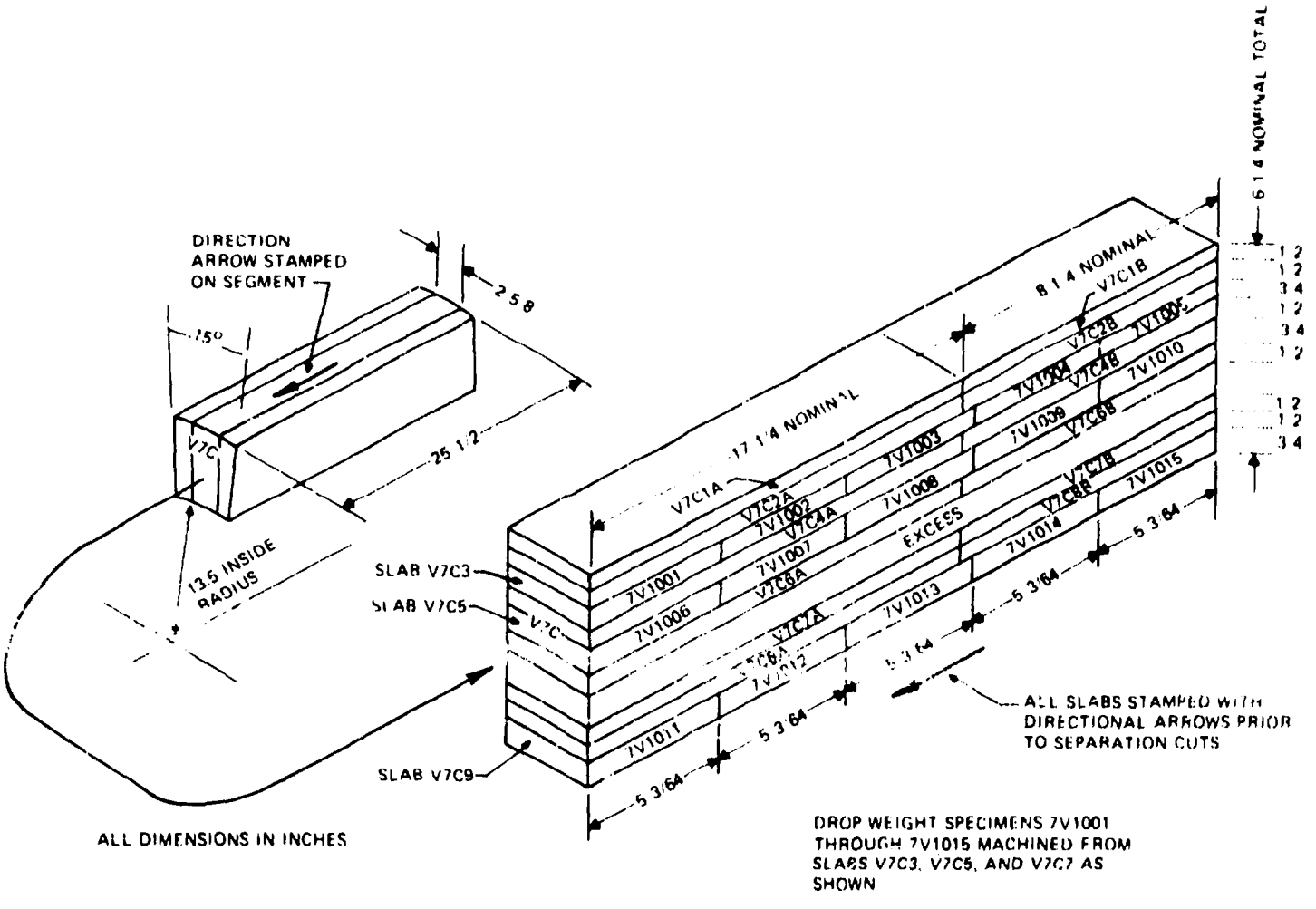

Fig. A-2. Cutting plan for segment V7C from prolongation of vessel V-7.

ORNL-DWG 76-7977

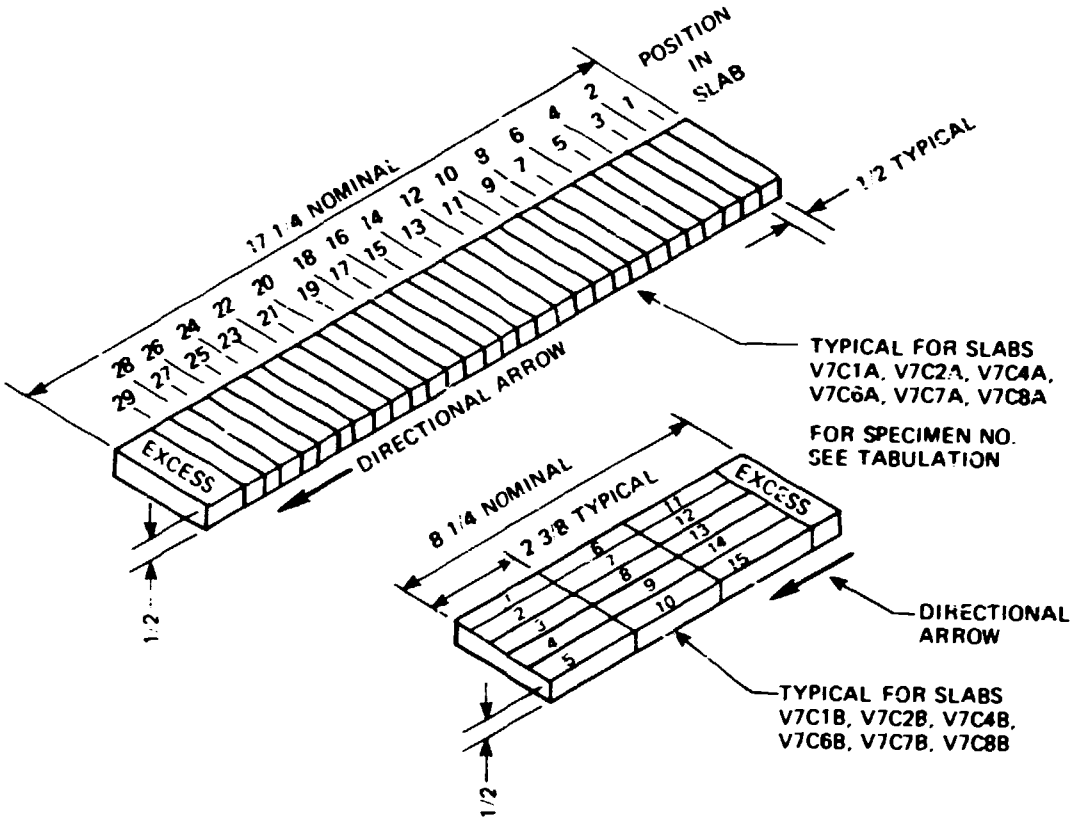

SPECIMEN TABULATION					
SPECIMEN TYPE	CHARPY	SUBSIZE TENSILE		CHARPY	SUBSIZE TENSILE
POSITION IN SLAB	1-27	28, 29		1-13	14, 15
SLAB NO.			SLAB NO.		
V7C1A	7V001-7V027	7V401, 7V402	V7C1B	7V028-7V040	7V403, 7V404
V7C2A	7V041-7V067	7V405, 7V406	V7C2B	7V068-7V080	7V407, 7V408
V7C4A	7V081-7V107	7V409, 7V410	V7C4B	7V108-7V120	7V411, 7V412
V7C6A	7V121-7V147	7V413, 7V414	V7C6B	7V148-7V160	7V415, 7V416
V7C7A	7V161-7V187	7V417, 7V418	V7C7B	7V188-7V200	7V419, 7V420
V7C8A	7V201-7V227	7V421, 7V422	V7C8B	7V228-7V240	7V423, 7V424

Fig. A-3. Cutting plan for Charpy and tensile specimens from segment V7C.

Table A-1. Fracture toughness of prolongation of vessel V-7 from slow bend (0.100 in./min) tests of pre-cracked Charpy V-notch specimens

Conversion factors: 1 in. = 25.4 mm; 1 lbf = 4.4482 N; 1 ksi $\sqrt{in}$ = 1.0988 MN·m$^{-3/2}$; 1 ft·lb = 1.3558 J; 1 lbf/in = 0.17513 N/mm

Specimen No	Depth[a]	Specimen orientation	Test temperature [°C (°F)]	Average crack data[b]				Load (lb)			Deflection (in.)		Energy (ft·lb)		Slope of linear load-displacement curve (10^6 lb/in.)	Lateral expansion (mils)	K_{Jrd} (ksi $\sqrt{in}$)	
				a (in.)	c (in.)	$\frac{a}{w}$	$f\left(\frac{a}{w}\right)$	Maximum	Start of fracture	Fracture arrest	Maximum load	Start of fracture	Maximum load	Start of fracture			From crosshead motion	From specimen deflection
7V-001	0.05	CA	93 3 (200)	0 2218	0 1717	0 564	3 31	1120			0 071		5.6		8.13	31	177	203
7V-002	0.05	CA	93 3 (200)	0 1909	0.2024	0.485	2 54	1470	1420	1350	0 060	0 084	6.1		9.60	32	154	175
7V-003	0.05	CA	54 4 (130)	0 1921	0.2014	0.488	2 56	1565			0 047		4.7		9.72	35	137	155
7V-004	0.05	CA	23 3 (74)	0 2385	0 1551	0.606	3 85	870			0 045		2.6		6 72	23	128	145
7V-005	0.05	CA	10.0 (50)	0 2073	0 1859	0 527	2 91	1220			0 044		3.6		8.88	21	131	148
7V-006	0.05	CA	17 8 (0)	0 2019	0 1915	0.513	2 77	1350			0 047		4 6		8.61	23	138	157
7V-007	0.05	CA	45 6 (50)	0 1838	0.2096	0.467	2 40	1655			0 051		5 7		9.60	25	141	160
7V-008	0.05	CA	87 2 (125)	0 1957	0 1978	0.497	2 64	1600	1540	235	0 045	0 075	6 0		9.66	13	160	183
7V-028	0.05	AC	93 3 (200)	0 1990	0 1944	0 506	2 71	1390			0 054		5 0		9 36	28	147	167
7V-029	0.05	AC	37 8 (100)	0 2049	0 1882	0 521	2 85	1300			0 052		4 5		8 88	25	143	163
7V-030	0.05	AC	10 0 (50)	0 2060	0 1873	0.524	2 88	1380			0 061		5 7		8.88	29	163	186
7V-031	0.05	AC	17 8 (0)	0 1972	0 1969	0 500	2 66	1530			0 060		6 1		8 82	29	154	175
7V-081	0.36	CA	93 3 (200)	0 2040	0 1893	0.519	2 83	1280			0 077		7 0		8.58	34	174	200
7V-082	0.36	CA	93 3 (200)	0 2065	0 1969	0 525	2 89	1240			0 075		6 4		8 70	34	171	196
7V-083	0.36	CA	54 4 (130)	0 1923	0 2012	0 489	2 57	1520			0 094		9 8		8.94	35	191	220
7V-084	0.36	CA	23 3 (74)	0 2119	0 1817	0 538	3 02	1200			0 074		7 5		8 76	35	194	223
7V-085	0.36	CA	10.0 (50)	0 2046	0 1886	0 520	2 84	1385			0 078		7 5		8 88	38	186	211
7V-086	0.36	CA	17 8 (0)	0 2015	0 1918	0 512	2 77	1440			0 074		7 3		9 12	31	179	205
7V-087	0.36	CA	45 6 (50)	0 1908	0 2024	0 485	2 54	1835	1080	230	0 075	0 175	8 2		9 60	29	179	205
7V-088	0 36	CA	87 2 (125)	0 1952	0 1978	0 497	2 64		1485	120		0 038		3 4	9 24	11	118	133
7V-108	0.36	AC	93 3 (200)	0 1922	0 2015	0 488	2 56	1400			0 060		5 7		9 30	30	148	169
7V-109	0.36	AC	37 8 (100)	0 2064	0 1843	0 528	2 92	1200			0 053		4 3		9.00	28	145	165
7V-110	0.36	AC	10 0 (50)	0 1989	0 1944	0 506	2 71	1420			0 061		5 7		9 66	28	159	182
7V-111	0.36	AC	17 8 (0)	0 2034	0 1899	0 517	2 81	1370	1280	480	0 068	0 133	6 3		8 82	27	166	190
7V-121	0.59	CA	93 3 (200)	0 2067	0 1868	0 525	2 89	1295			0 082		7 5		8 64	28	184	211
7V-122	0.59	CA	93 3 (200)	0 1901	0 2038	0 483	2 52	1525			0 090		9 7		9 90	38	195	225
7V-123	0.59	CA	54 4 (130)	0 2023	0 1907	0 515	2 79		1410	1335		0 093		9 0	9 00	41	199	229
7V-124	0.59	CA	23 3 (74)	0 2147	0 1788	0 546	3 10	1170			0 087		7 2		8 16	19	189	217
7V-125	0.59	CA	10 0 (50)	0 2349	0 1584	0 597	3 73	1060			0 082		6 0		7 32	13	196	226
7V-126	0.59	CA	17 8 (0)	0 2052	0 1879	0 522	2 86	1465			0 087		8 6		9 00	37	200	230
7V-127	0.59	CA	45 6 (50)	0 1977	0 1959	0 502	2 68	1590	1400	180	0 099	0 155	10 7		8 76	27	206	238
7V-128	0 59	CA	87 2 (125)	0 1849	0 2081	0 470	2 42		1270	30		0 014		0 8	9 81	5	54	57
7V-148	0.59	AC	93 3 (200)	0 1754	0 2142	0 456	2 33	1605			0 070		7 6		10 20	30	163	186
7V-149	0 59	AC	37 8 (100)	0 1842	0 2092	0 468	2 41	1540			0 069		7 0		10 20	34	162	185
7V-150	0.59	AC	10.0 (50)	0 2059	0 1872	0 524	2 88	1360			0 078		7 1		8 10	33	174	200
7V-151	0.59	AC	17 8 (0)	0 2059	0 1874	0 524	2 88	1305			0 073		6 5		8 22	34	167	191
7V-201	0.79	CA	93 3 (200)	0 1858	0 2063	0 475	2 46	1625			0 086		9 8		10 68	37	200	230
7V-202	0.79	CA	93 3 (200)	0 1989	0 1941	0 506	2 71		1490	1440		0 080		8 0	9 06	34	183	210
7V-203	0 79	CA	54 4 (130)	0 2020	0 1911	0 514	2 78	1420			0 080		7 8		8 76	36	182	209
7V-204	0.79	CA	23 3 (74)	0 2416	0 1515	0 615	4 00	895			0 076		4 7		6 42	28	[illegible]	201
7V-205	0.79	CA	10 0 (50)	0 1872	0 2060	0 476	2 47	1690			0 089		10 1		9 78	35	195	225
7V-206	0.79	CA	17 8 (0)	0 2026	0 1906	0 515	2 79	1460			0 083		8 1		8 52	35	184	211
7V-207	0.79	CA	45 6 (50)	0 1887	0 2046	0 480	2 50	1755	1540	90	0 087	0 154	10 0		9 36	27	192	221
7V-208	0.79	CA	87 2 (125)	0 1795	0 2136	0 457	2 33		1525	30		0 078		2 5	10 08	5	93	103
7V-228	0.79	AC	93 3 (200)	0 1952	0 1981	0 496	2 63		1410	1325		0 060		5 6	9 00	34	148	169
7V-229	0.79	AC	37 8 (100)	0 1829	0 2103	0 465	2 39	1650			0 073		8 1		9 66	41	168	192
7V-230	0.79	AC	10 0 (50)	0 1916	0 2007	0 488	2 56	1525			0 072		7 5		9 36	35	171	196
7V-231	0.79	AC	17 8 (0)	0 2078	0 1856	0 528	2 92	1360			0 075		6 8		8 16	34	172	197

Table A.1 (continued)

Specimen No.	Depth[a]	Specimen orientation	Test temperature [°C (°F)]	Average crack data[b] a (in.)	c (in.)	a/w	$f\left(\frac{a}{w}\right)$	Load (lb) Maximum	Load (lb) Start of fracture	Load (lb) Fracture arrest	Deflection (in.) Maximum load	Deflection (in.) Start of fracture	Energy (ft-lb) Maximum load	Energy (ft-lb) Start of fracture	Slope of linear load displacement curve (10^4 lb/in.)	Lateral expansion (mils)	K_{Id} (ksi $\sqrt{in.}$) From crosshead motion	K_{Id} (ksi $\sqrt{in.}$) From specimen deflection
7V-021	0.05	CA	93.3 (200)	0.2090	0.1833	0.534	2.98	1345			0.097		9.3		8.46	33	211	244
7V-036	0.05	AC	−45.6 (−50)	0.2245	0.1693	0.570	3.38	1140	1105	730	0.054	0.070	4.0		7.68	21	148	169
7V-037	0.05	AC	−73.3 (−100)	0.2116	0.1823	0.537	3.03	1300	1240	510	0.053	0.078	4.8		8.10	18	149	170
7V-116	0.36	AC	−45.6 (−50)	0.2196	0.1741	0.558	3.24		1190	125		0.064		5.2	7.86	20	163	186
7V-117	0.36	AC	−73.3 (−100)	0.1547	0.2382	0.394	1.95		1400	80		0.014		0.9	8.40	7	43	44
7V-156	0.59	AC	−45.6 (−50)	0.1830	0.2102	0.465	2.39	1785	1585	90	0.090	0.128	10.7		8.82	25	197	213
7V-157	0.59	AC	−73.3 (−100)	No crack					1650	0		0.106		24.8	12.18	19		
7V-236	0.79	AC	−45.6 (−50)	0.1367	0.2568	0.347	1.72	2430	2420	110	0.079	0.089	12.4		10.32	25	154	176
7V-237	0.79	AC	−73.3 (−100)	No crack					1880	0		0.119		29.6	11.82	22		
7V-241	0.93	CA	37.8 (100)	0.2018	0.1906	0.514	2.78	1440			0.090		8.9		7.56	37	182	209
7V-242	0.93	CA	[illegible] (0)	0.2095	0.1830	0.534	2.98	1380			0.080		7.7		8.10	40	188	216
7V-243	0.93	CA	51.7 (125)	0.2154	0.1782	0.547	3.11	1235			0.068		5.8		8.06	33	169	194
7V-244	0.93	CA	93.3 (200)	0.2085	0.1852	0.530	2.96	1345			0.087		8.3		8.94	30	201	232

[a] Fraction of wall thickness (6 in.) from outside.
[b] Dimension a is average of six measurements; c = w − a.

results were available at the time of the vessel tests. Subsequently, the system was changed so that specimen deflection is presently measured directly. By correlation of results obtained by both methods, data accumulated to date are sufficient to determine corrections for $K_{I,d}$ data up to 137 MN·m$^{-3/2}$ (125 ksi $\sqrt{\text{in.}}$). This correlation is shown in Fig. A-4. The adjusted values are included in the tabulation under the heading "From specimen deflection." It should be noted that deflections for the adjusted values are taken from the correlation, of which the portion above the data points shown is an assumed linear fit to the data.

The value of $K_{I,d}$ is calculated in accordance with the expression given in ASTM E-399-72 for bend specimens,[3] with the load P_Q being given the value P_{eq} prescribed by the equivalent-energy method.

$$P_{eq} = \sqrt{2kE_{max}} .$$

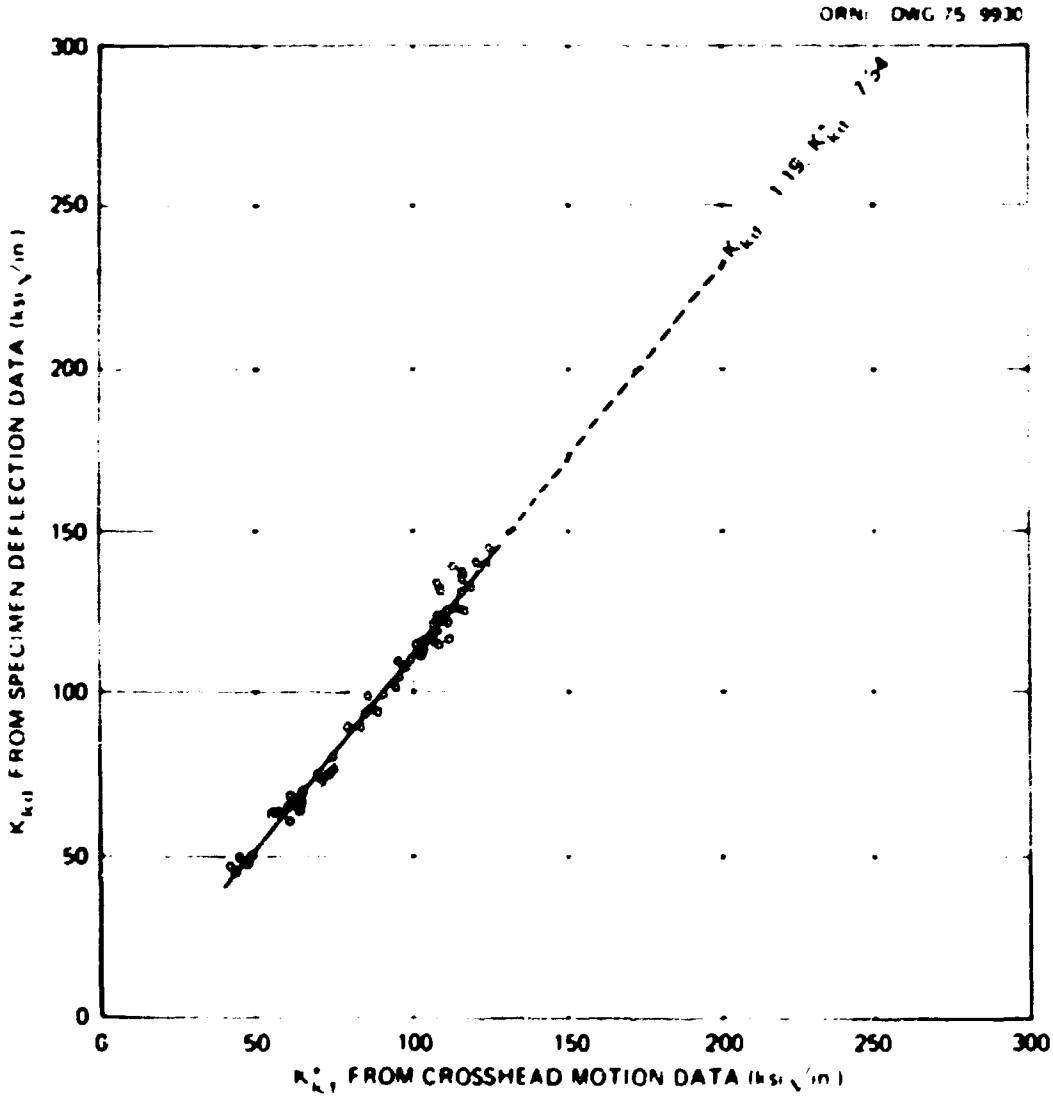

Fig. A-4. Comparison of static fracture toughness as computed from deflectometer measurements and crosshead motion.

where A is the slope of the linear portion of the load-deflection curve and E_{max} is the area under the curve up to maximum load. The dimensional parameters shown in Table A-1 are defined in ASTM E-399-72. The span length was 40 mm (1.575 in.) for all specimens, the width and thickness of the specimens were nominally 10 mm (0.394 in.), but actual measurements were used in calculating K_{Id}.

Stelzman's Charpy-impact, tensile properties, and dynamic fracture toughness measurements of the V-7 prolongation are given in Table A-2, A-3, and A-4 respectively. Locations of these specimens are also shown in the tables, and orientations are as defined in Fig. 2.7.

Table A-2. Charpy impact data from prolongation of vessel V-7

Conversion factors: 1 in. = 25.4 mm, 1 ft-lb = 1.3558 J, 1 mil = 0.0254 mm

Specimen No.	Depth[a]	Specimen orientation	Test temperature [°C (°F)]	Total energy (ft-lb)	Lateral expansion (mils)
7V-009	0.05	CA	93.3 (200)	95	79
7V-010	0.05	CA	37.8 (100)	123	[illegible]
7V-011	0.05	CA	10.0 (50)	123	81
7V-012	0.05	CA	17.8 (0)	130	93
7V-032	0.05	AC	93.3 (200)	72	64
7V-033	0.05	AC	37.8 (100)	70	58
7V-034	0.05	AC	10.0 (50)	55	46
7V-035	0.05	AC	17.8 (0)	35	27
7V-089	0.36	CA	93.3 (200)	118	78
7V-090	0.36	CA	37.9 (100)	115	82
7V-091	0.36	CA	10.0 (50)	93	67
7V-092	0.36	CA	17.8 (0)	69	52
7V-112	0.36	AC	93.3 (200)	57	55
7V-113	0.36	AC	37.8 (100)	63	56
7V-114	0.36	AC	10.0 (50)	50	46
7V-115	0.36	AC	17.8 (0)	30	29
7V-129	0.59	CA	93.3 (200)	137	88
7V-130	0.59	CA	37.8 (100)	130	85
7V-131	0.59	CA	10.0 (50)	114	80
7V-132	0.59	CA	17.8 (0)	51	39
7V-152	0.59	AC	93.3 (200)	86	70
7V-153	0.59	AC	37.8 (100)	75	63
7V-154	0.59	AC	10.0 (50)	51	50
7V-155	0.59	AC	17.8 (0)	39	30
7V-209	0.79	CA	93.3 (200)	138	89
7V-210	0.79	CA	37.8 (100)	140	89
7V-211	0.79	CA	10.0 (50)	100	69
7V-212	0.79	CA	17.8 (0)	99	72
7V-232	0.79	AC	93.3 (200)	85	68
7V-233	0.79	AC	37.8 (100)	91	69
7V-234	0.79	AC	10.0 (50)	65	53
7V-235	0.79	AC	-17.8 (0)	48	46
7V-017	0.05	CA	148.9 (300)	147	83
7V-018	0.05	CA	45.6 (50)	116	72
7V-019	0.05	CA	73.3 (100)	73	49
7V-020	0.05	CA	93.3 (200)	145	87
7V-097	0.36	CA	148.9 (300)	122	87
7V-098	0.36	CA	45.6 (50)	30	19
7V-099	0.36	CA	73.3 (100)	11	0
7V-137	0.59	CA	148.9 (300)	146	84
7V-138	0.59	CA	-45.6 (50)	43	30
7V-139	0.59	CA	-73.3 (100)	15	8
7V-217	0.79	CA	148.9 (300)	143	84
7V-218	0.79	CA	-45.6 (50)	58	41
7V-219	0.79	CA	73.3 (100)	27	15

[a] Fraction of wall thickness (6 in.) from outside.

Table A-3. Base metal tensile properties from the prolongation of vessel V-7 from subsize tensile specimens

Conversion factor 10^3 psi = 6.8948 MPa

Specimen No.	Orientation	Depth[a]	Test temperature [°C (°F)]	Lower yield ($\times 10^3$ psi)	Ultimate ($\times 10^3$ psi)	Total elongation in 31.75 mm (1.250 in.) (%)	Reduction in area (%)
7V-401	CA	0.05	93.3 (200)	74.0	89.8	17.6	71.6
7V-402	CA	0.05	93.3 (200)	73.8	90.2	17.7	75.7
7V-403	AC	0.05	93.3 (200)	71.0	89.2	15.3	67.5
7V-404	AC	0.05	93.3 (200)	73.2	90.4	17.3	67.1
7V-405	CA	0.14	93.3 (200)	62.7	82.3	16.8	73.8
7V-406	CA	0.14	93.3 (200)	63.3	82.8	17.5	71.8
7V-409	CA	0.36	93.3 (200)	63.3	83.2	18.2	72.3
7V-410	CA	0.36	93.3 (200)	63.6	83.6	18.4	71.0
7V-411	AC	0.36	93.3 (200)	64.2	84.0	14.4	55.5
7V-412	AC	0.36	93.3 (200)	63.8	84.3	15.2	61.7
7V-413	CA	0.59	93.3 (200)	62.2	82.3	17.1	73.3
7V-414	CA	0.59	93.3 (200)	63.8	84.1	16.9	73.0
7V-415	AC	0.59	93.3 (200)	63.4	83.3	16.4	59.2
7V-416	AC	0.59	93.3 (200)	63.4	83.6	16.0	65.3
7V-421	CA	0.79	93.3 (200)	63.2	83.3	18.2	70.7
7V-422	CA	0.79	93.3 (200)	62.6	82.9	17.8	74.4
7V-423	AC	0.79	93.3 (200)	62.8	82.8	17.8	68.3
7V-424	AC	0.79	93.3 (200)	63.6	83.3	17.4	66.8
7V-417	CA	0.70	25.0 (77)	65.8	86.5	22.6	73.4
7V-419	AC	0.70	25.0 (77)	66.0	88.1	18.3	69.4
7V-407	AC	0.14	93.3 (200)	59.1	83.2	16.4	67.0
7V-425	CA	0.93	93.3 (200)	75.3	90.7	17.8	76.8
7V-426	CA	0.93	93.3 (200)	74.5	89.7	18.1	76.2

[a]Fraction of wall thickness [152.4 mm (6 in.)] from outside

Table A-4. Fracture toughness of prolongation of vessel V-7 from dynamic test of precracked Charpy V-notch specimens, CA orientation

Conversion factors: 1 in. = 25.4 mm; 1 lbf = 4.4482 N; 1 ksi$\sqrt{\text{in.}}$ = 1.0988 MN·m$^{-3/2}$; 1 ft-lb = 1.3558 J; 1 lbf/in. = 0.17513 N/mm

Specimen No.	Depth[a]	Test temperature [°C (°F)]	Total energy (ft-lb)	Average crack data (in.)				Load (lb)			Deflection (in.)		Energy (ft-lb)		Slope of linear load-displacement curve (10^6 lb/in.)	Lateral expansion (mils)	K_{Jd} (ksi$\sqrt{\text{in.}}$)
				a	c	$\frac{a}{w}$	$f\left(\frac{a}{w}\right)$	Maximum	Start of fast fracture	Fracture arrest	Maximum load	Start of fast fracture	Maximum load	Start of fast fracture			
7V-013	0.05	93.3 (200)	55	0.1936	0.2000	0.492	2.60	1745			0.106		12.0		7.99	54	202
7V-014	0.05	37.8 (100)	54	0.1928	0.2013	0.489	2.57	1820			0.106		13.1		6.42	52	187
7V-015	0.05	10.0 (50)	42	0.2160	0.1783	0.548	3.13	1505			0.082		8.4		9.34	45	220
7V-016	0.05	17.8 (0)	47	0.2039	0.1901	0.518	2.82	1745			0.060		6.4		9.39	46	173
7V-093	0.36	93.3 (200)	47	0.1919	0.2015	0.486	2.56	1720			0.130		15.3		7.55	50	218
7V-094	0.36	37.8 (100)	47	0.1986	0.1958	0.504	2.69	1695			0.083		9.2		9.87	52	203
7V-095	0.36	10.0 (50)	32	0.2013	0.1929	0.511	2.76		1265	915		0.014		1.0	12.56	30	77
7V-096	0.36	17.8 (0)	8	0.1983	0.1958	0.503	2.68		1130	315		0.012		0.7	12.72	12	63
7V-133	0.59	93.3 (200)	61	0.1839	0.2094	0.468	2.41	1795			0.105		13.0		12.72	53	246
7V-134	0.59	37.8 (100)	49	0.2054	0.1888	0.521	2.85	1530			0.104		11.2		11.98	49	261
7V-135	0.59	10.0 (50)	23	0.2129	0.1809	0.541	3.05		1320	665		0.052		4.2	8.03	25	141
7V-136	0.59	17.8 (0)	14	0.1909	0.2034	0.484	2.53		1161	610		0.013		0.9	13.06	20	69
7V-213	0.79	93.3 (200)	55	0.1973	0.1959	0.502	2.68	1605			0.107		10.8		8.13	51	199
7V-214	0.79	37.8 (100)	51	0.1932	0.2008	0.490	2.58	1795			0.131		16.2		6.80	51	215
7V-215	0.79	10.0 (50)	35	0.2059	0.1885	0.522	2.86									36	
7V-216	0.79	17.8 (0)	15	0.1893	0.2050	0.480	2.50		1050	465		0.015		0.8	8.36	16	51

[a]Fraction of wall thickness (6 in.) from outside

REFERENCES

1. T. R. Mager, S. E. Yanichko, and L. R. Singer, *Fracture Toughness Characterization of HSST Intermediate Pressure Vessel Material*, WCAP-8456 (December 1974).

2. ASTM E-399-72, "Method of Test for Plane-Strain Fracture Toughness of Metallic Materials," *ASTM Standards*, Part 31, 1973.

Appendix B

Intermediate Vessel V-7 Test Data

Table B-1. Pressure-stream data from V

Stream (psia, at) at pre
(channel No. press

1000	2000	3000	4000	5000	6000	7000	8000
17 -.5501701E+02	17 -.1000139E+03	17 -.1515950E+03	17 -.1856824E+03	17 .2338223E+03	17 .3301021E+03	17 .4332598E+03	17 .5776787E+0
16 -.8596409E+02	16 -.1616325E+03	16 -.2476012E+03	16 -.3232250E+03	16 .4091891E+03	16 .4985917E+03	16 .6223800E+03	16 .7983082E+0
21 -.7564840E+02	21 -.1444125E+03	21 -.2235035E+03	21 -.2819622E+03	21 .3576106E+03	21 .4298294E+03	21 .5226616E+03	21 .6980284E+0
22 -.9627978E+02	22 -.1554597E+03	22 -.2207958E+03	22 -.2957164E+03	22 .3816805E+03	22 .4676446E+03	22 .5604858E+03	22 .6602042E+0
89 +.2195226E+01	89 +.2195226E+01	89 +.2195070E+01	89 +.2194757E+01	89 +.2194757E+01	89 +.2194757E+01	89 +.2194757E+01	89 +.2194757E+0
91 -.6149214E+02	91 -.1198308E+03	91 -.1828997E+03	91 -.2428151E+03	91 .3090374E+03	91 .3691471E+03	91 .4[illegible]24768E+03	91 .4903604E+0
80 -.6464558E+02	80 -.1245610E+03	80 .1892965E+03	80 .2506987E+03	80 .3184977E+03	80 .3805895E+03	80 .4408794E+03	80 .5045504E+0
82 -.6149214E+02	82 -.1182541E+03	82 -.1828997E+03	82 .2412384E+03	82 .3058840E+03	82 .3681071E+03	82 .4285580E+03	82 .4872068E+0
59 -.8653073E+02	59 -.1636217E+03	59 .2501525E+03	59 -.3319633E+03	59 .4184941E+03	59 .5003049E+03	59 .5811779E+03	59 .6623534E+0
60 -.1211430E+03	60 -.2296997E+03	60 .3508427E+03	60 .4641193E+03	60 .5884989E+03	60 .7048327E+03	60 .8223108E+03	60 .9408250E+0
87 +.2185684E+01	87 +.2185226E+01	87 +.2184757E+01	87 +.2184288E+01	87 +.2184132E+01	87 +.2183976E+01	87 +.2183976E+01	87 +.2183976E+0
90 +.2213664E+01	90 +.2213508E+01	90 +.2213039E+01	90 +.2213039E+01	90 +.2212883E+01	90 +.2212883E-01	90 +.2212883E+01	90 +.2213039E+0
8 -.1237882E+03	8 -.2371793E+03	8 -.3575354E+03	8 .4607675E+03	8 .5811172E+03	8 .6877127E+03	8 .7805539E+03	8 .8802723E+0
9 -.1306654E+03	9 -.2269547E+03	9 -.3438720E+03	9 .4470132E+03	9 .5638244E+03	9 .6739584E+03	9 .7943082E+03	9 +.1127[illegible]2E+0
10 -.6189414E+02	10 -.1168959E+03	10 -.1787933E+03	10 .2303838E+03	10 .2854008E+03	10 .3438563E+03	10 .3954348E+03	10 .4[illegible]E+0
11 -.1169111E+03	11 -.2204084E+03	11 .3442032E+03	11 .4504518E+03	11 .5742401E+03	11 .6842741E+03	11 .8011853E+03	11 .9180964E+0
12 -.1134726E+03	12 -.1857594E+03	12 -.2854830E+03	12 .3782420E+03	12 .4779603E+03	12 .5776787E+03	12 .6877127E+03	12 .7986096E+0
13 -.1031569E+03	13 -.2027134E+03	13 -.3024370E+03	13 -.3851191E+03	13 .4813989E+03	13 .5742401E+03	13 .6739584E+03	13 .7771154E+0
15 -.1031569E+02	15 -.2750492E+02	15 -.3094366E+02	15 -.3438563E+02	15 .4126276E+02	15 .4813989E+02	15 .5501701E+02	15 .6845558E+0
18 +.6877127E+02	18 +.1065682E+03	18 +.1581493E+03	18 +.2166295E+03	18 +.2716465E+03	18 +.3301021E+03	18 +.3713648E+03	18 +.4160662E+0
20 +.5845558E+02	20 -.3481384E+05	20 -.3522993E+05	20 .3525903E+05	20 .3524528E+05	20 .3520401E+05	20 .3515587E+05	20 .3509398E+0
23 -.1719282E+02	23 -.3802063E+02	23 .5521434E+02	23 -.6533271E+02	23 .7564840E+02	23 .8940265E+02	23 .1100340E+03	23 .1203497E+0
24 -.9284121E+02	24 -.1754332E+03	24 -.2682792E+03	24 .3472949E+03	24 .4401361E+03	24 .5295388E+03	24 .6292571E+03	24 .7289755E+0
25 -.1237882E+03	25 -.2370862E+03	25 -.3471260E+03	25 .4470132E+03	25 .5570473E+03	25 .6602042E+03	25 .7736768E+03	25 .8802723E+0
26 -.1272268E+03	26 -.2443312E+03	26 -.3646872E+03	26 .4676446E+03	26 .5845558E+03	26 .6911513E+03	26 .8046239E+03	26 .9112193E+0
27 -.1272268E+03	27 -.2304418E+03	27 -.3473559E+03	27 .4538903E+03	27 .5708015E+03	27 .6773970E+03	27 .7908696E+03	27 .9009037E+0
28 -.5501701E+02	28 -.1169878E+03	28 -.1720077E+03	28 .2235066E+03	28 .2750850E+03	28 .3301021E+03	28 .3851191E+03	28 .4435747E+0
29 -.1203497E+03	29 -.2270856E+03	29 -.3440029E+03	29 .4470132E+03	29 .5570473E+03	29 .6670813E+03	29 .7736768E+03	29 .8768337E+0
30 -.1547353E+03	30 -.2939312E+03	30 .4538327E+03	30 .5983101E+03	30 .7530454E+03	30 .8940275E+03	30 .1031569E+04	30 .1163954E+0
31 -.1564546E+03	31 -.2891466E+03	31 -.4404513E+03	31 .5811172E+03	31 .7289755E+03	31 .8630794E+03	31 .9954642E+03	31 .1126129E+0
32 -.1289461E+03	32 -.2476835E+03	32 -.3766365E+03	32 .4968724E+03	32 .6275379E+03	32 .7461683E+03	32 .8647987E+03	32 .9799986E+0
33 -.1289461E+03	33 -.2510322E+03	33 -.3817044E+03	33 .5037496E+03	33 .6326957E+03	33 .7530454E+03	33 .8716759E+03	33 .9885870E+0
34 -.1375425E+03	34 -.2613129E+03	34 -.3971432E+03	34 .5243809E+03	34 .6619235E+03	34 .7891503E+03	34 .9163772E+03	34 .1043604E+0
35 -.1684896E+03	35 -.3113240E+03	35 -.4437156E+03	35 .5811172E+03	35 .7289755E+03	35 .8630794E+03	35 .9937449E+03	35 .1119253E+0
36 -.1564546E+03	36 -.2940611E+03	36 -.4470852E+03	36 .5879943E+03	36 .7392911E+03	36 .8751145E+03	36 .1007499E+04	36 .1136445E+0
37 -.6877127E+01	37 -.3095775E+02	37 -.5159021E+02	37 -.7392911E+02	37 .9627978E+02	37 .1186304E+03	37 .1375425E+03	37 .1564546E+0
39 -.3283828E+03	39 -.4568774E+03	39 -.6064627E+03	39 -.7444490E+03	39 .9026729E+03	39 .9576399E+03	39 .1005780E+04	39 .1052200E+0
40 -.1366720E+03	40 -.2494263E+03	40 -.3741395E+03	40 .4903107E+03	40 .6150239E+03	40 .7294867E+03	40 .8438874E+03	40 .9560738E+0
41 -.8541998E+01	41 -.3929319E+02	41 .7175279E+02	41 .1007956E+03	41 .1298384E+03	41 .1588811E+03	41 .1845461E+03	41 .2118415E+0
43 -.1264216E+03	43 -.2340508E+03	43 -.3519303E+03	43 .4629763E+03	43 .5842727E+03	43 .6970270E+03	43 .8113059E+03	43 .9242442E+0
44 -.3416799E+02	44 -.6833599E+02	44 -.1007956E+03	44 -.1332551E+03	44 .1640064E+03	44 .1930491E+03	44 .2168994E+03	44 .2408843E+0
58 -.1573286E+02	58 -.2202600E+02	58 -.3775887E+02	58 -.4719858E+02	58 .6293144E+02	58 .7866430E+02	58 .9326612E+02	58 .1069834E+0
63 -.7551773E+02	63 -.1321560E+03	63 -.2076737E+03	63 -.2706051E+03	63 .3461229E+03	63 .4122009E+03	63 .4811934E+03	63 .5475035E+0
64 -.1573286E+02	64 -.2517257E+02	64 -.4405201E+02	64 -.5653839E+02	64 .7551773E+02	64 .9754373E+02	64 .1154930E+03	64 .1321560E+0
65 -.6607801E+02	65 -.1132766E+03	65 -.1825011E+03	65 -.2328463E+03	65 .2989243E+03	65 .3555626E+03	65 .4140116E+03	65 .4719858E+0
66 -.3461229E+02	66 -.6765130E+02	66 -.1022636E+03	66 -.1353026E+03	66 .1714882E+03	66 .2045271E+03	66 .2388340E+03	66 .2721784E+0
68 -.5349172E+02	68 -.1022636E+03	68 -.1573286E+03	68 -.2076737E+03	68 .2643120E+03	68 .3162305E+03	68 .3675410E+03	68 .4216406E+0
70 -.5978487E+02	70 -.1117033E+03	70 -.1714882E+03	70 -.2281264E+03	70 .2879113E+03	70 .3461229E+03	70 .4018335E+03	70 .4593995E+0
71 -.6135815E+02	71 -.1179964E+03	71 -.1809279E+03	71 -.2407127E+03	71 -.3036442E+03	71 .3634290E+03	71 .4229572E+03	71 .4829988E+0
72 -.5360853E+02	72 -.1040636E+03	72 -.1576721E+03	72 -.2081272E+03	72 -.2648892E+03	72 .3169100E+03	72 .3689612E+03	72 .4209846E+0
73 -.3311116E+02	73 -.6622231E+02	73 -.1009101E+03	73 -.1340213E+03	73 -.1702859E+03	73 .2041223E+03	73 .2357815E+03	73 .2696194E+0
74 -.5991542E+02	74 -.1151006E+03	74 -.1765928E+03	74 -.2333548E+03	74 .2980003E+03	74 .3575655E+03	74 .4134487E+03	74 .4714397E+0
75 -.5833870E+02	75 -.1135239E+03	75 -.1718626E+03	75 -.2270479E+03	75 -.2885400E+03	75 -.3463906E+03	75 -.4009730E+03	75 .4572492E+0
76 -.1734393E+02	76 -.3784132E+02	76 -.5676198E+02	76 -.7725936E+02	76 -.9775674E+02	76 .1185274E+03	76 .1369006E+03	76 .1560954E+0
77 +.4730165E+01	77 +.1892066E+02	77 +.2049738E+02	77 +.2049738E+02	77 +.2049738E+02	77 +.2218509E+02	77 +.1781033E+02	77 +.2049738E+0
78 +.4730165E+01	78 +.1892066E+02	78 +.2049738E+C2	78 +.2049738E+02	78 +.2049738E+02	78 +.2318509E+02	78 +.1781033E+02	78 +.2049738E+0
84 -.1892066E+02	84 -.4257148E+02	84 -.6622231E+02	84 -.8829641E+02	84 -.1151006E+03	84 .1387854E+03	84 .1607906E+03	84 .1860531E+0
85 -.5833870E+02	85 -.1103705E+03	85 -.1702859E+03	85 -.2254711E+03	85 -.2853866E+03	85 .3421856E+03	85 .3988705E+03	85 .4540959E+0
86 -.5676198E+02	86 -.1072170E+03	86 -.1624023E+03	86 -.2160108E+03	86 -.2727728E+03	86 .3268840E+03	86 .3779081E+03	86 .4320217E+0

BLANK PAGE

lata from V-7 Test – computer output

n/m) at pressure (psi) –
el No. precedes strain)

8000		9000		10,000		11,000		12,000		13,000		14,000		15,000
776787E+03	17	.7633611E+03	17	.1055639E+04	17	.1447269E+04	17	.1943180E+04	17	.2531205E+04	17	.3597864E+04	17	.4040312E+04
943082E+03	16	.9112193E+03	16	.1038446E+04	16	.1196546E+04	16	.1392703E+04	16	.1602466E+04	16	.1815561E+04	16	.2111278E+04
980284E+03	21	.8733952E+03	21	.1010938E+04	21	.1148435E+04	21	.1306707E+04	21	.1478645E+04	21	.1633318E+04	21	.1815561E+04
602042E+03	22	-.7633611E+03	22	.9490435E+03	22	.1175211E+04	22	.1352142E+04	22	.1496569E+04	22	.1640195E+04	22	.1777737E+04
194757E+01	89	+.2194913E+01	89	+.2195070E+01	89	+.2195382E+01	89	+.2173975E+01	89	+.2145537E+01	89	+.2110692E+01	89	+.2067253E+01
903604E+03	91	.5437657E+03	91	.6005247E+03	91	.6588603E+03	91	.7174083E+03	91	.7710169E+03	91	.8230487E+03	91	.8735038E+03
045509E+03	80	.5591273E+03	80	.6190397E+03	80	.6773753E+03	80	.7394824E+03	80	.7946677E+03	80	.8482762E+03	80	.9003080E+03
872069E+03	82	.5400760E+03	82	.5984117E+03	82	.6551707E+03	82	.7158316E+03	82	.7678634E+03	82	.8198952E+03	82	.8719271E+03
623534E+03	59	.7347245E+03	59	.8133888E+03	59	.8895280E+03	59	.9675709E+03	59	.1039942E+04	59	.1107593E+04	59	.1173671E+04
408250E+03	60	.1046235E+04	60	.1161085E+04	60	.1273819E+04	60	.1386065E+04	60	.1486755E+04	60	.1596885E+04	60	.1902102E+04
183976E+01	87	+.2183976E+01	87	+.2184132E+01	87	+.2184132E+01	87	+.2184288E+01	87	+.2184600E+01	87	+.2185069E+01	87	+.2185694E+01
213039E+01	90	+.2212883E+01	90	+.2212883E+01	90	+.2203976E+01	90	+.2188351E+01	90	+.2169913E+01	90	+.2146474E+01	90	+.2115087E+01
802723E+03	8	.9731135E+03	8	.1072832E+04	8	.1176021E+04	8	.1285996E+04	8	.1402913E+04	8	.1533599E+04	8	.1715843E+04
127092E+06	9	+.1127126E+06	9	+.1127126E+06	9	+.1127068E+06	9	+.1127185E+06	9	+.1127151E+06	9	+.1127126E+06	9	+.1127126E+06
263818E+03	10	.4779603E+03	10	.5398545E+03	10	.6086153E+03	10	.6842885E+03	10	.7805733E+03	10	.9112193E+03	10	.1145042E+04
180964E+03	11	.1024692E+04	11	.1141603E+04	11	.1271873E+04	11	.1420530E+04	11	.1609660E+04	11	.1867140E+04	11	.2080331E+04
906696E+03	12	.8905879E+03	12	.1007499E+04	12	.1134599E+04	12	.1299912E+04	12	-.1537185E+04	12	.1729598E+04	12	.1846508E+04
771154E+03	13	.8768337E+03	13	.1000622E+04	13	.1162346E+04	13	.1399396E+04	13	-.1567894E+04	13	.1708966E+04	13	.1849947E+04
845558E+02	15	.5501701E+02	15	.3094707E+02	15	+.9970811E+02	15	+.2028908E+03	15	+.3026144E+03	15	+.4126276E+03	15	+.5467316E+03
160662E+03	18	+.4745218E+03	18	+.5398545E+03	18	+.6120652E+03	18	+.6877157E+03	18	+.1133891E+06	18	+.1133866E+06	18	+.1133866E+06
509398E+05	20	.3502177E+05	20	.3493924E+05	20	.3484457E+05	20	.3475194E+05	20	.3461096E+05	20	.3447504E+05	20	.3432030E+05
203497E+03	23	.1409811E+03	23	.1409811E+03	23	.2043592E+02	23	+.9609035E+02	23	+.2130076E+03	23	+.3335406E+03	23	+.4745218E+03
289755E+03	24	.8218167E+03	24	.9352093E+03	24	.1079595E+04	24	.1299902E+04	24	.1482155E+04	24	.1612686E+04	24	.1750229E+04
802723E+03	25	.9799906E+03	25	.1093463E+04	25	.1217375E+04	25	.1368433E+04	25	.1581634E+04	25	.1784614E+04	25	.1935911E+04
112193E+03	26	.1010938E+04	26	.1124419E+04	26	.1244515E+04	26	.1385993E+04	26	.1561369E+04	26	.1788053E+04	26	.2052822E+04
009037E+03	27	.1000622E+04	27	-.1107217E+04	27	.1220580E+04	27	.1344594E+04	27	.1485583E+04	27	.1657388E+04	27	.1904964E+04
435747E+03	28	.4917145E+03	28	.5536087E+03	28	.6154002E+03	28	.6912579E+03	28	.7806652E+03	28	.8940265E+03	28	.1100340E+04
768337E+03	29	.9662364E+03	29	.1065955E+04	29	.1168922E+04	29	.1279341E+04	29	.1399697E+04	29	.1526722E+04	29	.1691773E+04
163954E+04	30	.1279146E+04	30	.1402934E+04	30	.1519847E+04	30	.1640199E+04	30	.1748519E+04	30	.1853386E+04	30	.1956542E+04
126129E+04	31	.1200059E+04	31	.1316969E+04	31	.1436952E+04	31	.1563201E+04	31	.1685276E+04	31	.1808684E+04	31	.1937630E+04
799906E+03	32	.1083147E+04	32	.1196620E+04	32	.1308211E+04	32	.1425453E+04	32	.1535931E+04	32	.1652230E+04	32	.1770860E+04
885870E+03	33	.1093463E+04	33	.1206936E+04	33	.1320335E+04	33	.1437398E+04	33	.1552596E+04	33	.1669422E+04	33	.1791492E+04
043604E+04	34	-.1157076E+04	34	-.1279146E+04	34	.1402892E+04	34	.1530209E+04	34	.1655723E+04	34	.1784614E+04	34	.1916999E+04
119253E+04	35	.1232725E+04	35	.1349636E+04	35	.1462914E+04	35	.1575062E+04	35	.1674786E+04	35	.1772579E+04	35	.1867140E+04
136445E+04	36	.1248198E+04	36	.1368588E+04	36	.1487053E+04	36	.1611099E+04	36	.1729736E+04	36	.1849947E+04	36	.1972016E+04
564546E+03	37	.1753667E+03	37	-.1925595E+03	37	.2131707E+03	37	.2338436E+03	37	.2527567E+03	37	.2699272E+03	37	.2871201E+03
052200E+04	39	.1090024E+04	39	.1131287E+04	39	.1171244E+04	39	.1197926E+04	39	.1228875E+04	39	.1255075E+04	39	.1282584E+04
567038E+03	40	.1057499E+04	40	.1165128E+04	40	.1270965E+04	40	.1382095E+04	40	.1488016E+04	40	.1595645E+04	40	.1704983E+04
118415E+03	41	.2340508E+03	41	.2596767E+03	41	.2819198E+03	41	.3075119E+03	41	.3297211E+03	41	.3519303E+03	41	.3758479E+03
242442E+03	43	.1023331E+04	43	.1132669E+04	43	.1243509E+04	43	.1358178E+04	43	.1469224E+04	43	.1581978E+04	43	.1699857E+04
408843E+03	44	.2579683E+03	44	.2784691E+03	44	.2954817E+03	44	.3160539E+03	44	.3314295E+03	44	.3485135E+03	44	.3638891E+03
069834E+03	58	.1195697E+03	58	.1384491E+03	58	.1561943E+03	58	.1793546E+03	58	.2171134E+03	58	.2706052E+03	58	.3587092E+03
475035E+03	63	.6072884E+03	63	.6702198E+03	63	.7329061E+03	63	.7960827E+03	63	.8527210E+03	63	.9062127E+03	63	.9659976E+03
321560E+03	64	.1510354E+03	64	.1699149E+03	64	.1941532E+03	64	.2265532E+03	64	.2611654E+03	64	.3178038E+03	64	.4027612E+03
719858E+03	65	.5191844E+03	65	.5726761E+03	65	.6248210E+03	65	.6765130E+03	65	.7205650E+03	65	.7614704E+03	65	.7960827E+03
721784E+03	66	.3004976E+03	66	.3319033E+03	66	.3631171E+03	66	.3964681E+03	66	.4247872E+03	66	.4562529E+03	66	.4861454E+03
216406E+03	68	.4672659E+03	68	.5176111E+03	68	.5673379E+03	68	.6183014E+03	68	.6654999E+03	68	.7095519E+03	68	.7520307E+03
593995E+03	70	.5097447E+03	70	.5648096E+03	70	.6189357E+03	70	.6765130E+03	70	.7284314E+03	70	.7787765E+03	70	.8275484E+03
829988E+03	71	.5349172E+03	71	.5915555E+03	71	.6510718E+03	71	.7079787E+03	71	-.7614704E+03	71	.8133888E+03	71	.8637340E+03
209846E+03	72	.4667128E+03	72	.5171653E+03	72	.5644645E+03	72	.6149214E+03	72	.6606463E+03	72	.7063713E+03	72	.7473660E+03
596194E+03	73	.2972705E+03	73	.3303799E+03	73	.3603360E+03	73	.3941804E+03	73	.4241381E+03	73	.4556725E+03	73	.4856303E+03
714397E+03	74	.5206602E+03	74	.5758426E+03	74	.6294484E+03	74	.6858739E+03	74	.7363290E+03	74	.7852073E+03	74	.8325090E+03
572492E+03	75	.5050312E+03	75	.5602136E+03	75	.6122427E+03	75	.6653765E+03	75	.7142549E+03	75	.7631333E+03	75	.8072814E+03
560954E+03	76	.1715866E+03	76	.1889297E+03	76	.2062727E+03	76	.2254711E+03	76	.2412384E+03	76	.2570056E+03	76	.2680426E+03
049738E+02	77	+.1781033E+02	77	+.1781033E+02	77	+.1781033E+02	77	+.1892066E+02	77	+.1892066E+02	77	+.1892066E+02	77	+.1892066E+02
049738E+02	78	+.1781033E+02	78	+.1781033E+02	78	+.1781033E+02	78	+.2893066E+02	78	+.1892066E+02	78	+.1892066E+02	78	+.1892066E+02
860531E+03	84	.2065131E+03	84	.2285861E+03	84	.2522357E+03	84	.2759262E+03	84	.2964236E+03	84	.3169210E+03	84	.3342649E+03
840959E+03	85	-.5029287E+03	85	.5565345E+03	85	.6101403E+03	85	.6637998E+03	85	.7126782E+03	85	.7615565E+03	85	.8072814E+03
320217E+03	86	.4772364E+03	86	.5276889E+03	86	.5781413E+03	86	.6291119E+03	86	.6748368E+03	86	.7205618E+03	86	.7631333E+03

Table B-1 (co

	Strain (μm/m) at (channel No.							
16.000	17.000	18.000	18.500	19.000	19.500	20.000	~20
17 -.5316587E+04	17 .7015326E+04	17 .1024004E+05	17 .1289117E+05	17 .1765480E+05	17 .2551920E+05	17 .4306710E+05	17 .49
16 -.2613456E+04	16 .3345909E+04	16 .4724586E+04	16 .5677[illegible]E+04	16 .7070067E+04	16 .8909795E+04	16 .1221442E+05	16 .133
21 -.2121689E+04	21 .2575604E+04	21 .3424809E+04	21 .3957787E+04	21 .4790154E+04	21 .5794267E+04	21 .7527394E+04	21 .807
22 .1933290E+04	22 -.2043330E+04	22 .2200680E+04	22 .2345100E+04	22 .2734517E+04	22 .3133411E+04	22 .3814282E+04	22 .406
89 +.2002720E+01	89 +.1924749E+01	89 +.1804119E+01	89 +.1742555E+01	89 +.1636146E+01	89 +.1528017E+01	89 +.1365668E+01	89 +.131
91 -.9271123E+03	91 .9696838E+03	91 .1016985E+04	91 .1035906E+04	91 .1056403E+04	91 .1075324E+04	91 .1100552E+04	91 .109
80 .9554933E+03	80 .9980648E+03	80 .1046943E+04	80 .1064287E+04	80 .1084784E+04	80 .1103705E+04	80 .1127356E+04	80 .112
82 .9239583E+03	82 .9649536E+03	82 .1010679E+04	82 .1029599E+04	82 .1046943E+04	82 .1065863E+04	82 .1087937E+04	82 .108
59 .1296387E+04	59 .1553820E+04	59 .1920982E+04	59 .2372515E+04	59 .3249910E+04	59 .5030962E+04	59 .6798169E+04	59 .727
60 .2344196E+04	60 .2500557E+04	60 .2934178E+04	60 .3919055E+04	60 .5702360E+04	60 .7820113E+04	60 .1020590E+05	60 .108
87 +.2172413E+01	87 +.2106004E+01	87 +.1995220E+01	87 +.1937562E+01	87 +.1833965E+01	87 +.1726773E+01	87 +.1566456E+01	87 +.151
90 +.2063660E+01	90 +.1995376E+01	90 +.1762087E+01	90 +.1701617E+01	90 +.1592550E+01	90 +.1480516E+01	90 +.1318792E+01	90 +.126
8 .2042520E+04	8 .2682126E+04	8 .3600175E+04	8 .4109083E+04	8 .4975767E+04	8 .5818259E+04	8 .6970238E+04	8 .733
9 +.1127185E+06	9 +.1127185E+06	9 +.1127126E+06	9 +.1127126E+06	9 +.1127185E+06	9 +.1127185E+06	9 +.1127185E+06	9 +.112
10 .1368598E+04	10 .1543974E+04	10 .1743351E+04	10 .1832754E+04	10 .1973817E+04	10 .2142316E+04	10 .2438047E+04	10 .252
11 .2290531E+04	11 .2723813E+04	11 .3448879E+04	11 .4098768E+04	11 .5192831E+04	11 .6472043E+04	11 .8157027E+04	11 .867
12 .1970467E+04	12 .2108017E+04	12 .2345100E+04	12 .2774921E+04	12 .3566043E+04	12 .4604544E+04	12 .6076326E+04	12 -.653
13 .2011176E+04	13 .2100899E+04	13 .2228189E+04	13 .2345100E+04	13 .2671731E+04	13 .3386989E+04	13 .4590550E+04	13 .500
15 +.7874771E+03	15 +.1193249E+04	15 +.1870579E+04	15 +.2200680E+04	15 +.2816336E+04	15 +.3507523E+04	15 +.4638869E+04	15 +.503
18 +.1133925E+06	18 +.1133925E+06	18 +.1133866E+06	18 +.1133866E+06	18 +.1133925E+06	18 +.1133925E+06	18 +.1133925E+06	18 +.113
20 .3413297E+05	20 .3395072E+05	20 .3373919E+05	20 .3366698E+05	20 .3355526E+05	20 .3348305E+05	20 .3342459E+05	20 .334
23 +.6909929E+03	23 +.1027989E+04	23 +.1640195E+04	23 +.1164813E+06	23 +.1164872E+06	23 +.1164872E+06	23 +.1164872E+06	23 +.116
24 .1887927E+04	24 .1970457E+04	24 .2042506E+04	24 .2094085E+04	24 .2304015E+04	24 .2837020E+04	24 .3861765E+04	24 .420
25 .2059620E+04	25 .2159343E+04	25 .2345100E+04	25 .2709588E+04	25 .3424801E+04	25 .4360139E+04	25 .5663422E+04	25 -.604
26 .2280067E+04	26 .2747736E+04	26 .3373231E+04	26 .3892453E+04	26 .4933828E+04	26 .5959522E+04	26 -.7369406E+04	26 -.777
27 .2238668E+04	27 .2840448E+04	27 .3679262E+04	27 .4146907E+04	27 .5030927E+04	27 .5986897E+04	27 -.7242038E+04	27 -.761
28 .1358574E+04	28 .1557821E+04	28 .1798369E+04	28 .1898087E+04	28 .2059878E+04	28 .2242131E+04	28 .2561934E+04	28 -.266
29 -.1960212E+04	29 .2355667E+04	29 .3156601E+04	29 .3555474E+04	29 .4236660E+04	29 .4958796E+04	29 .5962969E+04	29 -.626
30 .2073481E+04	30 .2185759E+04	30 .2346820E+04	30 .2419029E+04	30 .2501604E+04	30 .2599608E+04	30 .2840320E+04	30 .293
31 .2087609E+04	31 .2225159E+04	31 .2401837E+04	31 .2484362E+04	31 .2572472E+04	31 .2918065E+04	31 .2923223E+04	31 .277
32 .1908596E+04	32 .2035830E+04	32 .2193803E+04	32 .2260856E+04	32 .2343598E+04	32 .2410653E+04	32 .2489744E+04	32 .250
33 .1930858E+04	33 .2058091E+04	33 .2216154E+04	33 .2279767E+04	33 .2357262E+04	33 .2419160E+04	33 .2479338E+04	33 .246
34 .2070091E+04	34 .2211080E+04	34 .2379486E+04	34 .2436222E+04	34 .2714856E+04	34 .2946971E+04	34 .3230667E+04	34 .330
35 .1973956E+04	35 .2075399E+04	35 .2209277E+04	35 .2264294E+04	35 .2341902E+04	35 .2517278E+04	25 .2845677E+04	35 .292
36 .2114875E+04	36 .2243828E+04	36 .2405275E+04	36 .2475765E+04	36 .2515489E+04	36 .2388256E+04	36 .2368256E+04	36 .235
37 .3060572E+03	37 .3198121E+03	37 .3386985E+03	37 .3455756E+03	37 .3541996E+03	37 .3610771E+03	37 .3679546E+03	37 .367
39 .1313124E+04	39 .1333757E+04	39 .1366829E+04	39 .1384022E+04	39 .1395654E+04	39 .1405970E+04	39 .1416286E+04	39 .141
40 .1829696E+04	40 .1942569E+04	40 .2150875E+04	40 .2244837E+04	40 .2383359E+04	40 .2499536E+04	40 .2622393E+04	40 .263
41 -.3997655E+03	41 .4236565E+03	41 .4561427E+03	41 .4595595E+03	41 .4595348E+03	41 .4612433E+03	41 .4595595E+03	41 .454
43 .1832113E+04	43 .1954652E+04	43 .2108165E+04	43 .2176501E+04	43 .2260472E+04	43 .2333937E+04	43 .2410552E+04	43 .240
44 .3809731E+03	44 .3936084E+03	44 .4100159E+03	44 .4168495E+03	44 .4237612E+03	44 .4323036E+03	44 .4390587E+03	44 .440
58 .4877187E+03	58 .5108981E+03	58 .2768983E+03	58 .2076737E+03	58 .1993713E+03	58 .2119582E+03	58 .2265532E+03	58 .239
63 .1047808E+04	63 .1148765E+04	63 .1469449E+04	63 .1765227E+04	63 .2335085E+04	63 .3216170E+04	63 .4326536E+04	63 .464
64 .5443570E+03	64 .6239786E+03	64 .4342269E+03	64 .3272435E+03	64 .2463704E+03	64 .2149031E+03	64 .2202600E+03	64 .223
65 .8401347E+03	65 .8949880E+03	65 .1006903E+04	65 .1104447E+04	65 .1329237E+04	65 .1662791E+04	65 .2243506E+04	65 .245
66 .5128912E+03	66 .5273712E+03	66 .5317707E+03	66 .5301974E+03	66 .5257979E+03	66 .5163577E+03	66 .4735591E+03	66 .449
68 .7929362E+03	68 .8218870E+03	68 .8480011E+03	68 .8590141E+03	68 .8580744E+03	68 .8549277E+03	68 .8558676E+03	68 .846
70 .8763203E+03	70 .9134603E+03	70 .9534113E+03	70 .9707174E+03	70 .9874085E+03	70 .1011009E+04	70 .1032075E+04	70 .102
71 .9140791E+03	71 .9521222E+03	71 .9943167E+03	71 .1014769E+04	71 .1037084E+04	71 .1063831E+04	71 .1096580E+04	71 .109
72 .7883608E+03	72 .8167418E+03	72 .8482762E+03	72 .8640434E+03	72 .8624667E+03	72 .8671969E+03	72 .8719271E+03	72 .864
73 .5140112E+03	73 .5282017E+03	73 .5376620E+03	73 .5439689E+03	73 .5376620E+03	73 .5187414E+03	73 .4682863E+03	73 .447
74 .8798106E+03	74 .9160752E+03	74 .9570700E+03	74 .9728372E+03	74 .9901812E+03	74 .1007525E+04	74 .1024869E+04	74 .102
75 .8545831E+03	75 .8892710E+03	75 .9302657E+03	75 .9460330E+03	75 .9618002E+03	75 .9775674E+03	75 .9964880E+03	75 .993
76 .2790797E+03	76 .2806564E+03	76 .2806564E+03	76 .2806564E+03	76 .2759262E+03	76 .2743495E+03	76 .2711961E+03	76 .268
77 +.1892066E+02	77 +.2049738E+02	77 +.1892066E+02	77 +.1892066E+02	77 +.1892066E+02	77 +.1892066E+02	77 +.2049738E+02	77 +.189
78 +.1892066E+02	78 +.2049738E+02	78 +.1892066E+02	78 +.1892066E+02	78 +.1892066E+02	78 +.1892066E+02	78 +.2049738E+02	78 +.189
84 .3500322E+03	84 .3594925E+03	84 .3705295E+03	84 .3736830E+03	84 .3768364E+03	84 .3799899E+03	84 .3799899E+03	84 .376
85 .8545831E+03	85 .8892710E+03	85 .9302657E+03	85 .9460330E+03	85 .9633769E+03	85 .9791441E+03	85 .9949113E+03	85 .990
86 .8072814E+03	86 .8403926E+03	86 .8798106E+03	86 .8955778E+03	86 .9097684E+03	86 .9255356E+03	86 .9413028E+03	86 .934

ntinued)

pressure (psi) precedes strain)													
000	19.840		19.300		19.320		19.280		20.350		20.340		20.320
4198E+05	17	-.5076351E+05	17	-.6337272E+05	17	-.1070253E+06	17	.1070253E+06	17	-.1070253E+06	17	-.1070253E+06	17	.1070311E+06
2787E+05	16	-.1347573E+05	16	-.1501621E+05	16	-.1985770E+05	16	-.2060731E+05	16	-.2094773E+05	16	-.2132597E+05	16	-.2136836E+05
7185E+04	21	-.8135641E+04	21	-.8778653E+04	21	-.1117189E+05	21	-.1148824E+05	21	-.1162578E+05	21	-.1176676E+05	21	.1178112E+05
8943E+04	22	-.4098768E+04	22	-.4281011E+04	22	-.5044372E+04	22	.5150968E+04	22	-.5199108E+04	22	-.5243809E+04	22	-.5282238E+04
0198E+01	89	+.1299729E+01	89	+.1252852E+01	89	+.1096910E+01	89	+.1073003E+01	89	+.1062065E+01	89	+.1048783E+01	89	+.1046908E+01
7398E+04	91	-.1094245E+04	91	-.1114742E+04	91	-.1130509E+04	91	-.1130569E+04	91	-.1132086E+04	91	-.1132086E+04	91	-.1132086E+04
4202E+04	80	-.1121049E+04	80	-.1154160E+04	80	-.1157314E+04	80	-.1157314E+04	80	-.1157314E+04	80	-.1157314E+04	80	-.1157314E+04
3208E+04	82	-.1080054E+04	82	-.1111589E+04	82	-.1114742E+04	82	-.1113165E+04	82	-.1113165E+04	82	-.1114742E+04	82	-.1114742E+04
1727E+04	59	-.7344099E+04	59	-.7597398E+04	59	-.8410786E+04	59	-.8527210E+04	59	-.8583626E+04	59	-.8646561E+04	59	-.8656001E+04
7613E+05	60	-.1098783E+05	60	-.1155107E+05	60	-.1314323E+05	60	-.1337450E+05	60	-.1347951E+05	60	-.1360224E+05	60	-.1361797E+05
0829E+01	87	+.1500829E+01	87	+.1459265E+01	87	+.1306604E+01	87	+.1283166E+01	87	+.1272540E+01	87	+.1259571E+01	87	+.1257852E+01
2853E+01	90	+.1252540E+01	90	+.1208476E+01	9	+.1055971E+01	90	+.1032689E+01	90	+.1022064E+01	90	+.1009094E+01	90	+.1007532E+01
7895E+04	8	-.7389473E+04	8	-.7568278E+04	8	-.8503567E+04	8	-.8610163E+04	8	-.8658303E+04				
7092E+06	9	+.1127126E+06	9	+.1127126E+06	9	+.1127126E+06	9	+.1127126E+06	9	+.1127126E+06				
7344E+04	10	.2537660E+04	10	.2661448E+04	10	.2984673E+04	10	-.3025935E+04	10	-.3050006E+04				
2057E+04	11	.8744267E+04	11	.9057176E+04	11	-.1032257E+05	11	-.1047386E+05	11	-.1053919E+05				
3271E+04	12	-.6602042E+04	12	-.6911512E+04	12	-.8068414E+04	12	-.8149396E+04	12	-.8211290E+04				
6548E+04	13	-.5075320E+04	13	-.5336650E+04	13	-.6326957E+04	13	-.6461061E+04	13	-.6522955E+04				
7496E+04	15	+.5113144E+04	15	+.5484508E+04	15	+.6722391E+04	15	+.6914951E+04	15	+.7000915E+04				
3832E+06	18	+.1133866E+06	18	+.1133866E+06	18	+.1133866E+06	18	+.1133866E+06	18	+.1133866E+06				
1596E+05	20	-.3341940E+05	20	-.3335750E+05	20	-.3335750E+05	20	-.3336094E+05	20	-.3337470E+05				
4779E+06	23	+.1164813E+06	23	+.1164813E+06	23	+.1164813E+06	23	+.1164813E+06	23	+.1164813E+06				
5363E+04	24	-.4263818E+04	24	-.4494202E+04	24	-.5281633E+04	24	-.5384790E+04	24	-.5436369E+04				
4995E+04	25	-.6103450E+04	25	-.6395728E+04	25	-.7337895E+04	25	-.7454805E+04	25	-.7502946E+04				
4592E+04	26	-.7826170E+04	26	-.8104694E+04	26	-.9136265E+04	26	-.9253174E+04	26	-.9304753E+04				
2980E+04	27	-.7661120E+04	27	-.7884626E+04	27	-.8854301E+04	27	-.8964335E+04	27	-.9009037E+04				
1448E+04	28	-.2675202E+04	28	-.2792114E+04	28	-.3129093E+04	28	-.3173794E+04	28	-.3197864E+04				
5063E+04	29	.6309764E+04	29	-.6485131E+04	29	-.7279438E+04	29	-.7368841E+04	29	-.7410104E+04				
3095E+04	30	.2945129E+04	30	.3074076E+04	30	.3295863E+04	30	.3337126E+04	30	.3361195E+04				
8359E+04	31	-.2515309E+04	31	-.2525625E+04	31	.2594396E+04	31	-.2566887E+04	31	.2324469E+04				
3274E+04	32	.2515309E+04	32	.2632220E+04	32	.2730219E+04	32	.2740535E+04	32	.2747412E+04				
2011E+04	33	-.2458572E+04	33	.2515309E+04	33	-.2594396E+04	33	.2616747E+04	33	-.2627062E+04				
2740E+04	34	.3314775E+04	34	.3442002E+04	34	.3641439E+04	34	.3670666E+04	34	.3684421E+04				
6217E+04	35	-.2945129E+04	35	-.3096426E+04	35	.3376669E+04	35	-.3428248E+04	35	-.3455756E+04				
1977E+04	36	.2339943E+04	36	.2369801E+04	36	.2365732E+04	36	.2351977E+04	36	.2327907E+04				
9262E+03	37	-.3662070E+03	37	-.3748034E+03	37	-.3713648E+03	37	-.3713648E+03	37	-.3730841E+03				
4968E+04	39	.1413249E+04	39	.1420127E+04	39	.1416688E+04	39	.1413249E+04	39	.1414968E+04				
7769E+04	40	.2637769E+04	40	.2702688E+04	40	.2753940E+04	40	.2757357E+04	40	.2760935E+04				
4343E+03	41	.4527259E+03	41	.4612679E+03	41	.4527259E+03	41	.4493091E+03	41	.4509923E+03				
8843E+04	43	.2405427E+04	43	.2463512E+04	43	.2478888E+04	43	.2484013E+04	43	.2487701E+04				
7671E+03	44	.4390587E+03	44	.4476007E+03	44	.4476007E+03	44	.4476007E+03	44	.4493885E+03				
1394E+03	58	.2359929E+03	58	.2800449E+03	58	.3429763E+03	58	-.3492695E+03	58	-.3567081E+03				
7486E+04	63	.4723004E+04	63	.5088006E+04	63	.5780252E+04	63	.5868356E+04	63	.5912922E+04				
4066E+03	64	.2202600E+03	64	.2391394E+03	64	.2737517E+03	64	.2768983E+03	64	.2841312E+03				
4326E+04	65	.2498378E+04	65	.2803595E+04	65	.3420323E+04	65	.3508477E+04	65	.3557126E+04				
9598E+03	66	.4436666E+03	66	.4436666E+03	66	.3775886E+03	66	.3665756E+03	66	.3621677E+03				
4278E+03	68	.8417080E+03	68	.8668805E+03	68	.8448545E+03	68	.8401347E+03	68	.8423408E+03				
5782E+04	70	.1022636E+04	70	.1047808E+04	70	.1036795E+04	70	.1033649E+04	70	.1034609E+04				
5007E+04	71	.1091860E+04	71	.1124899E+04	71	.1121755E+04	71	.1118606E+04	71	.1120473E+04				
0434E+03	72	.8593133E+03	72	.8829641E+03	72	.8640434E+03	72	.8608900E+03	72	.8608900E+03				
7890E+03	73	.4399054E+03	73	.4351752E+03	73	.3642227E+03	73	.3516089E+03	73	.3468787E+03				
0139E+04	74	.1016985E+04	74	.1046943E+04	74	.1043789E+04	74	.1042213E+04	74	.1042213E+04				
3346E+03	75	.9886044E+03	75	.1018562E+04	75	.1016985E+04	75	.1015409E+04	75	.1015409E+04				
0426E+03	76	.2648892E+03	76	.2743495E+03	76	.2664659E+03	76	.2648892E+03	76	.2664659E+03				
2065E+02	77	+.2049738E+02	77	+.2049738E+02	77	+.2049738E+02	77	+.2049738E+02	77	+.1892066E+02				
2066E+02	78	+.2049738E+02	78	+.2049738E+02	78	+.2049738E+02	78	+.2049738E+02	78	+.1892066E+02				
8364E+03	84	.3736830E+03	84	.3831433E+03	84	.3752597E+03	84	.3736830E+03	84	.3752597E+03				
1812E+03	85	.9870277E+03	85	.1013832E+04	85	.1010679E+04	85	.1007525E+04	85	.1009101E+04				
9959E+03	86	.9318425E+03	86	.9570700E+03	86	.9523398E+03	86	.9507631E+03	86	.9507631E+03				

2

BLANK PAGE

Table B-1 (continued)

Strain (μm/m) at pressure (psi)
(channel No. precedes strain)

20,450	20,590	20,730	20,840	20,910	20,950	20,930	20,890
17 -.1070194E+06	17 -.1070311E+06	17 -.1070311E+06	17 -.1070311E+06	17 -.1070311E+06	17 -.1070253E+06	17 .1070194E+06	17 .1070253E+06
16 -.2139361E+05	16 -.2163314E+05	16 -.2230026E+05	16 .2440133E+05	16 .2927059E+05	16 .3433374E+05	16 .3928696E+05	16 .4178886E+05
21 -.1179711E+05	21 -.1186365E+05	21 -.1204246E+05	21 -.1296749E+05	21 -.1519235E+05	21 .1745415E+05	21 .1966069E+05	21 .2075861E+05
22 -.5260011E+04	22 -.5286064E+04	22 -.5337645E+04	22 .5530215E+04	22 -.6049465E+04	22 -.6519516E+04	22 -.6910436E+04	22 .7086879E+04
89 +.1044721E+01	89 +.1039720E+01	89 +.1027532E+01	89 +.9839376E+00	89 +.8836219E+00	89 +.7876813E+00	89 +.7050224E+00	89 +.6668962E+00
91 -.1136816E+04	91 -.1144934E+04	91 -.1155972E+04	91 -.1166774E+04	91 -.1169927E+04	91 -.1174893E+04	91 -.1177811E+04	91 -.1177811E+04
80 -.1162044E+04	80 -.1170568E+04	80 -.1183182E+04	80 .1192061E+04	80 -.1195155E+04	80 -.1200527E+04	80 .1201462E+04	80 .1201462E+04
82 -.1117895E+04	82 -.1128126E+04	82 -.1139164E+04	82 .1147853E+04	82 -.1151006E+04	82 -.1154932E+04	82 -.1157314E+04	82 -.1154160E+04
59 -.8664085E+04	59 -.8689042E+04	59 -.8744109E+04	59 -.8871552E+04	59 -.9246014E+04	59 -.9684984E+04	59 -.1005330E+05	59 -.1022006E+05
60 -.1363252E+05	60 -.1367461E+05	60 -.1379419E+05	60 -.1416393E+05	60 -.1501355E+05	60 .1588677E+05	60 .1660761E+05	60 -.1693485E+05
87 +.1256133E+01	87 +.1252227E+01	87 +.1241446E+01	87 +.1198632E+01	87 +.1099722E+01	87 +.1007532E+01	87 +.9295608E+00	87 +.8934659E+00
90 +.1005813E+01	90 +.1001906E+01	90 +.9911253E+00	90 +.9481552E+00	90 +.8525271E+00	90 +.7620555E+00	90 +.7150228E+00	90 +.7148665E+00

370

311E+06	17
189E+05	16
553E+05	23
811E+04	2
330E+00	8
674E+04	9
2104E+04	3
6508E+04	8
1590E+05	5
2156E+05	6
3090E+00	8
8665E+00	9

BLANK PAGE

[illegible]

[illegible] (psi)
[illegible] stream)

20.890	20.870	20.870	20.860	20.840	20.830	20.810
17 -.1070253E+06	17 -.1070311E+06	17 -.1070311E+06	17 -.1070311E+06	17 -.1070253E+06	17 -.1070321E+06	17 -.1070321E+06
16 -.4178886E+05	16 -.4323189E+05	16 -.4415003E+05	16 -.4478620E+05	16 -.4527212E+05	16 -.4604924E+05	16 -.4701892E+05
21 -.2075861E+05	21 -.2138553E+05	21 -.2177754E+05	21 -.2204920E+05	21 -.2225095E+05	21 -.2257417E+05	21 -.2296960E+05
22 -.7086879E+04	22 -.7188811E+04	22 -.7239270E+04	22 -.7273657E+04	22 -.7300070E+04	22 -.7337895E+05	22 -.7382596E+04
89 +.6660962E+00	89 +.6453330E+00	89 +.6320514E+00	89 +.6226760E+00	89 +.6154883E+00	89 +.6040817E+00	89 +.5895500E+00
91 -.1177811E+04	91 -.1179624E+04	91 -.1177811E+04	91 -.1176471E+04	91 -.1178047E+04	91 -.1176234E+04	91 -.1176234E+04
80 -.1201462E+04	80 -.1202104E+04	80 -.1199885E+04	80 -.1198951E+04	80 -.1200527E+04	80 -.1199885E+04	80 -.1199885E+04
82 -.1154160E+04	82 -.1156508E+04	82 -.1155737E+04	82 -.1153355E+04	82 -.1154932E+04	82 -.1154160E+04	82 -.1152583E+04
59 -.1022006E+05	59 -.1031590E+05	59 -.1037412E+05	59 -.1041188E+05	59 -.1044334E+05	59 -.1048910E+05	59 -.1054888E+05
60 -.1693485E+05	60 -.1712186E+05	60 -.1723357E+05	60 -.1731066E+05	60 -.1737045E+05	60 -.1746190E+05	60 -.1757832E+05
87 +.8934659E+00	87 +.8733090E+00	87 +.8608086E+00	87 +.8522146E+00	87 +.8454957E+00	87 +.8351828E+00	87 +.8217449E+00
90 +.7148665E+00	90 +.7148665E+00	90 +.7148665E+00	90 +.7148665E+00	90 +.7148655E+00	90 +.7148665E+00	90 +.7147102E+00
					8 -.1046699E+05	
					9 +.1127058E+06	
					10 -.4085013E+04	
					11 -.1308717E+05	
					12 -.1043260E+05	
					13 -.8617040E+04	
					15 +.1093463E+05	
					18 +.1133797E+06	
					20 -.5653342E+05	
					23 +.1164745E+06	
					24 -.7097195E+04	
					25 -.9524821E+04	
					26 -.1146073E+05	
					27 -.1098621E+05	
					28 -.4253503E+04	
					29 -.8995282E+04	
					30 -.4593921E+04	
					31 +.6195431E+05	
					32 -.2996708E+04	
					33 -.2881516E+04	
					34 -.4303362E+04	
					35 -.4654095E+04	
					36 -.2324469E+04	
					37 -.3730841E+03	
					39 -.1416688E+04	
					40 -.2894029E+04	
					41 -.4493091E+03	
					43 -.2583100E+04	
					44 -.4544343E+03	
					58 -.5191844E+03	
					63 -.6758837E+04	
					64 -.4216466E+03	
					65 -.4697831E+04	
					66 -.1258628E+03	
				2	68 -.8086690E+03	
					70 -.1038368E+04	
					71 -.1131193E+04	
					72 -.8356624E+03	
					73 -.1072170E+03	
					74 -.1065863E+04	
					75 -.1043789E+04	
					76 -.2601590E+03	
					77 +.1892066E+02	
					78 +.1892066E+02	
					84 -.3642227E+03	
					85 .1024869E+04	
					86 .9633769E+03	

Table B-1 (continued)

Strain (μm/m) at pressure (
(channel No. precedes stra

20,840	21,010	21,130	21,230	21,270	21,270	21,360	20,9
17 .1070321E+06	17 .1070321E+06	17 .1070321E+06	17 -.1070321E+06	17 -.1070321E+06	17 -.1070321E+06	17 -.1070263E+06	17 -.1070
16 .4724586E+05	16 .4769631E+05	16 .4908205E+05	16 .5396825E+05	16 -.1123688E+06	16 -.1123688E+06	16 -.1123629E+06	16 -.1123
21 -.2306588E+05	21 -.2325844E+05	21 .2381893E+05	21 -.2615371E+05	21 -.3299989E+05	21 -.4232184E+05	21 -.5341187E+05	21 -.1128
22 .7392911E+04	22 -.7427297E+04	22 -.7492629E+04	22 -.7702382E+04	22 -.8372902E+04	22 -.9077808E+04	22 -.9723034E+04	22 -.1028
89 +.5859561E+00	89 +.5792372E+00	89 +.5636117E+00	89 +.5101725E+00	89 +.3756369E+00	89 +.2226633E+00	89 +.7187730E-01	89 -.6797
91 -.1177811E+04	91 .1185694E+04	91 -.1196731E+04	91 -.1206192E+04	91 -.1207768E+04	91 -.1210922E+04	91 -.1210922E+04	91 -.1188
80 -.1198308E+04	80 -.1209346E+04	80 -.1218805E+04	80 -.1228266E+04	80 -.1229842E+04	80 -.1229842E+04	80 -.1229842E+04	80 -.1204
82 -.1152583E+04	82 -.1162044E+04	82 -.1171504E+04	82 -.1180964E+04	82 -.1182541E+04	82 -.1180964E+04	82 -.1182541E+04	82 -.1155
59 -.1056461E+05	59 -.1059439E+05	59 -.1065429E+05	59 -.1080690E+05	59 -.1126472E+05	59 -.1184055E+05	59 -.1237075E+05	59 -.1280
60 -.1760821E+05	60 -.1766152E+05	60 -.1778914E+05	60 -.1818089E+05	60 -.1919881E+05	60 -.2041968E+05	60 -.2157604E+05	60 -.2257
87 +.8186198E+00	87 +.8133071E+00	87 +.7995567E+00	87 +.7483050E+00	87 +.6181446E+00	87 +.4717338E+00	87 +.3295417E+00	87 +.1982
90 +.7148665E+00	90 +.7147102E+00	90 +.7148665E+00	90 +.7153353E+00	90 +.6051755E+00	90 +.4729838E+00	90 +.3382920E+00	90 +.2161

(continued)

R pressure (psi) –
precedes strain)

20,930	19,450	19,080	18,920	18,750	18,690	0
17 -.1070390E+06	17 -.1070390E+06	17 -.1070449E+06	17 -.1070449E+06	17 -.1070449E+06	17 -.1070449E+06	17 -.1071594E+06
16 -.1123757E+06	16 -.1123757E+06	16 -.1123815E+06	16 -.1123815E+06	16 -.1123815E+06	16 -.1123815E+06	16 .1124960E+06
21 -.1128811E+06	21 -.1128811E+06	21 -.1128870E+06	21 -.1128870E+06	21 -.1128870E+06	21 -.1128870E+06	21 -.1130015E+06
22 -.1028130E+05	22 -.1008874E+05	22 -.1002121E+05	22 -.1000058E+05	22 -.9973071E+04	22 -.9955877E+04	22 -.7031862E+04
89 -.6797093E-01	89 -.4062629E-01	89 -.3140725E-01	89 -.2968844E-01	89 -.2812590E-01	89 -.2781338E-01	89 +.3998565E+00
91 -.1188848E+04	91 -.1100552E+04	91 -.1070824E+04	91 -.1062710E+04	91 -.1050096E+04	91 .1045596E+04	91 +.5676198E+02
80 -.1204615E+04	80 -.1114742E+04	80 -.1075420E+04	80 -.1076900E+04	80 -.1062710E+04	80 -.1058615E+04	80 +.7725936E+02
82 -.1155737E+04	82 -.1069017E+04	82 -.1039825E+04	82 -.1032752E+04	82 -.1018562E+04	82 .1016173E+04	82 +.8356624E+02
59 -.1280025E+05	59 -.1267910E+05	59 -.1263662E+05	59 -.1262246E+05	59 -.1259729E+05	59 -.1259099E+05	59 -.1058821E+05
60 -.2257987E+05	60 -.2239422E+05	60 -.2232813E+05	60 -.2230768E+05	60 -.2227936E+05	60 -.2227149E+05	60 -.1898170E+05
87 +.1982876E+00	87 +.2136005E+00	87 +.2187569E+00	87 +.2204757E+00	87 +.2228196E+00	87 +.2234446E+00	87 +.5075162E+00
90 +.2161006E+00	90 +.2314136E+00	90 +.2365700E+00	90 +.2379763E+00	90 +.2400076E+00	90 +.2404764E+00	90 +.5086099E+00
					8 -.1247566E+05	8 -.1037071E+05
					9 +.1127048E+06	9 +.1125785E+06
					10 -.5577620E+04	10 -.4305081E+04
					11 -.1585637E+05	11 .1338289E+05
					12 -.1232452E+05	12 -.9848046E+04
					13 -.1056364E+05	13 -.7984344E+04
					15 +.1727969E+05	15 +.1582427E+05
					18 +.1133788E+06	18 +.1132525E+06
					20 -.7569018E+05	20 +.1681457E+04
					23 +.1164734E+06	23 +.1276051E+05
					24 -.8507508E+04	24 -.6103450E+04
					25 -.1127889E+05	25 -.8878371E+04
					26 -.1389958E+05	26 -.1157076E+05
					27 -.1328735E+05	27 -.1109281E+05
					28 .5787475E+04	28 .4604236E+04
					29 -.1069806E+05	29 -.8654865E+04
					30 .6191375E+04	30 .3701614E+04
					31 +.6195726E+05	31 .2138786E+04
					32 .3036504E+04	32 -.9593592E+03
					33 -.2945287E+04	33 .8200974E+03
					34 .4731678E+04	34 .2391521E+04
					35 -.6100448E+04	35 .3696455E+04
					36 +.5729113E+05	36 .4057505E+03
					37 -.3180928E+03	37 -.1891210E+02
					39 .1309685E+04	39 .8355709E+03
					40 .2738725E+04	40 .6981935E+03
					41 .3911952E+03	41 +.1025040E+02
					43 .2397150E+04	43 .3724311E+03
					44 .4254696E+03	44 .9054518E+02
					58 .7185826E+03	58 .3775886E+03
					63 -.7492583E+04	63 .5975340E+04
					64 .5453102E+03	64 .1699149E+03
					65 -.4982597E+04	65 .3788473E+04
					66 +.3474211E+03	66 +.9077860E+03
					68 .5843085E+03	68 +.3807352E+03
					70 -.8615391E+03	70 +.1762080E+03
					71 .9631358E+03	71 +.1252628E+03
					72 .6219331E+03	72 +.3437253E+03
					73 +.3603734E+03	73 +.9271123E+03
					74 .9236380E+03	74 +.1277144E+03
					75 .9108863E+03	75 +.1103705E+03
					76 .1942139E+03	76 +.1513652E+03
					77 +.2160829E+02	77 +.4730165E+01
					78 +.2160829E+02	78 +.4730165E+01
					84 .2901585E+03	84 +.1214075E+03
					85 .8782988E+03	85 +.1355980E+03
					86 .8188468E+03	86 +.1403282E+03

2

BLANK PAGE

Table B-2. Pressure-strain data from V-7 test
(manual readout from BLH indicators)

Pressure (psi)	Strain (μm/m) at gage No. —									
	14	19	38	42	56	57	61	62	77	83
0	0	0	0	0	0	0	0	0	0	0
1,000	300	70	160	140	80	90	130	90	70	70
2,000	400	130	280	250	130	150	230	150	120	120
3,000	600	190	430	380	200	230	350	250	180	190
4,000	700	250	580	510	260	300	460	320	240	250
5,000	700	280	730	640	320	370	580	410	300	320
6,000	700	370	860	760	390	440	690	490	350	370
7,000	700	500	990	880	450	510	810	570	410	440
8,000	800	640	1130	990	510	580	920	650	470	500
9,000	900	820	1240	1100	560	640	1,030	720	520	550
10,000	1,100	1,070	1360	1210	620	710	1,140	790	570	610
11,000	1,300	1,370	1430	1320	670	770	1,250	870	630	670
12,000	1,500	1,750	1540	1440	720	840	1,350	940	680	730
13,000	1,600	2,210	1650	1550	770	890	1,450	1,020	730	780
14,000	1,800	2,730	1770	1670	810	950	1,560	1,090	770	840
15,000	1,900	3,370	1880	1790	850	1010	1,900	1,160	820	890
16,000	2,100	4,410	2000		900	1080	2,370	1,290	870	940
17,000	2,200	5,780	2120		950	1200	2,440	1,530	910	980
18,000	2,500	8,340	2260		1110	1630	2,790	1,960	950	1030
18,500	2,900	10,200	2330		1290	1990	3,680	2,350	960	1040
19,000	3,400	14,550	2430		1650	2670	5,320	3,170	990	1060
19,500	3,900	21,000	2550		2140	3720	7,370	4,690	1000	1080
20,000	4,800	35,000	2650		3030	5510	9,490	6,370	1030	1110
20,000	4,690	39,380	2660		3190	5740	9,740	6,540	1030	1100
20,500	5,690		2760		4260	6820	11,830	7,650	1060	1130
21,000	7,790		2880		5290	7770	15,150	9,230	1100	1170
21,300	11,500						19,940			
18,600	11,270		2720		6050	9340	19,610	11,090	970	1030
0	8,290		580		4760	7740	16,410	9,150	60	230

Appendix C

Model Test Data

Table C-1. Pressure-strain data from model vessel V4.3 (vessel V-4 prolongation)[a]

See Fig. C-1 for gage locations
Test temperature: 195°F
Flaw size: length - 1.66 in.; depth - 0.60 in.

Pressure (psi)	Strain (μm/m) at gage No. -										
	1	2	3	4	5	6	7	8	9	10	11
0	-0	+10	-10	-0	0	0	0	+10	0	0	0
2,000	+130	+170	+220	+230	+170	+120	+120	+140	+140	+140	+130
4,000	+220	+290	+390	+400	+300	+210	+210	+240	+230	+230	+220
6,000	+320	+440	+600	+620	+450	+320	+310	+350	+350	+350	+320
8,000	+440	+590	+830	+860	+610	+430	+420	+460	+460	+460	+430
9,000	+490	+660	+940	+990	+680	+480	+470	+510	+510	+510	+480
10,000	+550	+740	+1,070	+1,110	+760	+530	+520	+570	+570	+570	+540
11,000	+610	+820	+1,210	+1,250	+850	+590	+570	+630	+630	+630	+600
12,000	+660	+900	+1,340	+1,380	+920	+640	+620	+680	+680	+680	+650
13,000	+720	+980	+1,500	+1,540	+1,020	+700	+670	+740	+740	+740	+710
14,000	+760	+1,070	+1,670	+1,720	+1,100	+750	+730	+790	+790	+800	+770
15,000	+830	+1,150	+1,840	+1,900	+1,190	+790	+770	+840	+840	+850	+830
16,000	+880	+1,260	+2,030	+2,120	+1,300	+850	+830	+900	+900	+900	+890
17,000	+920	+1,360	+2,200	+2,310	+1,400	+890	+890	+940	+940	+950	+930
18,000	+980	+1,520	+2,430	+2,580	+1,550	+940	+920	+990	+990	+1000	+990
19,000	+1,050	+1,710	+2,710	+2,920	+1,730	+1010	+970	+1050	+1060	+1060	+1060
20,000	+1,120	+1,920	+3,070	+3,300	+1,940	+1070	+1030	+1120	+1120	+1120	+1120
21,000	+1,220	+2,370	+3,690	+3,950	+2,290	+1170	+1080	+1190	+1190	+1200	+1190
22,000	+1,370	+3,250	+4,630 +4,980	+5,080	+2,990	+1310	+1150	+1270	+1260 +1280	+1290	+1270
23,000	+1,580	+4,440	+6,140 +6,620	+6,760	+4,120	+1500	+1200	+1360	+1360	+1370	+1340
24,000	+1,990	+6,160	+8,600 +9,150	+9,630	+6,010	+1900	+1270	+1470	+1470 +1480	+1490	+1430
25,000	+3,100	+9,260	+13,300 +13,930	+15,890	+9,970	+3160	+1370	+1640	+1650	+1680	+1560
26,000	+4,770	+13,340	+20,240 +20,930	+24,200	+14,390	+4430	+1460	+1840	+1850	+1920	+1670
27,000	+6,430	+18,820	+30,000 +32,090	+36,290	+20,030	+5870	+1630	+2630	+2540 +2690	+2640	+1870
27,500	+6,650	+19,930	33,500 34,950	+39,500	+21,260	+6150	+1710	+3150	+3080 +3180	+3190	+1980
27,500	+6,920	+20,950	37,400	+42,330	+22,420	+6430	+1780	+3450	+3500	+3500	+2080
28,200	+9,150	28,840	61,340	71,400	+35,250	+9240	+190		+4220		
14,000	+10,800	+45,530	Open	Open	Open	+9600	+1150	+3320	+3330	+3340	+1600

[a] 1 in. = 25.4 mm; 1 psi = 6.895 kPa.

Table C-2. Pressure-strain data from model vessel V7E-A2 (vessel V-7 prolongation)[a]

See Fig. C-1 for gage locations
Test temperature: 193°F
Flaw size: length = 1.7 in.; depth = 0.71 in.

Pressure (psi)	Strain (μm/m) at gage No.										
	1	2	3	4	5	6	7	8	9	10	11
0	0	0	0	0	10	0	0	0	0	0	0
4,000	220	320	450	430	310	230	220	220	230	220	230
8,000	420	620	900	850	590	440	410	420	430	420	430
12,000	620	940	1,400	1,310	890	660	610	640	650	640	640
16,000	820	1,260	1,950	1,850	1,210	860	810	850	870	850	860
20,000	940	1,880	2,840	2,620	1,660	1,060	990	1050	1080	1050	1050
21,000	980	2,180	3,340	2,940	1,830	1,140	1020	1120	1140	1120	1100
22,000	1030	3,250	4,870	3,910	2,290	1,300	1100	1220	1230	1220	1170
23,000	1140	5,460	7,560	5,960	3,720	1,720	1180	1320	1340	1330	1260
23,500	1230	6,560	8,890	7,140	4,680	2,110	1210	1370	1380	1370	1290
24,000	1530	8,640	11,690	9,540	6,480	3,120	1280	1450	1470	1450	1350
24,500	2440	10,830	15,120	12,360	8,240	4,180	1330	1530	1560	1540	1420
25,000	3230	13,520	19,700	15,980	10,410	5,000	1370	1620	1650	1640	1500
25,250	3400	14,490	21,350	17,420	11,210	5,240	1450	1670	1700	1680	1550
25,500	3530	15,320	22,810	18,600	11,870	5,450	1480	1700	1730	1710	1580
25,750	3930	17,830	27,220	22,030	13,860	6,180	1540	1730	1760	1740	1640
26,000	4270	20,030	31,400	25,190	15,630	6,860	1600	1750	1780	1760	1710
26,250	4460	21,270	33,530	27,040	16,630	7,240	1640	1750	1780	1750	1750
26,500	4940	24,500	39,750	31,850	19,200	8,210	1690	1760	1790	1760	1800
26,500	4990	24,770	40,350	32,350	19,440	8,300	1700	1770	1800	1780	1840
26,750	5020	25,130	41,100	32,990	19,730	8,400	1720	1790	1820	1800	1870
27,000	5830	31,040	53,660	42,400	24,370	10,040	1800	1820	1880	1820	1970
27,000	5890	31,360	54,430	43,020	24,650	10,140	1840	1870	1890	1870	2020
27,250	5980	32,590	57,550	45,330	25,620	10,420	1890	1910	1940	1890	2070
27,500			59,880						i930		
18,000	5560	32,650	58,610	45,800	25,510	10,050	1430	1400	1450	1410	1560
0	4580	30,770	55,210	42,890	23,800	8,980	510	410	430	420	600

[a]1 in. = 25.4 mm; 1 psi = 6.895 kPa.

Table C-3. Pressure-strain data from model vessel V7E-A3 (vessel V-7 prolongation)[a]

See Fig. C-1 for gage locations
Test temperature: 193°F
Flaw size: length = 2.55 in.; depth = 0.71 in.

Pressure (psi)	Strain (μm/m) at gage No. –										
	1	2	3	4	5	6	7	8	9	10	11
0	0	0	0	0	0	0	0	0	0	0	0
1,000	+60	+90	+140	+120	+90	+70	+60	+60	+70	+60	+60
2,000	+100	+180	+260	+240	+170	+140	+120	+120	+120	+110	+110
3,000	+160	+270	+390	+370	+260	+200	+170	+180	+180	+180	+170
4,000	+210	+360	+510	+500	+340	+260	+210	+230	+230	+220	+210
5,000	+260	+450	+650	+640	+430	+330	+270	+280	+280	+280	+260
5,500	+290	+490	+710	+690	+470	+350	+290	+300	+310	+300	+280
5,750	+300	+510	+740	+720	+490	+370	+300	+320	+320	+310	+290
6,000	+320	+540	+790	+770	+510	+390	+310	+340	+340	+330	+310
6,300	+330	+550	+820	+800	+530	+410	+320	+340	+350	+340	+320
6,500	+340	+570	+850	+830	+550	+390	+330	+350	+360	+350	+330
6,750	+350	+590	+880	+860	+520	+430	+340	+370	+370	+370	+340
7,000	+360	+610	+910	+890	+590	+450	+360	+380	+380	+380	+350
7,300	+370	+630	+950	+920	+610	+460	+370	+390	+400	+390	+360
7,500	+380	+650	+970	+950	+620	+470	+370	+400	+410	+400	+360
7,750	+400	+680	+1,020	+1,000	+650	+490	+390	+420	+430	+420	+390
8,000	+410	+700	+1,060	+1,030	+670	+510	+400	+430	+440	+430	+400
8,250	+420	+720	+1,090	+1,060	+690	+520	+410	+440	+450	+440	+410
8,500	+430	+740	+1,120	+1,090	+700	+530	+420	+450	+460	+450	+420
8,750	+450	+770	+1,170	+1,150	+730	+550	+440	+470	+480	+470	+440
9,000	+460	+790	+1,200	+1,170	+750	+560	+450	+480	+490	+480	+440
9,300	+470	+820	+1,250	+1,220	+780	+580	+470	+500	+510	+500	+460
9,500	+490	+840	+1,280	+1,250	+800	+600	+480	+510	+520	+510	+470
9,800	+500	+860	+1,330	+1,300	+830	+620	+490	+530	+530	+530	+490
10,000	+510	+880	+1,360	+1,330	+850	+630	+500	+540	+550	+540	+500
10,300	+520	+910	+1,410	+1,380	+870	+650	+520	+550	+560	+550	+510
10,500	+530	+920	+1,440	+1,410	+890	+660	+530	+560	+570	+560	+520
10,800	+550	+960	+1,500	+1,470	+910	+680	+540	+580	+590	+580	+540
11,000	+560	+970	+1,530	+1,500	+930	+690	+550	+590	+600	+590	+550
12,000	+600	+1,060	+1,690	+1,670	+1,020	+750	+600	+640	+650	+640	+590
13,000	+650	+1,150	+1,870	+1,860	+1,110	+810	+650	+690	+700	+590	+640
14,000	+690	+1,280	+2,130	+2,120	+1,230	+870	+700	+750	+760	+750	+690
15,000	+730	+1,410	+2,350	+2,330	+1,350	+940	+750	+800	+810	+800	+740
16,000	+760	+1,570	+2,570	+2,540	+1,500	+1020	+790	+850	+860	+850	+790
17,000	+790	+1,770	+2,840	+2,720	+1,660	+1100	+840	+890	+910	+900	+830
18,000	+820	+1,980	+3,190	+2,950	+1,760	+1200	+870	+930	+950	+930	+870
18,500	+850	+2,170	+3,540	+3,170	+1 830	+1280	+900	+960	+970	+960	+890
19,000	+880	+2,480	+4,070	+3,550	+1,950	+1380	+920	+990	+1000	+990	+920
19,500	+910	+2,910	+4,700	+4,060	+2,190	+1490	+940	+1010	+1030	+1020	+940
20,000	+970	+3,640	+5,620	+4,960	+2,700	+1710	+970	+1050	+1060	+1050	+960
20,500	+1050	+4,420	+6,540	+5,950	+3,400	+1970	+990	+1070	+1090	+1080	+980
21,000	+1200	+5,610	+8,200	+7,600	+4,600	+2640	+1010	+1110	+1140	+1120	+1010
21,500	+1390	+6,580	+9,600	+9,020	+5,560	+3320	+1030	+1150	+1170	+1160	+1030
22,000	+1820	+8,910	+11,740	+11,160	+6,770	+4120	+1060	+1200	+1220	+1210	+1060
22,500	+2320	+9,440	+14,200	+13,460	+7,980	+4750	+1090	+1240	+1260	+1250	+1090
23,000	+2720	+11,330	+17,700	+17,040	+9,690	+5570	+1110	+1280	+1300	+1300	+1120
23,400	+3130	+14,050	+22,600	+22,160	+11,940	+6640	+1140	+1330	+1360	+1340	+1140
23,700	+3330	+15,470	+26,080	+24,990	+13,100	+7160	+1150	+1350	+1380	+1370	+1160
23,950	+3600	+20,710	+38,270	+36,430	+17,160	+8690	+940	+1120	+1200	+1130	+920
17,000	+3490	+20,490	+37,510	+36,060	+16,970	+8550	+820	+1000	+1020	+1010	+810
0	+2650	+18,570	+34,090	+32,450	+15,170	+7410	+50	+180	+190	+180	+50

[a] 1 in. = 25.4 mm; 1 psi = 6.895 kPa.

ORNL-DWG 76-7983

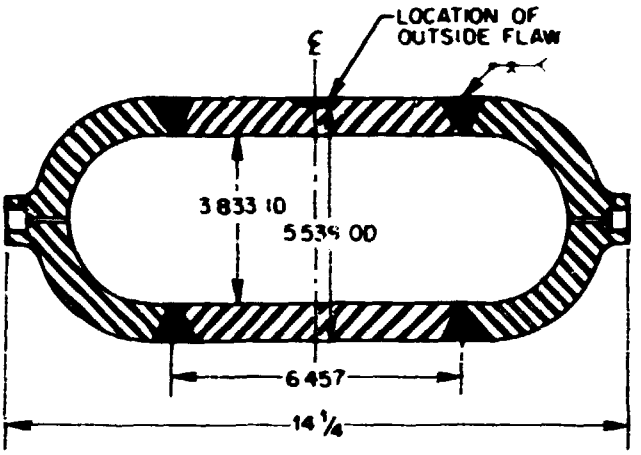

SKETCH OF MODELS

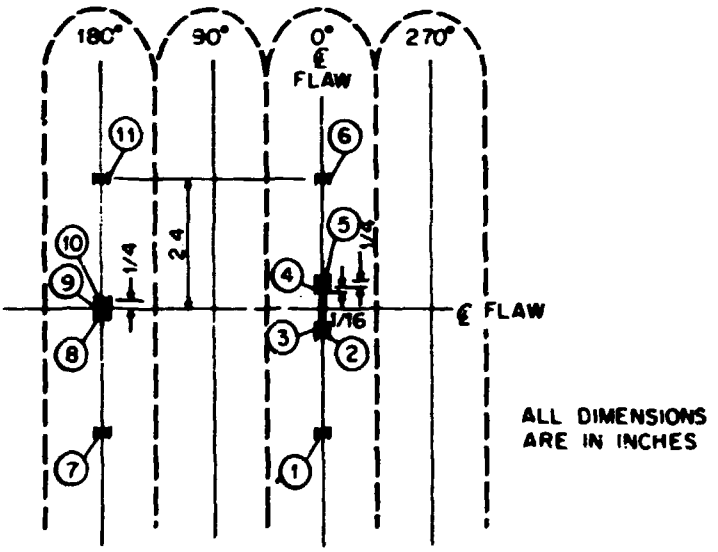

STRAIN GAGE LOCATIONS
MODEL V4-1

NOTE: WHERE NO DIMENSIONS ARE SHOWN, GAGES ARE PLACED SYMMETRICALLY ABOUT CENTER LINE OF FLAW. ALL GAGES ARE LOCATED ON OUTSIDE SURFACE.

Fig. C-1. Strain gage locations for models tested for ITV-7.

Appendix D

Acoustic-Emission Monitoring of HSST Intermediate Test Vessel V-7*

INTRODUCTION

Acoustic emission (AE) is the term applied to the spontaneously generated elastic waves produced within a material under stress. Plastic deformation and the nucleation and growth of cracks are the primary sources of AE in metals. Acoustic-emission techniques have been successfully applied to the evaluation of structural integrity in bridges, nuclear and petrochemical pressure vessels, wind tunnels, rocket-motor cases, and composite materials and pipeline.[1-10] Acoustic emission has already been incorporated into production line testing in one AEC facility.[9]

The Nuclear Regulatory Commission in conjunction with Oak Ridge National Laboratory is conducting a continuing test program on heavy-section-steel pressure vessels. The purpose of the program is to gather experimental data concerning the failure modes of thick-walled pressure vessels with very large flaws. A secondary purpose is to demonstrate and evaluate various methods of nondestructive testing techniques in detecting and analyzing flaws and thus preventing catastrophic in-service failure. Dunegan/Endevco has participated in the AE monitoring of three of these test vessels. This report covers the monitoring of intermediate test vessel V-7; a similar report will be generated from data acquired from each of the other vessels monitored by Dunegan/Endevco.

EXPERIMENTAL PROCEDURE AND RESULTS

A block diagram of the Dunegan/Endevco model 1032 source location system used in this work is presented in Fig. D-1. The features and components of the model listed below are worth noting.

Transducer: Dunegan/Endevco S140B single-ended 140-kHz resonant frequency transducers were used in this work.

Array selector/audio monitor: The 1032 utilizes a four-transducer array configuration. Each array is totally independent of all other arrays and monitors AE activity both inside and outside the array boundaries. The array selector allows oscilloscope monitoring via thumbwheel switch selection of the four analog signals within any array. The audio monitor heterodynes the high-frequency analog signal from any channel to provide an audible measure of the AE activity.

Delta-t interface: The delta-*t* interface is the heart of the 1032. When an AE event has occurred, this module determines which array has been excited, locks out all other arrays to reduce subsequent extraneous data, determines the transducer arrival sequence, measures the corresponding arrival times, and stores the event information in computer memory.

Interdata model 74 computer: The model 74 computer calculates the *X* and *Y* coordinates of the source as well as the event severity and prepares the source information for display on the CRT and printout on the terminal.

613 CRT: The CRT provides an instantaneous display of the location of each source in relation to the position of the four sensors involved. A dual histogram indicating the number of events per array and the number of ringdown counts (event magnitude) per array alerts the operator of the most active areas and their severity. The computer front panel switches allow the operator to select any array and its monitoring area for display on the CRT.

---

*This appendix is a report to ORNL by M. P. Kelly, Field Test Manager, Dunegan/Endevco, whose work was performed under UCCND Purchase Order 11Y-7328V.

BLANK PAGE

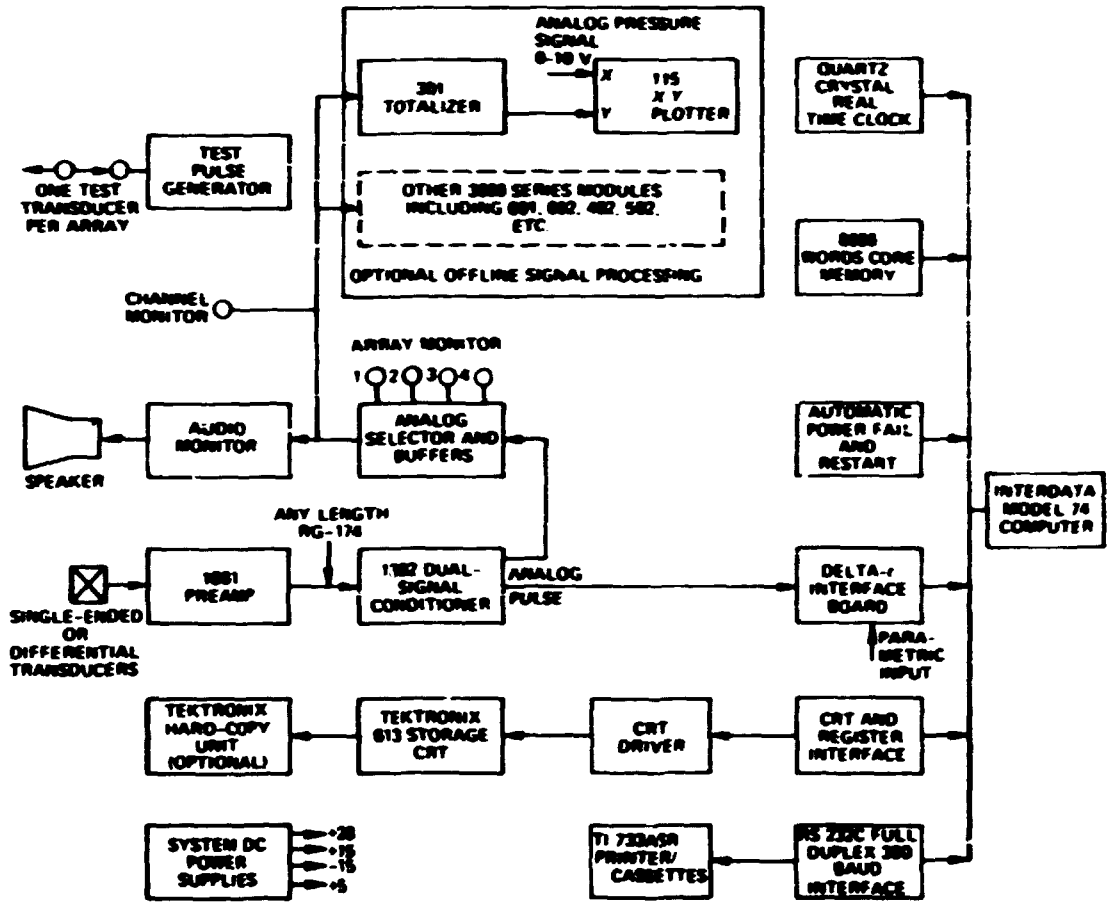

Fig. D-1. 1032 block diagram.

Terminal: Besides serving as an input device for the test operator, the printer/cassette combination provides a hard-copy output of each event for test analysis. The event number, array number, delta-*t*'s, source coordinates, test time, and event severity are output for each event. The cassette record permits the operator to either duplicate the test results at a later date or actually recompute and display "new" source coordinates using an alternate calibration value.

Calibration: The 1032 is self-calibrating since the wave velocity of the material is measured automatically by the system during a special calibration run prior to testing. A piezoelectric transducer used as a pulser is attached to the structure next to one of the pickup sensors and excited by an electrical signal to simulate an AE event. The closest transducer detects the event immediately and enables three delta-*t* counters, which are disabled as the other sensors are hit. This technique provides the system with the maximum time of flight between transducers for rejection of erroneous data in hardware, as well as calculation of source coordinates of legitimate data.

The vessel monitored in this work was a vertical cylinder of A533, class 1, low-carbon steel. Two arrays of four sensors each were attached to the vessel using plastic tape and a room-temperature vulcanizing

compound. The center transducer of each array is the origin for that array, and the X and Y coordinates are given in inches from that point. The arrays were positioned such that the flaw was located 305 mm (12 in.) from the center of each array. Figure D-2 illustrates several views of intermediate vessel V-7 including the approximate position of all Dunegan/Endevco transducers.

The 1032 system specifications during the test were as follows:

Transducers: 140-kHz resonant frequency, single ended
Filter range: 120 to 240 kHz
Preamplifier gain: 40 dB
Secondary amplifier gain: 22 dB
Total system gain: 62 dB
Arrival time resolution: 0.1 μsec

Intermediate vessel V-7 was monitored over a 2-hr period on June 19, 1974, during which a total of 819 AE events triggered at least one sensor. More than 600 of these events were very weak in amplitude and did not trigger all four transducers of any one array during the maximum time allowable (maximum time is equal to the time it takes for an AE event that occurs underneath one outside sensor to travel from that sensor to another outside sensor). A total of 158 events successfully passed all the 1032 validity checks. Table D-1 includes the breakdown by pressure increment of the number of valid events as well as the number of events recorded from the flaw region. The accuracy incorporated in determining flaw activity was approximately half the wall thickness in the Y direction.

The AE activity (counts) as a function of pressure is presented in Fig. D-3. Counts represent a well-defined indication of event magnitude and are proportional to the amplitude of the AE signal

Table D-1. Number of valid events and flaw activity as a function of pressure

Pressure increment (ksi)	Total number of recorded events	Number of events from flaw	Percent of valid events from flaw
0–4	4	0	0
4–5	6	3	50
5–6	7	2	29
6–7	10	7	70
7–8	9	4	44
8–9	3	0	0
9–10	10	4	40
10–11	5	0	0
11–12	9	4	44
12–13	5	1	20
13–14	5	1	20
14–15	6	0	0
15–16	6	0	0
16–17	3	0	0
17–18	5	1	20
18–19	5	0	0
19–20	8	0	0
20–21	23	4	17
21–21.3	29	7	24

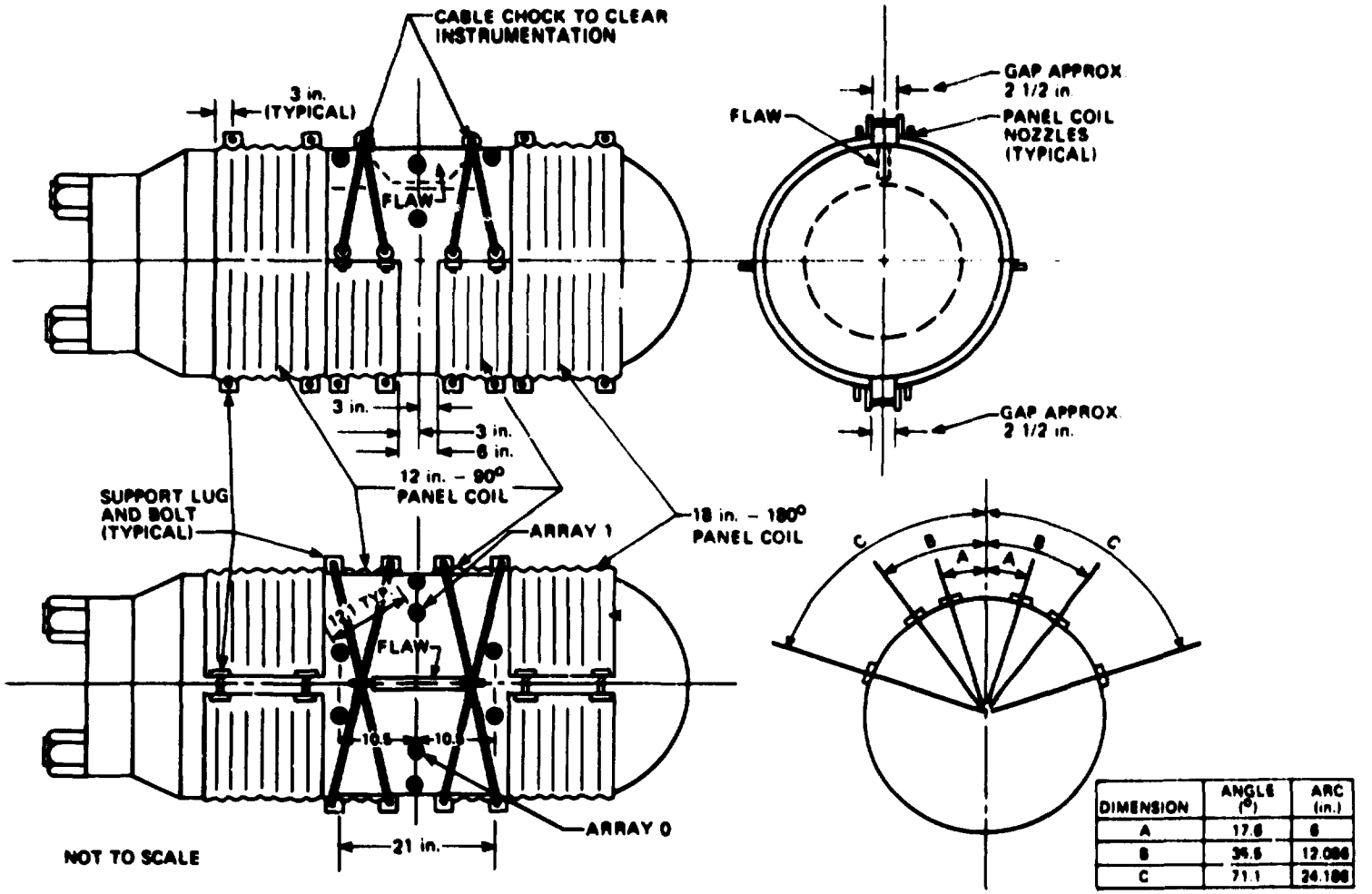

DIMENSION	ANGLE (°)	ARC (in.)
A	17.6	6
B	35.5	12.086
C	71.1	24.186

Fig. D-2. Approximate location of Dunegan/Endevco sensors with respect to flaw.

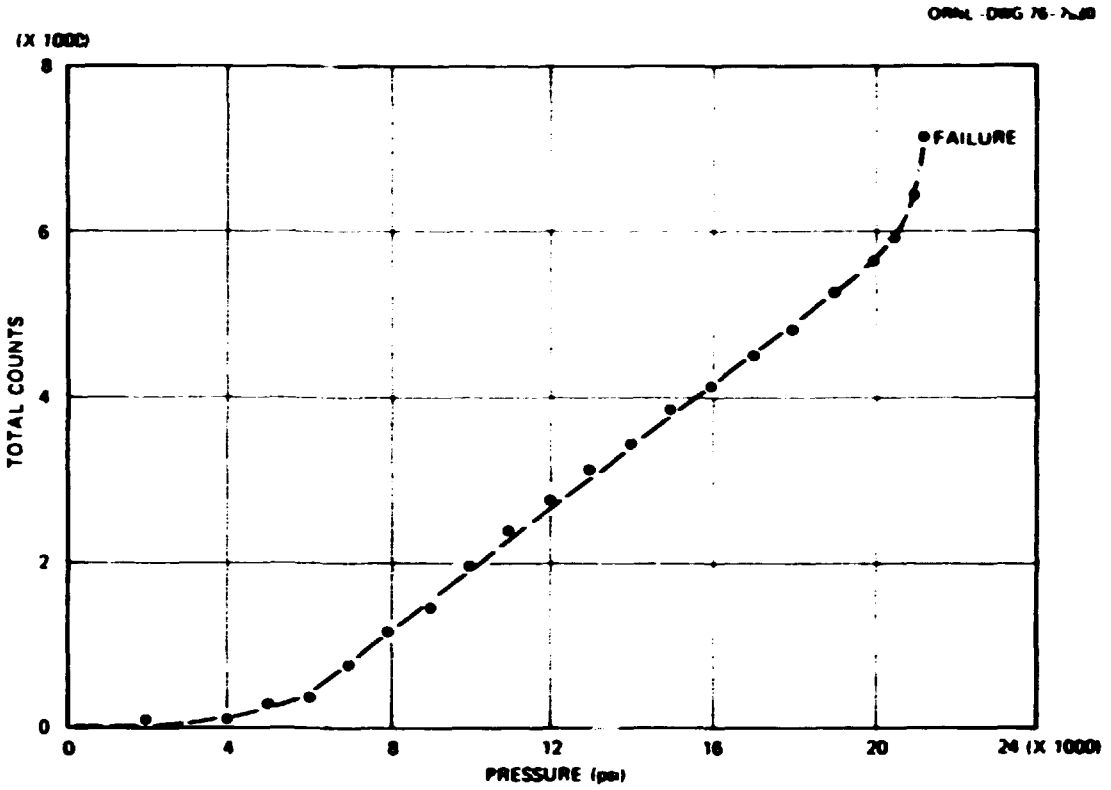

Fig. D-3. Summation of counts as a function of pressure for V-7.

produced by a transducer. Hard-copy reproductions of the source activity for arrays 0 and 1 are shown in Figs. D-4 and D-5. The original flaw coordinates [457 mm (18 in.)] are indicated by solid lines in these figures.

DISCUSSION OF RESULTS

Acoustic emission from the artificial defect was recorded by both of the four-transducer arrays attached to V-7. Although array 1 received more total events, most of the flaw emission triggered array 0. Each of the array CRT plots (Figs. D-4 and D-5) includes several sources to the sides of the arrays. These sources were probably caused by heater coil drag as the vessel expanded. The scatter of sources from the artificial defect can be attributed to wave transmission problems related to physical vessel geometry and transducer layout. Normally, in pressure vessel testing, transducers would be separated by distances at least five times the vessel thickness in order to reduce the effect of bulk wave transmission paths. The V-7 heating coils prevented normal transducer spacings and also accounted for the close proximity of the transducers to the actual flaw. Since bulk waves tend to attenuate much faster than surface waves, their effect is, of course, more profound near a source. Four of the AE transducers were located within 152 mm (6 in.) of the defect due to the presence of the heating coils.

The scatter from a real flaw in a pressure vessel with a normal transducer arrangement would be significantly less severe.

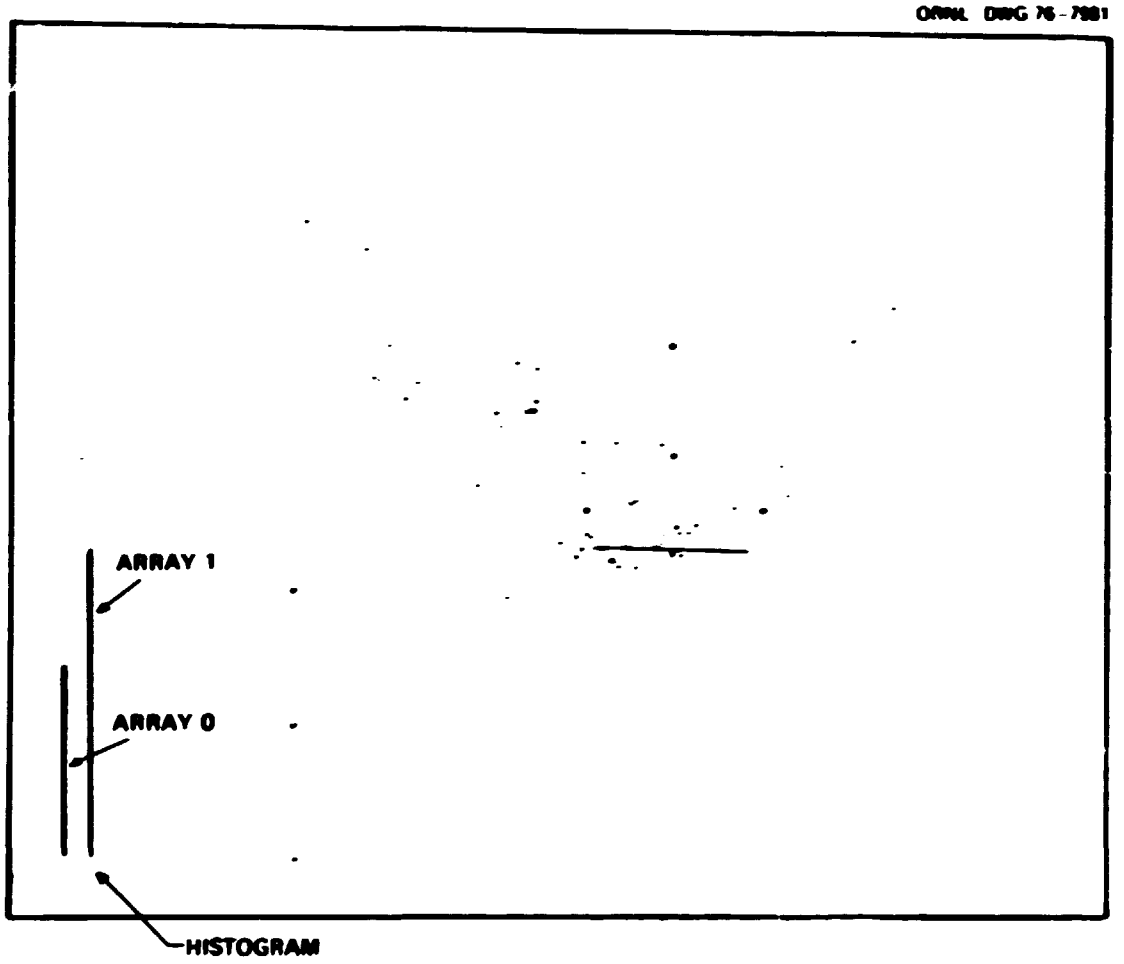

Fig. D-4. Source activity for array 0.

CONCLUSIONS

The following conclusions can be drawn from the test results:

1. The count pressure curve could have been utilized to halt pressurization prior to failure had this been desirable. A substantial change in slope was detected between 138 and 145 MPa (20 and 21 ksi).

2. The bulk of properly located flaw emission was detected prior to 83 MPa (12 ksi), although flaw activity did resume at 145 MPa (20 ksi). The initial data might be attributed to cracking of the EB weld at the root of the sawcut.

3. Some of the scattered emission in each array may be actual flaw emission. Significantly larger arrays would reduce scatter and improve locational accuracy.

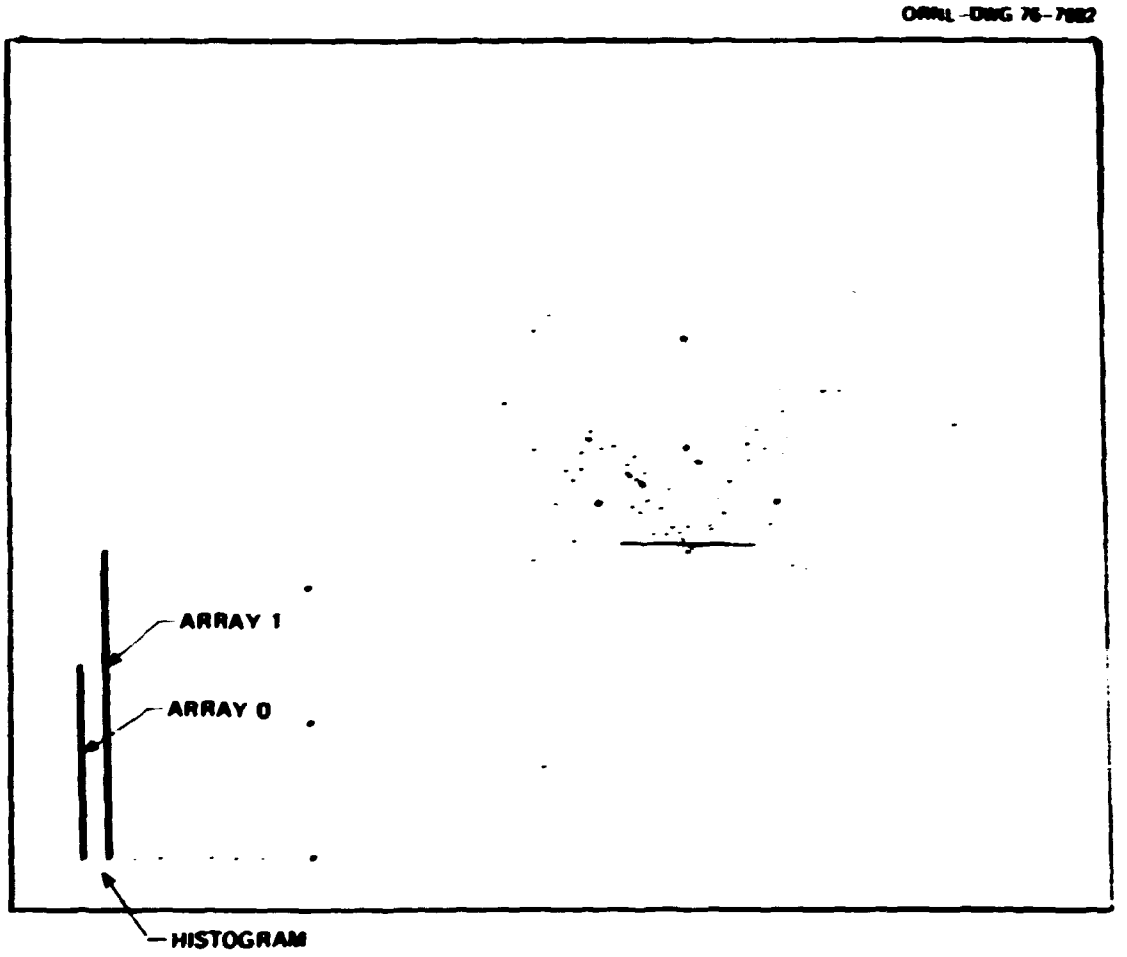

Fig. D-5. Source activity for array 1.

REFERENCES

1. M. P. Kelly and R. L. Bell. *Detection and Location of Flaw Growth in the EBOR Nuclear Reactor Vessel*, Dunegan/Endevco Report DE-73-4.
2. A. T. Green and H. L. Dunegan, "Acoustic Emission Analysis of Crack Propagation and Fracture in Pressure Vessels and Pressure Vessel Materials," presented at the First International Conference on Structural Mechanics in Reactor Technology, Berlin, Germany, September 1971.
3. D. O. Harris and H. L. Dunegan, "Verification of Structural Integrity of Pressure Vessels by Acoustic Emission and Periodic Proof Testing," *Testing for Prediction of Material Performance in Structures and Components*, STP-515, pp. 158–70, American Society for Testing and Materials, 1972.
4. R. Gopal, "Westinghouse Acoustic Emission Studies at EBOR," Final EEI-TVA Rp 79 Meeting, San Antonio, Tex., Dec. 11, 1972.
5. D. L. Parry, *Acoustic Emission Analysis in Oil and Chemical Industry*, Exxon Nuclear Company, Richland, Wash. (April 1972).

6. N. O. Cross, L. L. Loushin, and J. L. Thompson, "Acoustic Emission Testing of Pressure Vessels for Petroleum Refineries and Chemical Plants," *Acoustic Emission*, STP-505, pp. 270-96, American Society for Testing and Materials, 1972.

7. A. A. Pollock and B. Smith, "Stress-wave Emission Monitoring of a Military Bridge," *Non-Destructive Testing*, pp. 348-53 (December 1972).

8. M. P. Kelly, D. O. Harris, and A. A. Pollock, "Detection and Location of Flaw Growth in Metallic and Composite Structures," presented at the ASTM Symposium on Monitoring Structural Integrity by Acoustic Emission, Ft. Lauderdale, Fla., Jan. 17-18, 1974.

9. R. G. Liptai, C. A. Tatro, and T. F. Drouillard, "Nondestructive Evaluation Concepts Applied to Industrial Use of Acoustic Emission," presented at the ASTM Symposium on Monitoring Structural Integrity by Acoustic Emission, Ft. Lauderdale, Fla., Jan. 17-18, 1974.

10. R. R. Coyle, "The Use of Acoustic Emission to Improve Rocket Motor Case Structural Reliability," Paper 73-1258, presented at AIAA SAE 9th Propulsion Conference, Las Vegas, Nev., November 1973.